

2017 NSF/REU

**RESEARCH EXPERIENCE
FOR UNDERGRADUATES
IN PHYSICS**



STUDENT RESEARCH PAPERS

VOLUME 28 PART 2



**REU DIRECTOR
UMESH GARG, PH.D.**

MicroMegas Design

Joseph Levano

2017 NSF/REU Program
Physics Department, University of Notre Dame

Advisor: Professor Tan Ahn

July 28, 2017

MicroMegas Design

For the summer REU program, I worked with Dr. Tan Ahn's Active Target group on two projects, I worked on designing MicroMegas detector pad layouts and on simulating TwinSol runs using LISE++ to evaluate their efficiency. Both of these projects were designed to assist the group's experiments in determining nuclear structure.

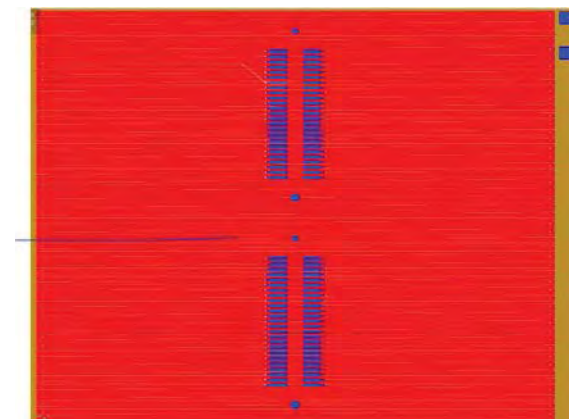
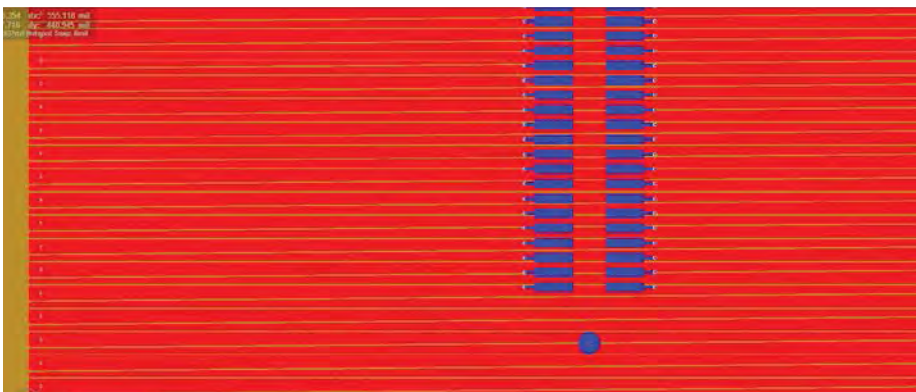
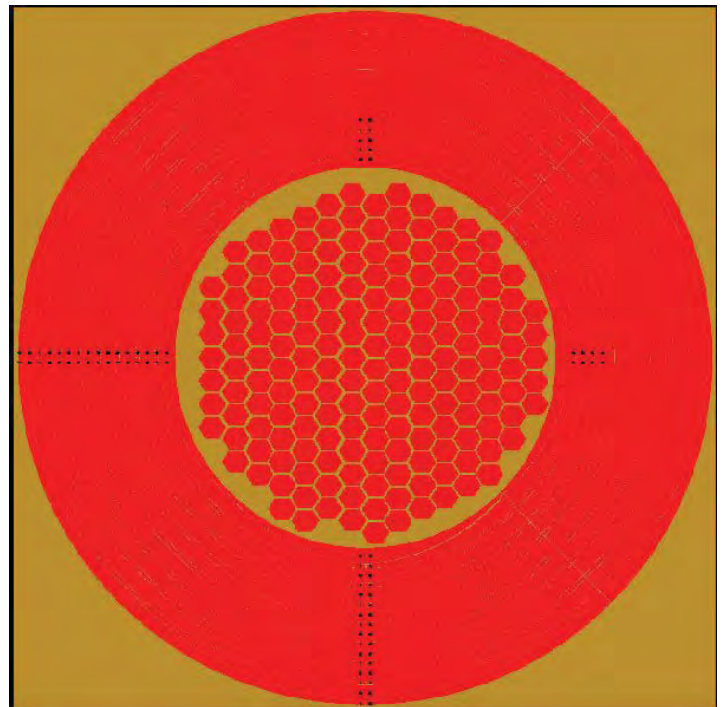
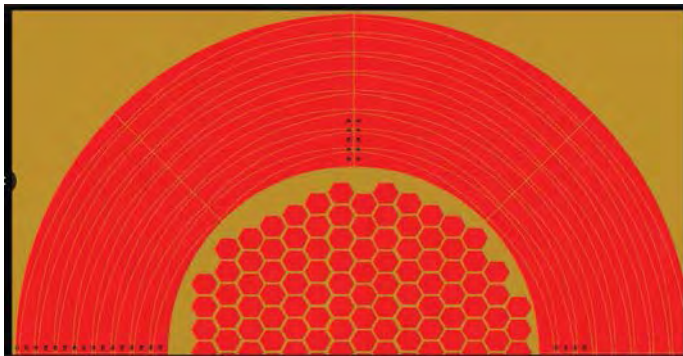
The goal of our group is to carry out experiments to determine the nature of nuclear structures and the stability of these structures. In order to carry out these experiments we will use a Time Projection Chamber. In our experimental setup, the chamber will contain a gaseous target with a uniform electric field applied over the whole chamber by a tower of rings enclosing the tower with a constant voltage drop across each each ring (Electric Field~ 600 V/cm¹). At the bottom of the chamber will be a mesh, below which is a much stronger electric field (Electric Field ~ 43,000 V/cm¹), at the bottom of this field is the MicroMegas detector. In order to create the radioactive ion beam which we will fire into the chamber we start by accelerating a beam of stable ions. By directing this stable beam into a carefully selected "primary target" we can create a second beam of radioactive ions. This beam of radioactive ions will be directed into our time projection chamber where it will encounter the gaseous target. The reaction between the radioactive beam and the gaseous target is the reaction that we are interested in. Within the chamber, the ions will collide with the atoms of the gaseous target. These collisions will knock electrons off of the atoms of the gas, creating free electrons in the chamber which are then accelerated towards the bottom of the chamber by the uniform electric field. These electrons go through the mesh and accelerate to the point where they knock electrons off of the atoms below the mesh each electron knocking off more. This cascade of electrons settles on a pattern of copper electrically charged plates called "pads", on top of the MicroMegas detector. These pads

¹Design and Construction of Large Size Micromegas Chambers for the Upgrade of the ATLAS Muon Spectrometer. Phillip Lössel, Ralph Müller

will send the electrical signal from the electron pulse through a via (a conductive path between the layers of the MicroMegs) to another layer of the Micromegas. This layer will have traces connect to a set of feedthroughs that transmit the signal to the computer. Using this X-Y position of the electron pulses on the plane, we can see the X-Y position in the chamber where the reactions occurred. The Z component of the reactions location can be determined using the time the electrons took to impact the detector. Using the location of the reaction can tell us about what kind of nuclear structures are prevalent in our target and their stability and lifetimes. Nuclear structure data we learn from these experiments will be applied to learn more about the causes for different nuclear structures.

My work on the MicroMegs was focused on designing the patterns of the copper pads on the top layer of the detector. The designs of the pads are very important to our experiments because they determine the amount of data we can gather and the precision of that data. The relevant characteristics of the pad design are size, shape, and location. If we use a smaller pad, we will have more precise location data for each electron pulse however we must keep our pads large enough that the via connecting the pad to the layers inside the board does not occupy a substantial space on the board. The shape of the pad determines how closely we can fit the pads together, hoping to minimize the dead space between each pad so that there is a minimum of wasted data. However another interesting factor involved in shape is the relative area of a given pad to its nearest neighbor. If there is a larger surface area on one pad than an adjacent one we will get a stronger reading for the pulse on the larger pad, this allows us to narrow down more precisely where on the pads the pulse occurred. The last relevant characteristic of the pads is the location. If we can tessellate the pads effectively we can fit many of them into the area of the board we expect to be detecting the majority of the pulses.

The designs I have worked on this summer have been focused on two designs mostly, making a design focused around hexagonal pads, and fine tuning and submitting a design of interlocking triangular pads created by a previous group member for fabrication. Both pad plane designs are pictured below.



Presented are larger images of both designs followed by close up shots in order to better see the pad design. The first design is centered around a central “honeycomb” of hexagonal pads, these are surrounded by concentric rings, actually made up of 8 arcs each. The obvious benefits to this design are its lack of dead space, easy symmetry, and the rings around the outside allow us to get a better look at where exactly an electron avalanche triggered the pad. However the drawbacks to this design are the complexity of the pad plane, leading to high fabrication costs and a necessary large size in order to fit the networks for each pads connection. In addition because each pad network has to be connected separately and each one has to be connected manually, the amount of time to produce this board is significantly longer than our other design. The second design is a square made up of interlocking triangular pads (similar to a backgammon board). This design allows for a large number of pads in a small space, and the triangular pads allow us to find more detailed position data. This is due to the fact that any electrons landing on two adjacent pads are landing on different surface areas, allowing us to further refine our position data. The drawbacks to this design are that each pad is 10 cm long (x axis length). While the triangles help us negate the effects, it can still be difficult to pinpoint where the electron avalanche contacted the pad.

Using LISE++ to simulate spectrometry events in TwinSol allows our group to make informed decisions about which reactions are viable in that we can derive a significant amount of data events from them to carry out an experiment. With the help of Dr. Jim Kolata I have simulated a number of different runs on TwinSol to determine, among other things, our ability to purify a beam generated by TwinSol of undesirable elements without losing too much of our desired beam. One run that I simulated with the help of Dr. Kolata was the reaction of $\text{Li } 8$ with a Beryllium target or with a Deuterium target, both in order to produce a beam of Li-9 . We started with the basic TwinSol setup, then by varying certain parameters we were able to

determine which reaction we preferred. Using the Be target to produce our beam, we were able to minimize the transmission of other impurities. By adding an additional stripper foil to the crossover point between the TwinSol solenoids allowed us to further purify the beam including the additional choice to make on the thickness of the foil. Improving my LISE++ abilities will allow me to manipulate the parameters of an experimental simulation to determine its potential usefulness.

My summer of research has been very productive and very enriching towards my goal of becoming a research scientist. I have done good work on designing the new MicroMegas we will use in our next generation of experiments in the TPC and I have edited and ordered the first MicroMegas we will use in our experiments. My immediate plan for the future is to hopefully join my group in carrying out live runs when the school year begins again. I hope that my research skills will continue to improve and I can keep contributing to the body of scientific knowledge.

References

1. Design and Construction of Large Size Micromegas Chambers for the Upgrade of the ATLAS Muon Spectrometer, [Philipp Lösel](#), [Ralph Müller](#). [arXiv:1508.02541](https://arxiv.org/abs/1508.02541)

Off-line Commissioning and Improvement of the Notre Dame MR-TOF

Biyang Liu

2017 NSF/REU Program
Physics Department, University of Notre Dame

ADVISOR: Maxime Brodeur

1 Introduction

The study of neutron-rich nuclei near neutron number $N=126$ nuclei is of great importance for better understanding the astrophysical rapid neutron capture process. Unfortunately, the production of those rare radioactive nuclei is very challenging. A new and unique facility located at Argonne National Laboratory will aim at producing these exclusive nuclei. Unfortunately, these exotic nuclei also come with a large amount of contaminant species. Hence, a separator is needed to get rid of that contamination and provide clean radioactive ion beams (RIB) to the experiments. Multiple-Reflection Time-of-Flight Mass-Spectrometer (MR-TOF-MS) are suitable as they have a high enough resolving power to separate isobars with a short life time.

We have developed a MR-TOF-MS at the University of Notre Dame to be used at the future $N=126$ beam factory of ANL. This MR-TOF-MS is now under off-line commissioning in order to optimize its resolving power and efficiency.

During the off-line commissioning, we found that a large fraction of the beam was being lost due to a poor injection. However, we found that adding a new steerer that can also act as an Einzel lens may help to adjust the injection optics and solve the problem. Simulations using SIMION was carried out to study the influence of the new steerer and confirm its need.

2 Motivation of building a MR-TOF-MS

The rapid neutron capture process (r-process) refers to a series of reactions responsible for the creation of approximately half of the atomic nuclei heavier than iron. In this process, heavy seed nuclei capture neutrons more rapidly than the time scale of the radioactive beta decay. The r-process pushes the nucleosynthesis far from stability into uncharted regions. The astrophysical location of this process, which includes supernova and neutron star mergers as likely candidates, is the subject of ongoing debate. Since few measurements have been done along the r-process, the study of it is necessary.

According to recent sensitivity studies, some particular nuclei and properties are more influential than others for the r-process. Among these properties, atomic mass have shown to be the most critical impact. Nuclei around the closed neutron shell $N=82$ and $N=126$ have high impact on the final abundances produced by the r-process. Unfortunately nuclei responsible for creating the $N=126$ peak are hard to access. However, multi-nucleon transfer reactions have shown to be a viable means of reaching the $N=126$ region, and Argonne National Laboratory is going to build facility that will make use of these reactions, enabling the study of $N=126$ nuclei. The first experiment at beam factory will be high-precise mass measurement. Such measurement requires particularly pure radioactive beams. To this end, we have built a multi-reflection time-of-flight mass spectrometer(MR-TOF-MS) that will filter out isobaric contaminants.

3 A brief introduction of TOF-MS

Time-of-flight mass spectrometers have been widely used in many fields of mass spectrometry. Its advantages is the large mass range, sensitive operation and the ability to record mass spectra on an extremely short time scale. Apart from these, for a given mass resolution, a very high mass accuracy can be obtained. The resolving power of certain TOF-MS can be high enough to resolve most short-lived isobaric nuclei, even if they differ significantly in abundance. Apart from being a spectrometer, another motivation for the development of TOF-MS is its application as an isobar separator. [1]

Multiple-Reflection TOF-MS, which have the ion bounce back-and-forth along the length of the device is an elegant method to shorten the length of the device and allows to extend the time of flight almost arbitrarily. However, one potential problem happening after many turns in the analyzer is the spread of the different ion species bunches due to the energy spread. This could limit the range of the number of turns and the resolving power that can be achieved. However, this effect can be minimized with proper tuning of the mirror potentials. Such optimization was the goal of the work

presented here.

4 The off-line set-up

The key points to consider in the operation of a MR-TOF-MS are the proper capture, reflection and extraction of the ion bunches. The principle consists of using two sets of electrostatic ion mirrors to reflect the ion bunches back and forth in the device, realizing a folded flight path. To separate ions of different mass, many round trips are needed. The capture and extraction can be accomplished either by switching the potential of the mirror electrodes, or the potential of the drift tube. Since the stability of the mirror electrodes the voltage is very important for the performance of a MR-TOF-MS, we chose to switch the drift tube. [2, 3]

Finally, the mass of interest, separated and extracted from the MR-TOF is selected using a Bradbury-Nielsen gate (BNG). A BNG comprises two sets of parallel wires which have the same voltage on but different polarity. When the gate is activated, ions would be scattered, while the beam is allowed to pass when it is grounded. As is shown in Fig 1.

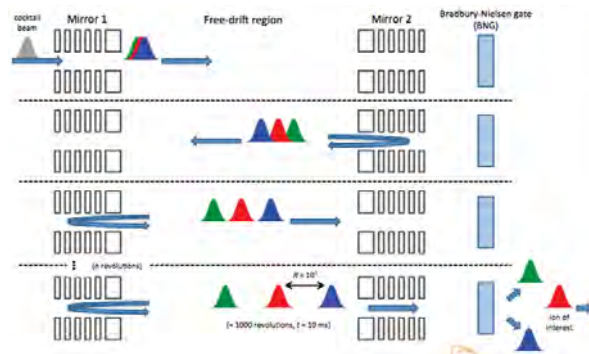


Figure 1: The principle of MR-TOF and the BNG

The set-up for the off-line commissioning (see Fig.2) consists of an ion source to produce the ion pulse, an Anode to pull the ions from the ion source, and a BNG to create ion pulses out of the continue beam. The MR-TOF includes five pairs of electrostatic ion mirrors, a pair of electrostatic lens and a drift tube. It reflects the ions back and forth to get it travel long enough to be separated.

The set-up also includes 2 Einzel lenses, one before and one after the MR-TOF, to help focus the beam like optical lenses. There is also a set of steerers to adjust the direction of the beam before it enters the MR-TOF. The first piece of diagnosis are Faraday cups used to tune large continuous beam current of several PA. The second piece of diagnosis are MCPs(Micro-channel plate) that allow to perform single-ion counting on the ion bunches. The MCPs after the MR-TOF was the main detector used for the measurements we performed.

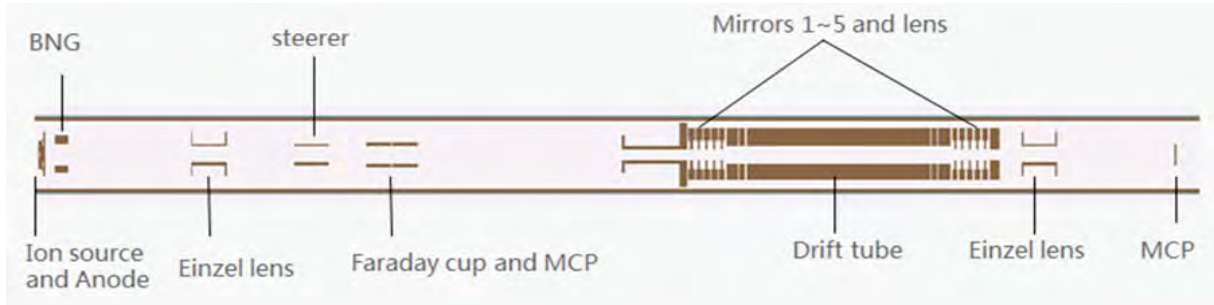


Figure 2: The current set-up for off-line MR-TOF-MS

5 MR-TOF-MS optimization procedure

The good performance of a MR-TOF depends on a high resolving power, which is defined as the following:

$$R = \frac{t}{2\Delta t} \quad (1)$$

$$t = t_1 + t_0 + t_2 \quad (2)$$

where t_1 is the time of flight from the ion source to the middle of the drift tube in the MR-TOF, t_0 is the time of flight in the MT-TOF, t_2 is the time of flight from the MR-TOF to the detector, Δt is half width of the peak and t is the total time of flight.

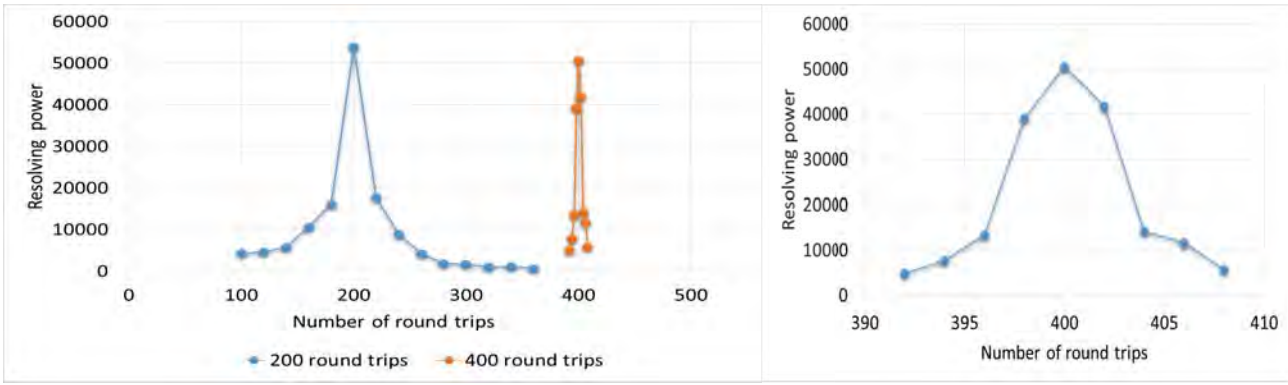


Figure 3: Change in resolving power for 200 and 400 round trips
 Figure 4: Change in resolving power for 400 round trips (zoom of Fig.4)

To get a good resolution power, t should be as large as possible and Δt should be as small as possible, which means that we need to minimize the spread of ions as much as possible. It is easy to imagine that when we are trying to separate distribution of two different species of ions, there would be a large overlap, that would make it difficult to separate them apart. On the other hand, if the peaks are narrow enough, we might be able to separate them.

By adjusting of the voltage on the mirrors and lens we can get higher resolving power and better efficiency. Hence, we varied the potential on mirror 1, mirror 2, mirror 3, mirror 4, mirror 5, the lens and the drift tube in the MR-TOF, we optimize by recording several quantities: the largest number of ions of the peak, N_{max} , the full width half maximum of the peak, Δt , and the total number of ions in the peak, N . We vary the voltages to find the one with the largest N_{max} or the smallest Δt and record it as the optimal setting.

First, we optimized the MR-TOF for 200 round trips. Then with that setting, we varied the number of round trips from 100 to 360 and saw a rapid drop in resolving power as one depart from 200 round trips. The same was observed when we tuned to 400 round trips. (See Fig.4 and Fig.5) Only the effect was more dramatic. These could correspond to different time focus points.

Then we optimized the drift tube voltage for 200, 250, 300, 350, 400, 450, 500 round trips in order to get the correct time focus for these number of round trips.

These optimization resulted in a nearly round trip independent resolving power of between 50000 and 60,000, as is shown in Fig.6.

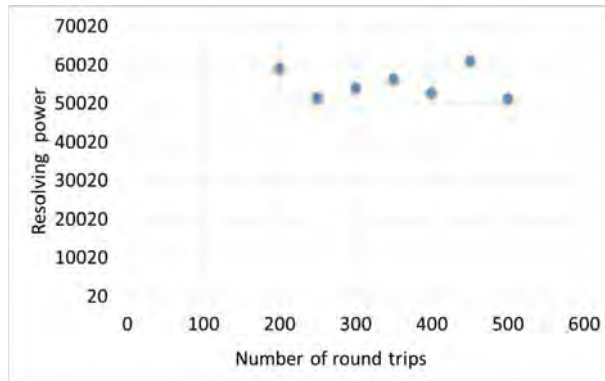


Figure 5: Resolving power against number of round trips

Efficiency is another important aspect. We defined it as the number of ions flying through the MR-TOF if we are not in capture mode. Fig.3 shows efficiency vs the time of flight in MR-TOF. As it's shown, the efficiency decreases rapidly with increasing of time of flight, which means we are losing beams in the process of reflection.

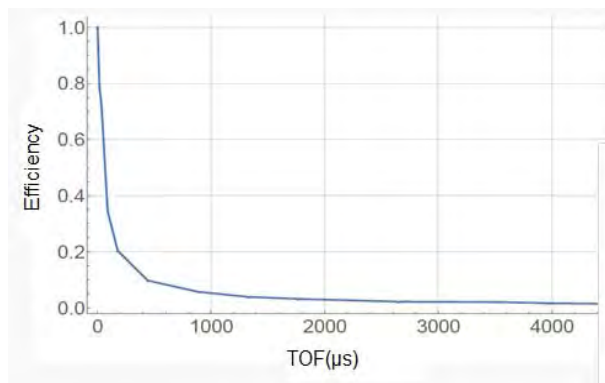


Figure 6: Change in efficiency against time-of-flight

Due to the rapid drop in efficiency with number of round trips, we decided to investigate if we could improve the injection of the beam in the MR-TOF.

6 Simulation on a 3D model of the off-line test set-up

6.1 Adding a new steeter

The measurements in the previous section indicate potentially that a lot of ions were being lost before they even enter the MR-TOF. We investigated that by checking the number of ions hitting the Einzel lens (see Fig.2) at the entrance and the number of ions hitting the first Faraday cup (see Fig.2), checking the efficiency of transportation from the Einzel lens to the position of Faraday cup. The current hitting the Einzel lens and the current hitting the first Faraday cup are recorded. As is shown in Fig.7 , the ratio of current from the first Faraday cup to the current hitting the Einzel lens is quite low, which means lots of ions are lost before the MR-TOF.

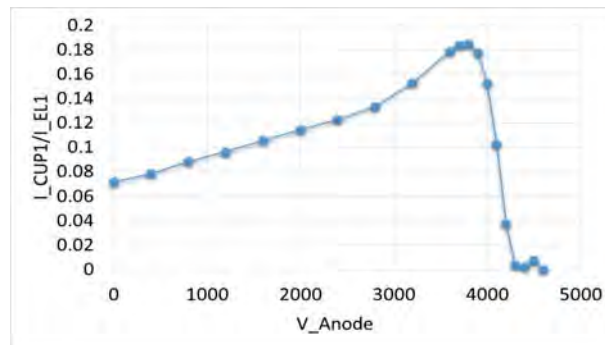


Figure 7: The current ratio of current from the first Faraday cup to the current from the Einzel lens at the entrance

Hence, to see how things can be improved, we created a cylindrical symmetry model of the system to simulate the trajectory. We found the ratio of the ions hitting the Einzel lens in this simulation to be much higher than reality. After tilting the direction of the injection of ions, the ratio become much more close to the reality. (see Fig.8) This implies that the lost of the beams may due to the beam coming at an angle. Hence, we decide to add a new steerer after the BNG and before the first Einzel lens to steer the beam in the right direction.

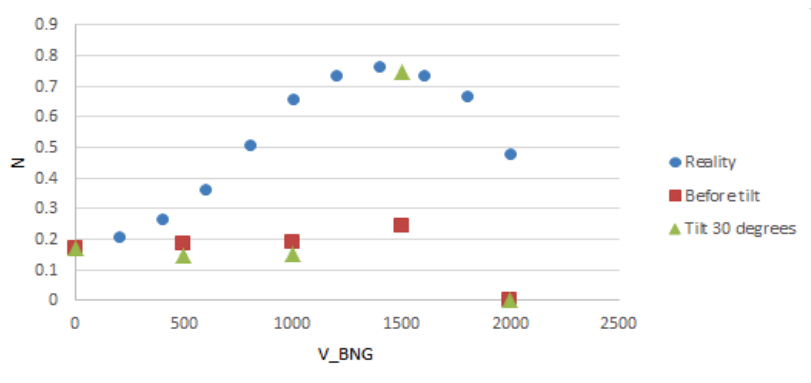


Figure 8: The ration in reality, before tilting in simulation and tilt 30 degrees in simulation

6.2 The building of a 3D model and simulations

To simulate the deflection of the beam by the BNG to create an ion bunch, a 3D model was built using SIMION. Due to the limitation of disk space, the model had to be divided into two parts: the first part was from the ion source to the BNG, using a planar symmetry and the second part include the whole equipment, from the ion source to the last MCP detector, using a cylindrical symmetry. When running the simulation, we begin to fly ions from the ion source in the first part, and record all the information of the ions after the BNG. Then we flew these ions in the second part, starting at the position where the information was recorded in the first part.

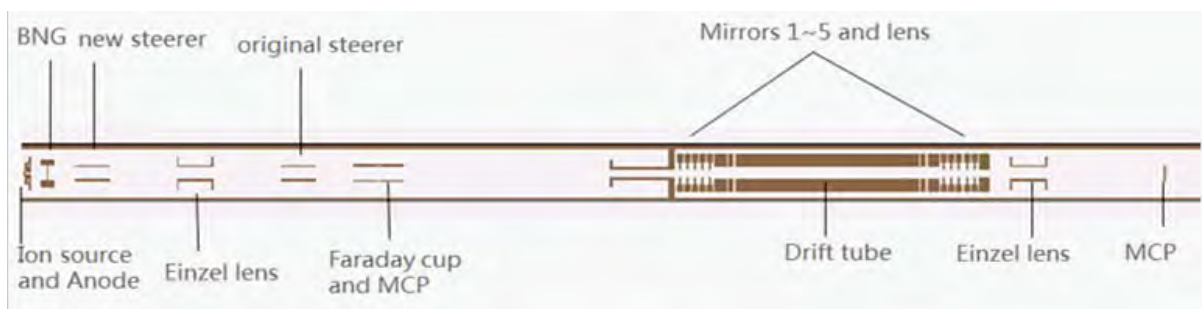


Figure 9: The set-up for off-line MR-TOF-MS with a new steerer

As is shown in Fig.9. We also added a new steerer after the BNG. Fig.10 shows the BNG used in the simulation.

For the simulation, we first varied the voltage of the new steerer (making it act like an Einzel lens) and the BNG. The optimal voltage for the new steerer to achieve optimal transmission through



Figure 10: The design of BNG in 3D model

the first Einzel lens was found to be 3000V. This optimal voltage was found by recording the position of the farthest ion radially at the entrance of MR-TOF to determine when the radius of the beam gets minimized.

Secondly, we varied the potential on the new steerer and the first Einzel lens sequentially in two dimensional scan while recording the number of ions arriving at the very end. The optimal voltage of 2300V for the new steerer and 1350V for the Einzel lens were found. After this, we varied the voltage for the original steerer and determined the optimal voltage of 750V. Then, to optimize the transport across the MR-TOF, we varied the potential of the first mirror from the entrance and the MR-TOF lens electrode finding 3500V and -5000V respectively as optimal potentials. Finally, we varied the anode and new steerer again and found the optimal voltage for the new steerer of 2100V and of 4400 for the anode.

After the optimization, the efficiency from the ion source to the last MCP above 70% was obtained. Before adding the new steerer, the current ratio of current from the first Faraday cup to the current from the Einzel lens at the entrance is less than 20%. The efficiency improved quite a lot.

7 Summary and outlook

A multi-reflection time-of-flight mass spectrometer has been built and is currently under commissioning at Notre Dame. This report present the first phase of off-line commissioning. The process of optimizing the voltages of different parts of the MR-TOF-MS was described. Resolving power

reaching 60,000 have been seen. However, poor efficiency of 2% after 200 round trips are also observed. This led to a series of simulations that showed the need for one more steerer to improve the situation. Next the new steerer would be added to the MR-TOF-MS to get better resolving power and efficiency performance of the MR-TOF-MS. Then the commissioning will continue until adequate resolving power and efficiency are obtained.

References

- [1] Wolfgang R. Pla, Timo Dickel, and Christoph Scheidenberger. Multiple-reflection time-of-flight mass spectrometry. *International Journal of Mass Spectrometry*, 349:134 – 144, 2013. 100 years of Mass Spectrometry.
- [2] R.N. Wolf, D. Beck, K. Blaum, Ch. Bhm, Ch. Borgmann, M. Breitenfeldt, F. Herfurth, A. Herlert, M. Kowalska, S. Kreim, D. Lunney, S. Naimi, D. Neidherr, M. Rosenbusch, L. Schweikhard, J. Stanja, F. Wienholtz, and K. Zuber. On-line separation of short-lived nuclei by a multi-reflection time-of-flight device. *Nuclear Instruments and Methods in Physics Research Section A: Accelerators, Spectrometers, Detectors and Associated Equipment*, 686:82 – 90, 2012.
- [3] Robert N. Wolf, Gerrit Marx, Marco Rosenbusch, and Lutz Schweikhard. Static-mirror ion capture and time focusing for electrostatic ion-beam traps and multi-reflection time-of-flight mass analyzers by use of an in-trap potential lift. *International Journal of Mass Spectrometry*, 313:8 – 14, 2012.

The Evolution of Cooperation in Flowing Media

Andrew McEllistrim

2017 REU Program

Physics Department, University of Notre Dame

Advisor: Professor Dervis Can Vural

Abstract

The aim of this project was to develop an effective model to describe the density of bacteria groups in a flowing environment where they undergo diffusion, convection, reproduction, mutation, and are subject to shear due to a flow. This model was designed to determine the regions of high and low density of the bacteria groups under different conditions of shear. The model was constructed based on Fisher's equation [1] (or the Kolmogorov–Petrovsky–Piskunov equation). Fisher's equation falls into the class of P.D.E.'s known as reaction diffusion equations and it is commonly used in Bio-Physics as well as Plasma Physics. The Kardar–Parisi–Zhang (KPZ) equation [2] was also used in the development of this model. The KPZ equation is a non-linear stochastic partial differential equation, that describes the temporal change of height at a given place and time.

The purpose of this project was to develop a system that would coarse grain the bacteria groups in a region and to obtain an effective equation governing the distribution of these groups of bacteria. The importance of this equation lies in being able to know the arrangement of bacteria in a flowing media at the steady state. This is valuable knowledge as it allows us to know under what conditions cooperation between the groups will succeed and under which conditions will the groups either be overrun by mutants or have too low a fitness to survive.

1 Introduction

The question of cellular cooperation is a growing field in Bio-Physics but it has many unventured areas. One of these areas is to search for an effective model to determine the density of groups of bacteria in flowing media. The objective of this project was to find a simple model which could determine the density of the bacteria groups in simple cases while still considering environmental factors such as diffusion, convection and shear due to different types of flow. The type of flow that will be looked at in this paper is Couette flow which gives constant shear. Couette flow is the flow of a fluid in the space between two surfaces, one of which is moving at a tangent relative to the other. The configuration often

takes the form of two parallel plates which is the case being discussed in this paper. The flow is driven by a viscous drag force acting on the fluid, but may additionally be motivated by an applied pressure gradient in the flow direction.

The model also accounts for the individual biological processes of the cells such as reproduction and mutation. Within each group of bacteria, each singular bacteria cell has a certain probability of reproducing per unit time. With each reproduction, the group grows until it has grown large enough to split off into two groups. Within each group of cells, the model assumes that: 1) The individual bacteria are point particles governed by the Navier-Stokes Equation. 2) The bacteria secrete two compounds a public good and a waste product. 3) These secretions obey a set of diffusion equations. 4) The secretion of the public good has a cost to the fitness of the cell secreting it. 5) The absorption of the public good has a net increase to the fitness of all the cells in the group consuming it. 6) The secretion of the waste product has no cost to the fitness of the cell. 7) If a cell or group resides just in the waste it is damaging to the fitness of the cells. 8) Each cell has a certain probability of reproducing per unit time. 9) A mutant cell does not emit the public good and seeks only to acquire the gain in fitness from absorbing it, without having to pay the cost in fitness to produce it. 10) If too many cells mutate, there will not be enough public good secretion to sustain the group and it will die.

Shear influences the groups as it causes groups to elongate and separate faster thus segregating mutant cells and increasing the likelihood of survival (see Figure 2 below). There is a certain value of shear to which cooperation becomes increasingly favourable as it leads to survival. The model developed in this paper looks to deal with the effect of shear in cases where mutation is and isn't possible in the groups.

This paper discusses the effect of shear on the carrying capacity of the groups of cells. The carrying capacity of the groups is the maximum number of groups that can reside in a certain area and still reach an evolutionary stable state where survival is guaranteed. If this number is exceeded the groups will be living in each other's waste and will eventually have too low of a fitness to survive. In this paper, the carrying capacity at different values of shear will be compared between what is expected from the model that was developed and discrete simulations at the steady state of the groups. The steady state is the point in the cells lifetime when their density no longer changes but only with position.

2 Method

This model was developed by combining the terms from Fisher's equation and the KPZ equation to account for the environmental and intracellular factors that affect the bacteria groups. As previously mentioned Fisher's equation falls into the class of P.D.E.'s known as reaction diffusion equations and it is displayed below:

$$\frac{\partial u}{\partial t} = D\nabla^2 u + ru(1 - u) \quad (1)$$

The time dependent differential term and the diffusion term were included to account for the change in density of the groups as they reach the steady state and the diffusion of the secreted chemicals. The final term in Fisher's equation accounts for the reproduction of the groups but it was altered to account for the shear dependence of the reproduction as well as the mutation of the groups.

The KPZ equation is as follows:

$$\frac{\partial h}{\partial t} = v\nabla^2 h + \frac{\lambda}{2}(\nabla h)^2 + \eta(x, t) \quad (2)$$

From this the time differential and the diffusion terms were ignored as they were already included from Fisher's equation. The second term of the KPZ equation was taken and altered by changing it into the standard form of a convection equation, instead of the squared form seen in equation (2). The final term in equation (2) is a noise term that while currently isn't included in the model but may be brought in to account for stochastic fluctuations later.

The resulting equation for the density of the groups from the combination of the two can be seen below:

$$\frac{\partial \rho}{\partial t} = D\nabla^2 \rho + r\rho \left(1 - \frac{\rho}{K}\right) - m\rho + v\nabla \rho \quad (3)$$

Equation (3) is the effective model used to predict the density of the groups as well determine the carrying capacity. The first term in equation (3) accounts from the diffusion of the groups in the environment. The Diffusion Constant D is dependent on the size of the groups as well as the reproduction rate of the groups and was derived using unitary analysis.

The expression for the reproduction rate of the groups was acquired from the paper “Shearing in flow environment promotes evolution of social behaviour in microbial populations” by Gurdip Uppal [4]. The two expressions can be seen below:

$$D = \frac{R^2}{r} \quad (4), \quad r = c\sigma + \omega_o \quad (5)$$

Where R is the size of the groups, c and ω_o are constants acquired from figure 1A.

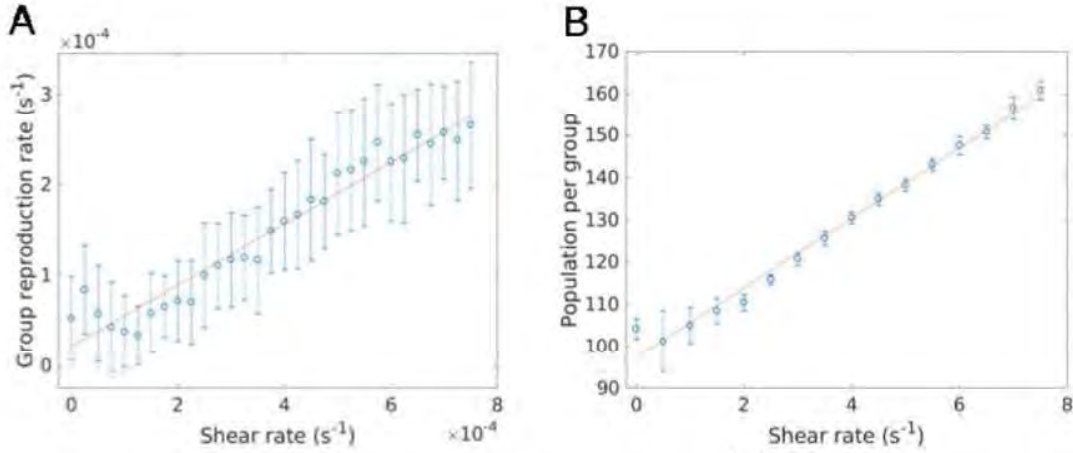


Figure 1.

- A) Group reproduction rate versus shear rate.
- B) Group population versus shear rate used below.

The symbol σ is the shear due to a Couette flow is given in the form $\sigma = \frac{V}{\Gamma}$ (6), where V is the velocity of the velocity due to the flow of the fluid the bacteria is suspended in and Γ is the size of the region the bacteria are in.

The second and third terms in the model account for the change in the number of groups due to reproduction and mutation. The K in the second term of the expression is the carrying capacity of the groups and the derivation of it at the steady state will be shown below. The m in the third term of equation (3) is the mutation rate of the individual cells within the groups. The mutation rate is given by the following expression:

$$m = \frac{1}{T_{mut}} + \frac{1}{T_{T.O.}} \quad (7)$$

$$\text{where } T_{mut} = \frac{1}{\mu N} \quad (8) \quad \text{and} \quad T_{T.O.} = \frac{A}{8d_b} \quad (9)$$

In equation (7) and (8) T_{mut} is time it takes for a cell to mutate and in equation (8) μ is the mutation probability and N is the average population of the group for a given shear rate acquired from Figure 1 B above. The $T_{T.O.}$ term is time it takes a mutant to take over a group i.e. the time for it to reproduce enough that there is not enough public good secretion to sustain the group. In this term A is the area of the group and d_b is the microbial diffusion constant. The fourth and final term in the expression is the convection term which was taken from the KPZ equation and adapted to suit the model.

The result achieved in this paper was comparing the accuracy of the carrying capacity given from equation (3) with the values given from simulations. The expression for the carrying capacity was derived from solving equation (3) at the stable state. At the stable state for a Couette flow the change in density with time is zero. The change in density with respect to position is negligible as a Couette flow is uniform flow thus the groups become roughly evenly distributed. Taking this into account equation (3) reduces to:

$$r\rho^* \left(1 - \frac{\rho^*}{K}\right) - m\rho^* = 0 \quad (10)$$

Where ρ^* is the density of the groups at the stable state. Equation (10) can be rearranged to give the following expression for the carrying capacity:

$$K = \frac{\rho^*}{\left(1 - \frac{m}{r}\right)} \quad (11)$$

To fully utilise equation (11), we need to know the value of ρ^* . To calculate this value an analysis of the change in length of the bacteria groups with respect to shear was used. It was known that the number of groups in the environment with shear was equal to the number of groups in an environment where shear was not a factor by a constant that is related to the magnitude of the shear. This constant was formulated by looking at the change of length of the groups with shear and without it to give:

$$\rho^* = \frac{2R\rho_o^*}{(V + 2\sigma R)\tau} \quad (12)$$

In this expression ρ_o^* is the value of the density of the groups at the steady state without shear. It is equal to the packing constant of the groups over the size of the group. It can be seen fully written out below.

$$\rho_o^* = \frac{\eta}{\pi R^2} \quad (13)$$

The other undefined terms in this expression are τ which is the reproduction time of the cells, it is proportional to one over the reproduction rate, $\left(\tau = \frac{1}{r}, (14)\right)$ and V which is the flow velocity. By using this the following expression for the carrying capacity of the bacterial group was acquired:

$$K = \frac{2\eta r^2}{\pi R(V + 2\sigma R)(r - m)} \quad (15)$$

This equation was then used to compare the accuracy of the model against simulations of bacteria experiencing shear due to a Couette flow at various velocities.

3 Results and Discussion

To test the accuracy of the above expressions simulations of bacteria undergoing shear due to a Couette flow with velocity ranging from 20-160 cm s^{-1} were run. These simulations were allowed to run until the steady state was reached. Below is an example of steady states reached at the maximum and minimum values of shear with and without mutations.

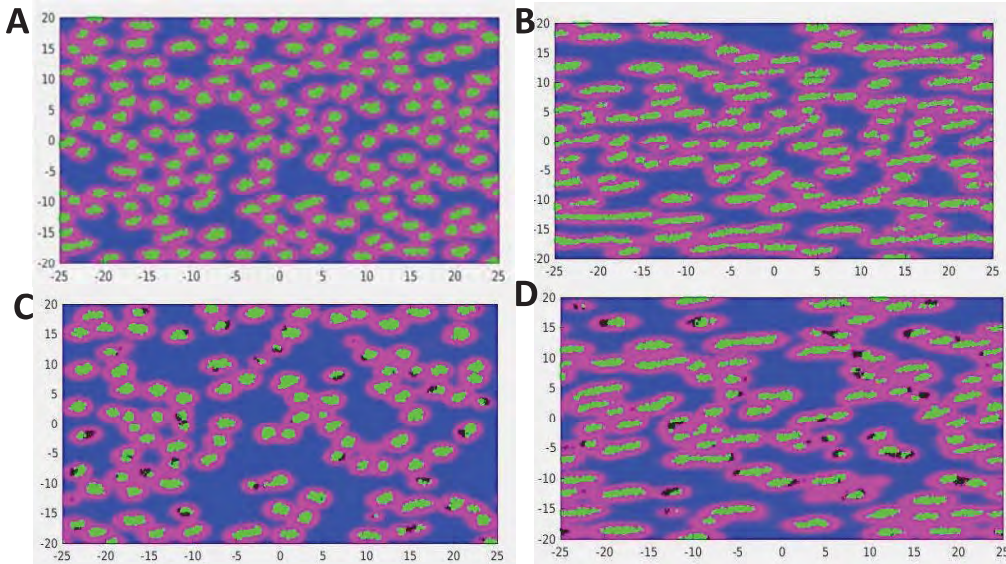


Figure 2. The green regions indicate groups of cells, black dots within the groups indicate the mutant cells in the group, the pink border around the group indicates the secretion of the public good and the blue regions indicate the secretion of the waste.

- A) Simulation image of steady state at 20 cm s^{-1} with no probability of cell mutation
- B) Simulation image of steady state at 160 cm s^{-1} with no probability of cell mutation
- C) Simulation image of steady state at 20 cm s^{-1} with cell mutations
- D) Simulation image of steady state at 160 cm s^{-1} with cell mutations

It is clear to see from Figure 2 A and B that when no mutant cells are present a reasonably accurate steady state is reached as there is an even distribution of cells as well as very few areas being filled just by the waste product. The few gaps that can be seen between the cells are due to the random aspect of the simulations. At the beginning of each simulation a set number of cell groups are randomly distributed throughout the area, an offset of this is that there are regions that never had cells to begin with. To counteract this effect multiple simulations were run and the results are averaged. It is also obvious from Figure 2 C and D that when mutations are possible a less accurate steady state is reached. There are clearly many more regions being occupied by the waste product. This is due to the mutant cells taking over groups and them eventually dying off. As of this a less accurate value of the carrying capacity is reached.

To obtain the value of the carrying capacity at the stable state a programme was used to count the number of cell groups in the region at the end of the simulation. To accurately calibrate this program the number of groups in the region was counted by hand for a set of 8 simulations and then the coarse graining parameters of the programme were adjusted to give similar results as the manual count. This value was then taken and divided by the area that the cells were in to get the average number of cells per unit area. This value was then assumed to be the carrying capacity as the simulations were set up so that the initial number of groups was far in excess of what could grow and survive in the region. Thus, as the simulation progressed to the steady state many of the groups died off leaving the maximum number of groups possible in the region, i.e. the carrying capacity.

These values of the carrying capacity were taken and plotted against the expected values of the carrying capacity determined from the model described above with the appropriate fitting parameters applied. A third line is also drawn in the plots below, this line is an average trend of the results of the simulations. It is used to more clearly show the agreement between the model and the simulations by averaging their fluctuations. The two plots below in Figure 3 show the accuracy of the of the model when mutants are and aren't aloud.

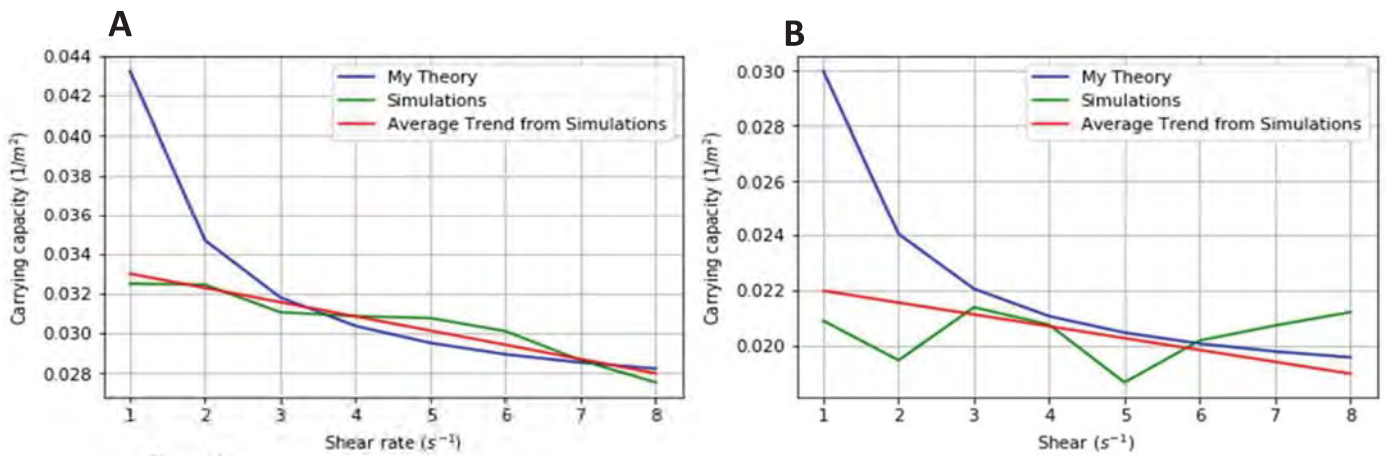


Figure 3

- A) Graph showing the accuracy of the model against the simulations without mutations
- B) Graph showing the accuracy of the model against the simulations with mutations

It is clear to see from the figures above the model does not accurately represent the carrying capacity at low shear but as shear is increased the lines begin to converge giving much more accurate results. The reason the for the disagreement in the low shear reason is partly that the model expects the groups to stretch more than they appear to in the simulations at the low shear values. It is also thought that the introduction of a continuous simulation would increase this accuracy. It would also reduce the fluctuations in the plot for the simulations as the groups would be distributed more evenly. The model also clearly overestimates the value of the carrying capacity when mutants are present as it cannot fully account for the regions where no groups are present as it predicts that they would redistribute to fill in the empty space. This would also be improved by the introduction of a continuous model.

Overall it is clear that the model does appear to converge to what is expected by simulations in the higher shear region. This gives positive indications that with some adjustments when the full model is solved it could give an accurate description of the density of the bacteria groups in cases with simple shear at the steady state.

Acknowledgments

I would like to give special thanks to Professor Dervis Can Vural and Gary Uppal for their help and guidance in doing this project.

References

- [1] R. A. Fisher. "The wave of advance of advantageous genes," *Ann. Eugenics* 7:353–369, 1937.
- [2] Kardar, Mehran; Parisi, Giorgio; Zhang, Yi-Cheng (3 March 1986). "Dynamic Scaling of Growing Interfaces". *Physical Review Letters*. 56 (9): 889–892.
- [3] G.P. Galdi. "An Introduction to the Mathematical Theory of the Navier-Stokes Equations"
- [4] G. Uppal. "Shearing in flow environment promotes evolution of social behaviour in microbial populations"

Using X-Ray Fluorescence (XRF) to Detect Lead in Urban Environments

Patrick Michael McGuire III

2017 NSF/REU Program

Physics Department, University of Notre Dame

Advisor: Dr. Graham Peaslee

Abstract

The Flint lead crisis in 2014 gained national attention when it was found that approximately five percent of children had elevated blood lead levels (more than 5 micrograms per deciliter of blood) after drinking contaminated water. By comparison, in one census tract in St. Joseph County, Indiana it was found that 178 out of 568 (31%) of young children had similarly high levels in 2015. It was suspected that most of this lead came from lead paint or lead in the soils. More than 80% of South Bend homes were built before 1978, when leaded paint was phased out of interior house paint in the United States. Leaded gasoline exhaust in urban areas has made its way into the city soils, and has shown to be a problem in some urban areas. Leaded gasoline was phased out of the US between 1976 and 1996. Since there is currently a national shortage of funding to study the environmental sources of lead exposure, Notre Dame has assembled a lead study group to investigate local homes and vacant lots for sources of lead to help address this public health issue. The team collected dozens of samples of soil, paint chips, and house dust from six houses and four vacant lots this summer. Testing methods such as Inductively Coupled Plasma Optical Emission Spectroscopy (ICP-OES) are very accurate for lead, but they are very time-consuming and destructive, taking several hours to complete only a few samples. X-Ray Fluorescence (XRF) is a spectroscopic method that can measure a sample for lead in under a minute. Our part of the project was to compare dust, paint, and soil samples measured by both the ICP and XRF to assess the accuracy of the spectroscopic method. The discrepancies were found to be minimal with our methods and it is a reliable way to identify areas of concern in homes with children at risk of lead poisoning. A method to provide expanding lead testing services to a broader community can be proposed based on this initial survey and some observed sources of lead exposure in South Bend will be reported.

1 Introduction

1.1 History

The first modern plumbing system was developed by the Romans over 2000 years ago. The word itself originates from the Latin for lead (*plumbum*) and its piping contained significant amounts of lead, a fact that many historians believe contributed to the fall of the Roman Empire. Lead has a long history of causing health problems, including outbreaks of gout and colic, but the first officially reported case of childhood lead poisoning was in 1892 in Brisbane, Australia. That country went on to ban lead in house paint by 1914, but the United States did not do the same until 1978, and did not ban leaded gasoline until 1980. Although these laws went into effect almost 40 years ago, the effects of this element persist in many American cities.

A 2016 Reuters article brought to light the fact that over 3000 towns and cities have recorded lead poisoning

rates in children that were at least double those in Flint in the past few years, South Bend included. Census tract 6 in particular was reported to show that 31.34% of 568 children under the age of seven tested since 2005 had elevated blood lead levels (EBBLs) (See fig 1) [1]. This census tract is only two miles from the Notre Dame, so when this was discovered, a lead affinity group, consisting of faculty and students from the university as well as members of the community, was formed to help families find the sources of exposure to lead.

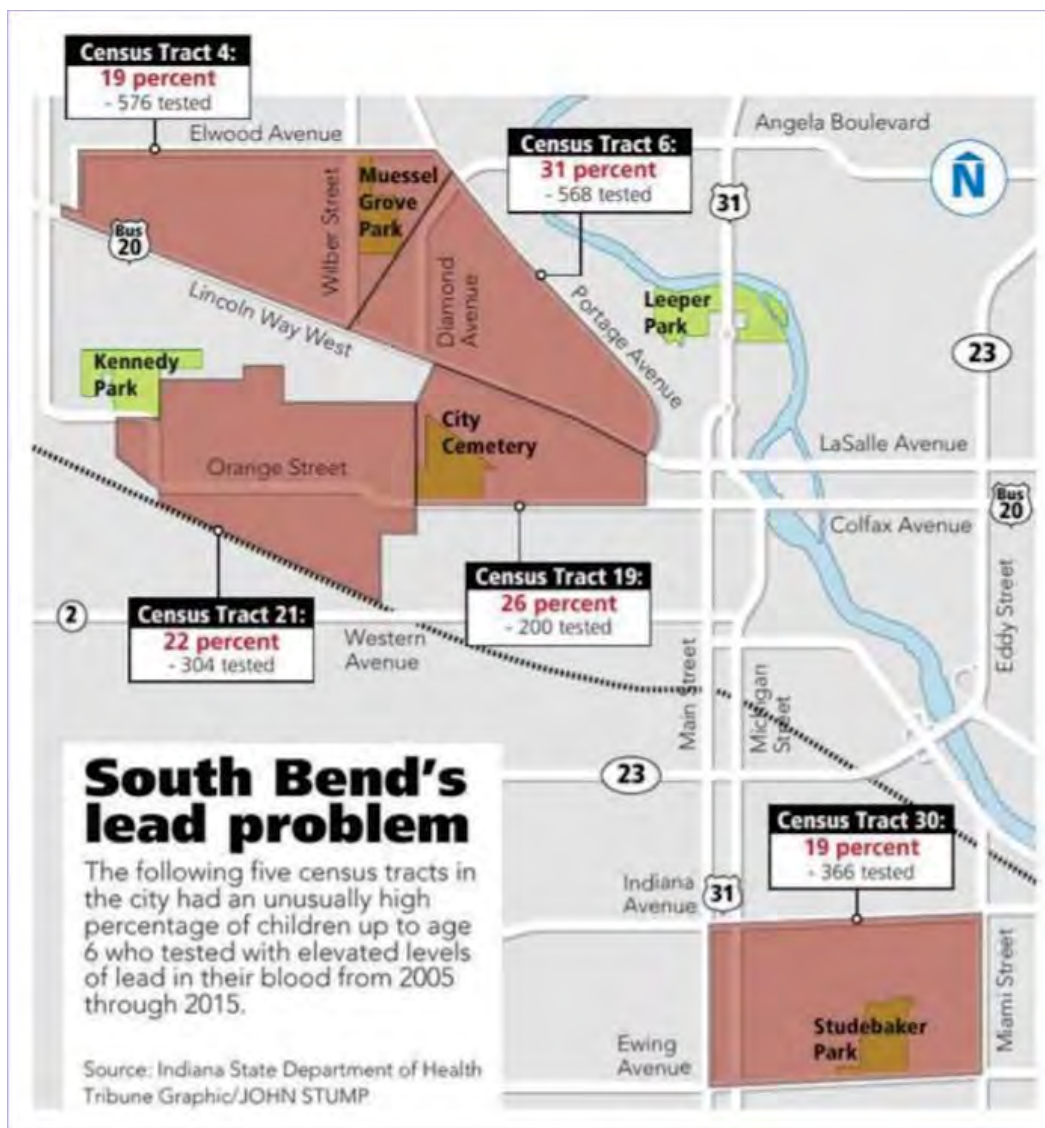


Figure 1: A map of South Bend, with areas of concern noted [2].

1.2 Effects of Elevated Blood Lead Levels

Lead is a known neurotoxin. Blood lead levels above 3 $\mu\text{g}/\text{dL}$ correlate with neurological effects such as poorer motor skills, attention deficit, cognitive function, as well as increased aggravated assault rates 20 years later (see figures 2 and

3) [3]. Low public health funding, particularly in Indiana, where the Department of Health does not intervene until 10 $\mu\text{g}/\text{dL}$ (the EPA recommends intervention at 5 $\mu\text{g}/\text{dL}$, which means Indiana checks on only a small fraction of children) has allowed this issue to linger, and associated societal costs, such as latent crime increases due to lead exposure, will not disappear until lead, particularly in urban environments, disappears.

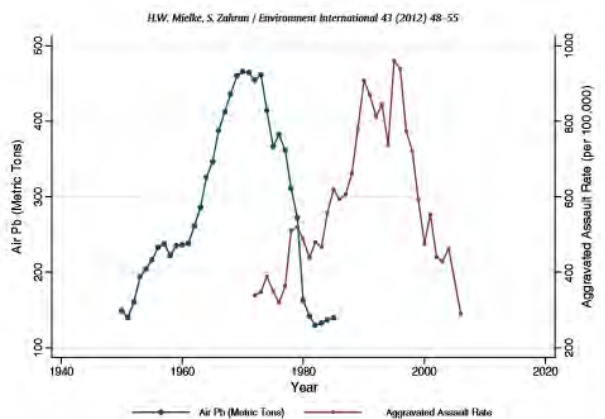


Figure 2: Air lead levels and assault rates.

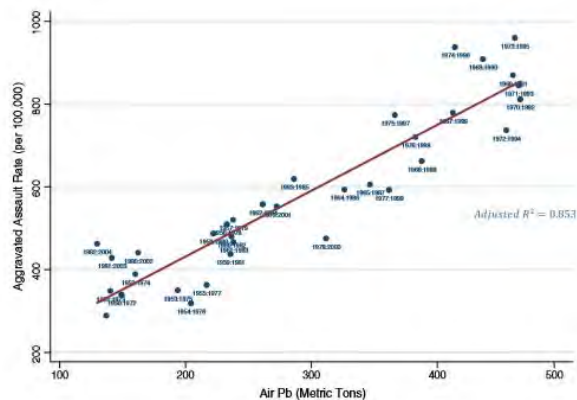


Figure 3: Adjusted for the 22 year offset.

2 Experimental Methods

The Indiana Department of Health has on record a list of children with elevated blood lead levels, and made available a volunteer opportunity for the parents to work with Notre Dame’s lead affinity group. If the parents accepted, a small group would meet with the homeowner to gain their consent in writing, and to gather information concerning the home as well as the children living in it, which included measured blood lead levels, as well as where the children spent most of their time in the house. Over the course of the summer, three vacant lots and seven homes in South Bend were tested.

2.1 Sample Collection

Four or more people typically completed sample collection: one person to operate the X-ray fluorescence (XRF) instrument (wearing a personal dosimeter), one to take soil, dust, and water samples (one 250 mL first-flush sample where the tap has not been run within the past 12 hours, and another after the tap has been running for two minutes), as well as paint chip samples. The other two entered metadata for each sample, such as location, sun exposure, surface type, and other comments along with a photo, into ArcGIS, a web form filled out using iPads provided by the Center for Digital Scholarship (CDS) that stores all necessary data for future analysis.

The teams focused on play areas, chipping paint areas, air vents (which could potentially circulate leaded dust), soldered joints (commonly leaded), and locations with visible amounts of dust or dirt. A robust labeling scheme, where each house was numbered and each sample had a type (S for soil, P for paint, D for dirt, and X for XRF) was used (H05:D02, for example, is the second dust sample at the fifth house). Dust samples were taken by swiping an individually-wrapped alcohol wipe over an 12 inch by 12 inch square (or 12 inch by 2 inch rectangle for tight spaces such as windowsills) so that the concentration of lead can be measured in micrograms per square foot ($\mu\text{g}/\text{ft}^2$). Gloves were worn and switched out between location or room to prevent cross-contamination while taking dust, dirt, and paint samples. Soil samples were taken using a small trowel and placed into conical tubes; the trowel was cleaned using a new alcohol wipe between samples. It was common to take approximately 50 or more XRF samples, 20 dust samples, and two to five paint chip samples. By the end of the summer, a team of four or five could complete an entire house survey in less than two hours.

2.2 Sample Preparation and Analysis

Once all sample collection was complete, soils were dried in an oven at 125°C for two hours, were mixed with 0.05 grams of cellulose to ensure it would remain solid when compressed to a disk, and homogenized using a Fisher Scientific Mini Vortex Mixer in Argos 5 mL microtubes. These samples were then being pressed into 0.5 gram pellets using an MTI Corporation TLJ-15 pellet press at 2000 psi, and analyzed alongside paint chips using the XRF. The leftover soil samples and all of the paint samples were passed onto the chemistry group to be run on ICP-OES, along with the water samples, as the limit of detection for the XRF was in the parts per million range, but the action level for water is in the parts per billion, which is able to be successfully detected by ICP.

2.3 Home Reports

After analysis was complete, a report containing information for all of the samples along with recommendations for intervention and safe practices for reducing lead exposure was sent to each household. A sample is considered to be at a level where action is recommended if it is soil above 400 parts per million (ppm) lead, paint over $5000 \mu\text{g}/\text{g}$ (equivalent to ppm) lead, water over 15 parts per billion (ppb), dust on the floor over $40 \mu\text{g}/\text{ft}^2$, or dust on windowsills over $40 \mu\text{g}/\text{ft}^2$. A level of risk was assigned, either low, moderate, or high, based on how much of a threat each sample posed; high traffic areas or chipping paint were considered higher risk than isolated locations or surfaces that were well-maintained [4].

For high risk areas, photo of the area of concern is included with a short write-up with abatement recommendations for the specific sample. By the end of the summer, once our process was streamlined, this was able to be completed in one to two weeks.

3 Data/Measurement Method

One of the main concerns with using an XRF, particularly one not specialized for lead, is that the readings might not be quantitatively accurate. This can be an issue because if lead is detected above or below the action level, different steps will be recommended than would be recommended by the state. The machine use in this project was supplied by SciAps, model X100-0054, which is one of their baseline products and is not certified for lead abatement. Its advantage is that the unit is significantly cheaper than models that are lead certified, which can be up to three or four times more expensive. These lead certified models are the tool of choice for health departments, as they are guaranteed to be accurate. However, if a cheaper method was found to be effective, the ability to find sources of lead can be increased many fold.

The rapid analysis that the XRF delivers makes it an excellent tool for in-home analysis, as a single sample takes only 30 seconds, with three x-ray beams of ten seconds each at 15, 40, and 50 keV. The X-Ray Tube operates at 40 kV with an Au anode for the default soil matrix, and the detector uses a 20 mm² standard silicon drift detector (SDD), digital pulse processor that operates at DPP 125,000 counts per second, and is live more than 90% of the time.

X-ray fluorescence uses a beam of x-rays to excite and eject electrons in an inner shell, which, due to quantum atomic transitions, have the vacancy filled by an outer-shell electron that, as it de-excites, releases a photon that has an energy characteristic to a particular element. Inductively coupled plasma optical emission spectrometry produces ions and excited atoms that release electromagnetic radiation in a similar manner, which also has a wavelength characteristic of the source element. ICP, however, is a destructive method, which requires dissolving a sample and exposing it to a flame at a temperature of 6000 to 10000 K. A radio frequency (RF) generator produces a powerful magnetic field using a coil (27 or 40 MHz) that ionizes argon gas to plasma, which then collides with electrons of the sample to be analyzed, causing ionization via electron excitation in much the same way XRF operates. This method requires a significant amount of time, requiring several hours to prepare, dissolve, and run a set of samples, compared to the XRF working at 30 seconds per run [5]. It is also not portable, and results are not instantly available, making it less effective in surveying for sources of lead than the XRF.

4 Results

For soil samples, the X100 has shown to have an excellent correlation with both NIST SRM standards ($R^2 = 0.994$) as well as with ICP data for the same soil samples ($R^2 = 0.897$). Compared to ICP and the standards, the XRF provides an excellent correlation. Because of this, our confidence in our discoveries in soils is very high. While the exact sources of lead contamination varied from house to house, soil and old paint, which eventually became dust scattered throughout

homes, were found to universally contain notable amounts of lead. This unit is not calibrated for dust, paint, or metal samples yet. So these sample results remained mostly qualitative.

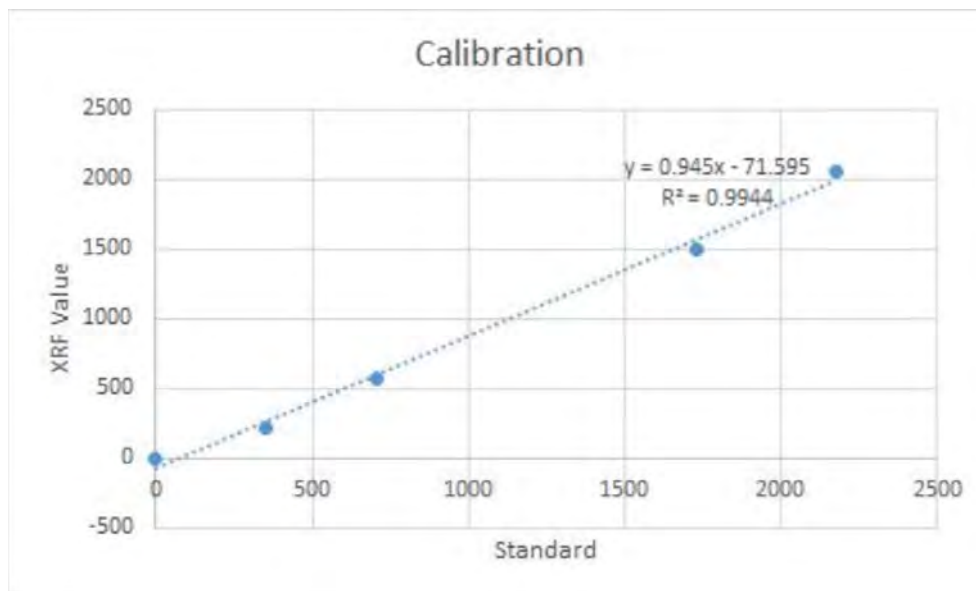


Figure 4: XRF correlate well with NIST soil standards

In all houses, lead paint was found to be present. The XRF is a surface analytical technique, but is able to penetrate several layers of paint. Comparing XRF results to other areas of the house as well as to paint chips taken was an easy way to determine if the most recent layer of paint was leaded; low concentrations in the surface XRF scan and high levels in the lower level paint chip would indicate that the surface paint is safe. However, even if the danger was discovered to be underneath, it was still noted that the wall should be maintained so that the underlying paint is not released into the air or dust. This also includes renovations or drilling, which would cause almost all of the lead to be released into the local environment. If the homeowner opts to remove the leaded paint, it is recommended that they chip it away rather than sand it off, for the very same reasons. They were urged to contact a licensed lead abatement company.

Leaded soil was also found universally, and was found to be highest in the soils next to the houses typically (called the drip line around a house). There were also several locations where soils close to streets and alleys were found to be elevated and this may be correlated with leaded gasoline use. Leaded dust was found in six out of seven homes tested. Along with paint (which can chip away outdoors when exposed to the elements and add to lead in the soil), soil and dust were the other major sources of lead exposure in homes. In order to eliminate these threats, recommendations were made that leaded soil can be covered with new grass, mulch, or stepping stones, and frequent dusting of floors and air ventilation units [6, 7].

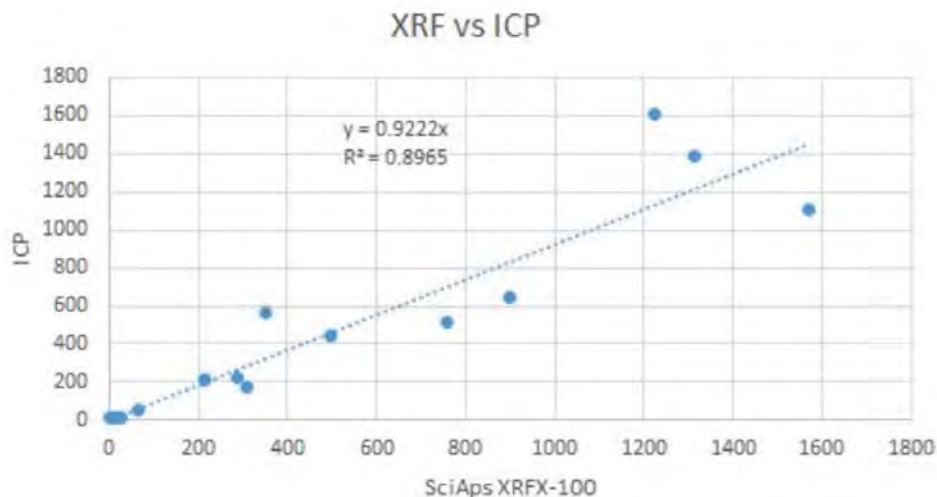


Figure 5: XRF and ICP show comparable results for the same samples.

5 Discussion

Dust samples are not solid nor homogenized. The beam area is only 20 mm², so it is reasonable to assume that it is possible to miss the leaded area or to pick up on the air, which may be the cause of slight inaccuracies, but overall the correlation between ICP and XRF sampling of the same dust wipes is strong.

Penetration depth was also taken into consideration. Contamination across coats of paint was always a concern, so any time a surface was discovered to be leaded, we took a paint chip from as many layers as possible in order to analyze each layer individually so that threat level can be easily determined; if a surface test showed a moderate lead level, but the top layer came back negative and was in good condition, it would be assigned a low threat level.

There was also the possibility for human error. With almost 100 samples for each house, the opportunity to mislabel or mis-enter information was abundant. This was generally avoided by sampling in pairs, and having data entry done by a small group of people as soon as possible after sampling.

5.1 Future Work

The XRF provides rapid and reliable results compared with traditional ICP measurements, so our methodology can be made available to others who have access to the low-cost XRF technology. We plan to work with the city of South Bend to spread awareness about the lead issue, hoping to start programs such as "Mulch Madness" to encourage people to mulch their yards at the start of summer, when kids begin to play outside, reducing seasonal exposure to lead soil.

Additionally, a "citizen scientist" program may begin soon, where we make publicly available our methods, so that people may take samples from their homes and send them in to our laboratory for us to analyze. It takes a lot of time

to organize and complete a household for sampling, but if homeowners send us samples of concern directly, our process would be streamlined so that we can run samples from hundreds or thousands of houses in a summer.

At Notre Dame, there is a new course titled Chemistry in Service to the Community taught by Dr. Marya Lieberman. Students will learn about how lead acts in the body, the epidemiology of lead exposure, medical and regulatory responses to lead, and the analytical principles and laboratory procedures needed to measure lead in paint, dust, soil, and water. We will go to homes where a child has been tested with elevated BLL and help the families identify sources of lead in the home, continuing our work from the summer with additional help.

6 Acknowledgments

None of this would have been possible without leadership of both the South Bend community, including the Near Northwest Neighborhood and Memorial Hospital, as well as Notre Dame faculty. Collaboration spanned across many departments and fields, including the Eck Institute for Global Health, the Notre Dame College of Science, Departments of Chemistry and Physics, the Center for Digital Scholarship, the College of Engineering, and the Indiana University School of Medicine. From the University of Notre Dame, I would like to thank Lacey Ahern, Dr. Heidi Beidinger, Dr. Marya Lieberman, Michael Dowd, Yutong Liu, Christian Allebach, Dr. Matthew Sisk, Noreen Maloney, Aline Irihamye, Jonah Cremin-Ends, Meghanne Tighe, and Dr. Graham Peaslee.

7 References

- [1] Pell, M.B., Schneyer, J. (2016) *The thousands of U.S. locales where lead poisoning is worse than in Flint*. Reuters.
<http://www.reuters.com/investigates/special-report/usa-lead-testing/>
- [2] Booker, T. (2017) *South Bend's stubborn lead problem: Why are kids still getting poisoned?* South Bend Tribune.
- [3] Mielke, H.W., Zahran, S. (2012) *The urban rise and fall of air lead (Pb) and the latent surge and retreat of societal violence*. Environment International. 43: 48-55.
- [4] U.S. Department of Housing and Urban Development. (2012) *Guidelines for the Evaluation and Control of Lead-Based Paint Hazards in Housing*. Ch 7, 13.
- [5] United States Environmental Protection Agency. (1996) *Method 3050B: Acid Digestion of Sediments, Sludges, and Soils*. Revision 2.
- [6] Centers for Disease Control and Prevention. (2017) *Prevent Childhood Lead Poisoning*.
<http://www.cdc.gov/nech/lead5>
- [7] United States Environmental Protection Agency. (2017) *Protect Your Family From Lead in Your Home*.
<http://www.epa.gov/lead>

**Evidence for Two-Phonon
Transverse Wobbling in ^{135}Pr**

Tyler McMaken

2017 NSF/REU Program

Physics Department, University of Notre Dame

Advisor: *Dr. Umesh Garg*

Abstract

Evidence is presented for a second transverse wobbling band in ^{135}Pr , the first two-phonon wobbling band to be observed outside of the $A \sim 160$ region of the nuclear chart. The wobbling nature of the nucleus, a unique indicator of triaxiality, is characterized by the $\Delta I=1$, $E2$ nature of the linking transitions between the band and its one-phonon counterpart, and its transverse nature is characterized by a decrease in the wobbling energy as angular momentum increases. In addition, the analysis of high-statistics data yields more precise measurements of angular distributions across the level scheme. Throughout the analysis, steps have been taken to improve methodologies in calibration, background subtraction, and mixing ratio extraction techniques for future use.

I. BACKGROUND/THEORY

Atomic nuclei have been observed in most cases to have a spherically symmetric shape in their ground state. However, at higher spin states, this spherical shape may become deformed, and for some nuclei, their ground states already take on a deformed shape. Most nuclear deformations have an oblate or prolate shape, being flattened or stretched at the poles, respectively, while remaining symmetric and axial in shape. But for a few small regions in the nuclear chart (e.g. around $Z = 72, N = 94$ and $Z = 60, N = 76$), their nuclei have been observed to have a triaxial shape; i.e., all three axis have different lengths [1][2].

Evidence for triaxiality can be found by analyzing the rotational bands of a nucleus. As an axially asymmetric nucleus rotates, it begins to wobble about its precession path [3]. This can be interpreted as an alignment of a quasiparticle of high angular momentum within the nucleus to an axis of the core of the nucleus, causing the total angular momentum to wobble

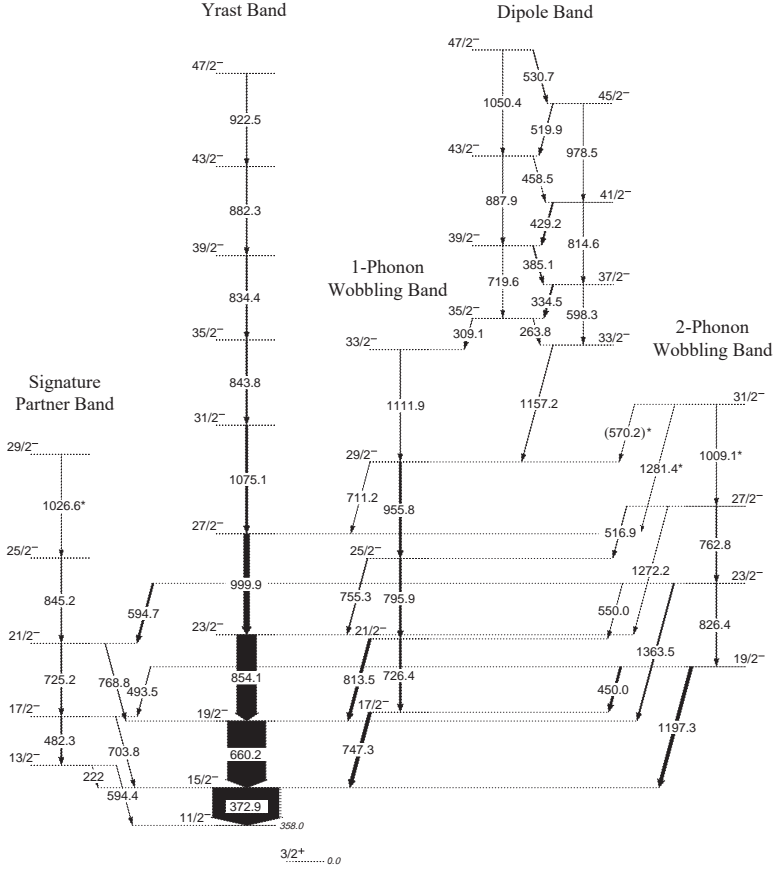


FIG. 1. Partial negative parity level scheme developed for ^{135}Pr . Gamma ray energies are given in keV, and the spin I and parity π are shown for each level as I^π . Transitions denoted with an asterisk (*) indicate gamma rays not seen prior to the present analysis.

about that axis. A wobbling mode will give rise to a band of energy levels which can be seen through gamma emission. In some cases, more than one wobbling band has been observed in the same nucleus, corresponding to an additional degree of freedom characterized by the quantum number n_w . This quantum number takes on non-negative integer values, and it corresponds to the number of phonons (i.e. vibrational modes) present in the system. The different wobbling bands for ^{135}Pr can be seen in Fig. 1. The $n_w=0$ band is labelled “Yrast” (a term for the band whose levels have the lowest energy for a given spin), and the $n_w=1$ and $n_w=2$ bands are correspondingly labelled as the one-phonon and two-phonon bands, which display the wobbling nature of ^{135}Pr and therefore indicate its triaxiality.

Two observables are used here to quantify the wobbling nature of ^{135}Pr . The first is the measurement of the wobbling energy, the amount of additional energy in the nucleus required for higher-mode wobbling to occur at a given spin I . Experimentally, the wobbling energy for an energy level within a wobbling band can be calculated as follows [2]:

$$E_{wob} = E(I, n_w) - \frac{E(I - n_w, n_w = 0) + E(I + n_w, n_w = 0)}{2}. \quad (1)$$

Theoretical models of nuclei initially predicted that the wobbling energy should always increase as spin increases within a given band. However, when the first wobbling bands were investigated, the experimental wobbling energies gave the opposite trend, decreasing as the spin increased. This discrepancy has since been explained by [Frauendorf and Dönau](#), who described how one can distinguish between cases of longitudinal and transverse coupling depending on, respectively, whether the quasiparticle aligns parallel to or perpendicular to the core's axis with the largest moment of inertia (the unstable intermediate axis) [4]. Though alignment parallel to this axis allows the quasiparticle to gyroscopically turn about a more stable axis, in the case of transverse wobbling, the quasiparticle instead aligns perpendicular to this axis. As more angular momentum is added to a transverse wobbling, rotation about the intermediate axis becomes favored over a transverse axis at some critical angular momentum, and thus the wobbling frequency decreases until the wobbling is transferred over to the longitudinal case. Hence, a decrease in the wobbling energy as spin increases is indicative of transverse wobbling.

The second observable which is used to quantify the wobbling nature of ^{135}Pr is the $E2/M1$ mixing ratio, δ . For a transition which contains an admixture of two different multipolarities, the mixing ratio is defined as

$$\delta = \sqrt{\frac{I_\gamma(L')}{I_\gamma(L)}}, \quad (2)$$

where I_γ is the gamma ray intensity of multipole nature L or $L' = L + 1$ for a given mixed transition [5]. Since radiation with $L > 2$ does not generally make a significant contribution, δ here is given with $L' = 2$ and $L = 1$, so that it corresponds to the ratio of electric quadrupole ($E2$) radiation to magnetic dipole ($M1$) radiation. Most of the inter-band transitions shown in Fig. 1 with $\Delta I = 1$ and $\pi_f = \pi_i$ should predominantly have an $M1$ nature with very small contributions from higher-order radiation; however, linking transitions between wobbling bands are distinctive in that they are highly mixed, showing significant contributions from $E2$ radiation. Following directly from Eq. 2, the percentage of contribution from $E2$ can be expressed as $\%E2(/100) = \frac{I_\gamma(E2)}{I_\gamma(M1)+I_\gamma(E2)} = \frac{\delta^2}{1+\delta^2}$, so that wobbling bands can easily be distinguished by their high $\%E2$ (typically much greater than $\sim 50\%$). The value of δ can be found by analyzing angular distributions, since the gamma ray intensity $W(\theta)$ should follow

$$W(\theta) \propto 1 + a_2 P_2(\cos\theta) + a_4 P_4(\cos\theta) + \dots, \quad (3)$$

where P_λ are the Legendre polynomials with coefficients $a_\lambda = \frac{F_\lambda^{L,L} + 2\delta F_\lambda^{L,L'} + \delta^2 F_\lambda^{L',L'}}{1+\delta^2} \rho_\lambda$ for F -coefficients obtained from Wigner-3j and Wigner-9j symbols and ρ -coefficients obtained from Clebsch-Gordan coefficients and magnetic substate probabilities $P_m(I)$ [5]. The latter probabilities cancel out to yield $a_\lambda = 0$ when λ is odd since substates are assumed to be aligned ($P_m(I) = P_{-m}(I)$), hence the exclusion of odd- λ terms in Eq. 3 [6]. Thus, the parameters a_2 and a_4 obtained from a fit of $W(\theta)$ (higher-order terms are negligible) depend on I_i, I_f, L, L' , and, most pertinent to this analysis, δ .

II. DATA/METHODOLOGY

The data for this analysis were obtained from an experiment conducted with the Gammasphere at Argonne National Laboratory. In the experiment, the levels of interest were populated through the fusion-evaporation reaction $^{123}\text{Sb}(^{16}\text{O},4n)^{135}\text{Pr}$ with a beam energy of 80 MeV. The resulting gamma rays were observed using 83 Compton-suppressed Ge detectors arranged in rings at 17 different polar angles. Because of the symmetry of the observed angular distributions (see Eq. 3), the data were folded into seven rings covering the $\theta = 0^\circ$ to $\theta = 90^\circ$ range to decrease statistical uncertainty.

Since each ring has a different number of detectors and each detector varies across energies in its efficiency to collect data at a given energy, a calibration was carried out using a ^{152}Eu target. In each ring, the ten strongest peaks in the resulting energy spectrum were fitted to the known energies and intensities of the gamma rays from ^{152}Eu , and an efficiency ϵ as a function of energy E (in keV) was fitted with the parameters A–G to the formula $(\ln[\epsilon])^{-G} = (A + B(\ln[\frac{E}{100}]) + C(\ln[\frac{E}{100}])^2)^{-G} + (D + E(\ln[\frac{E}{100}]) + F(\ln[\frac{E}{100}])^2)^{-G}$ using the Radware package [7]. Fig. 2 shows the ^{152}Eu peak intensities and fitted efficiency formulae for the seven folded rings.

To allow for higher precision measurements, spectra were filtered by applying a gate on a transition energy below the transition of interest, so that the only peaks left in the spectra are those in coincidence with the gated transition. Because Gammasphere's detectors observe with a time window of 120 ns and excited nuclear states have half lives on the order of picoseconds or less, all gamma rays produced from the cascade from an excited nuclear state down to the ground state will be observed instantaneously; i.e., in coincidence with one another [8].

^{152}Eu Efficiency Calibration

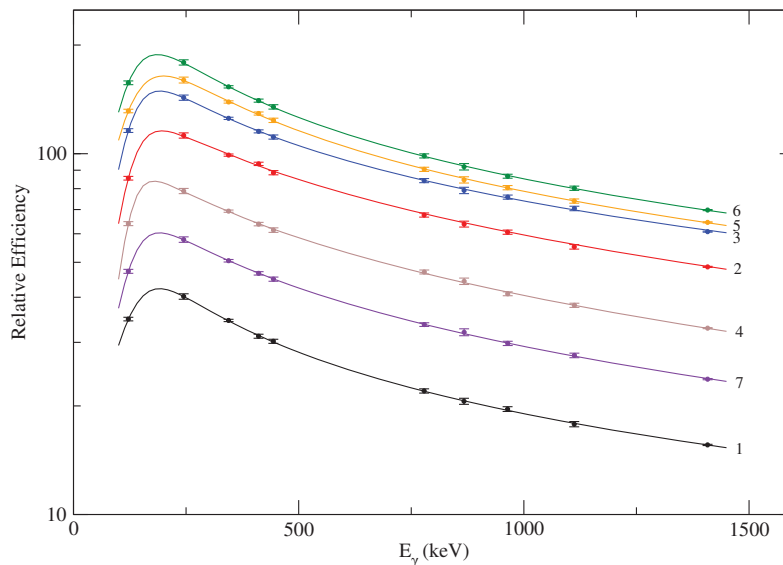


FIG. 2. Efficiency calibration for 7 rings of detectors. Ring numbers labelling each curve correspond to polar angles of 17.27° (1), 34.55° (2), 50.07° (3), 58.28° (4), 69.82° (5), 79.95° (6), and 90° (7).

Care must be taken when gating to subtract background properly, since a gate on an energy peak will result in a spectrum with background gamma rays in coincidence with the peak as well as gamma rays in coincidence with the background in the gated energy window. The former background spectrum which must be subtracted is obtained by fitting underneath the peaks using a Radware algorithm, and the latter spectrum is simply the total spectrum scaled by the gated energy peak's background-to-total ratio [9].

III. ANALYSIS/RESULTS

To confirm the wobbling nature of the rightmost band in Fig. 1, the angular distributions for the lowest three $n_w=2 \rightarrow n_w=1$ transitions are plotted in the first three panels of Fig. 3. As mentioned in section I, evidence for wobbling in these $\Delta I=1$ transitions comes from their $E2$ nature, which can be quantified using mixing ratios extracted from fits of

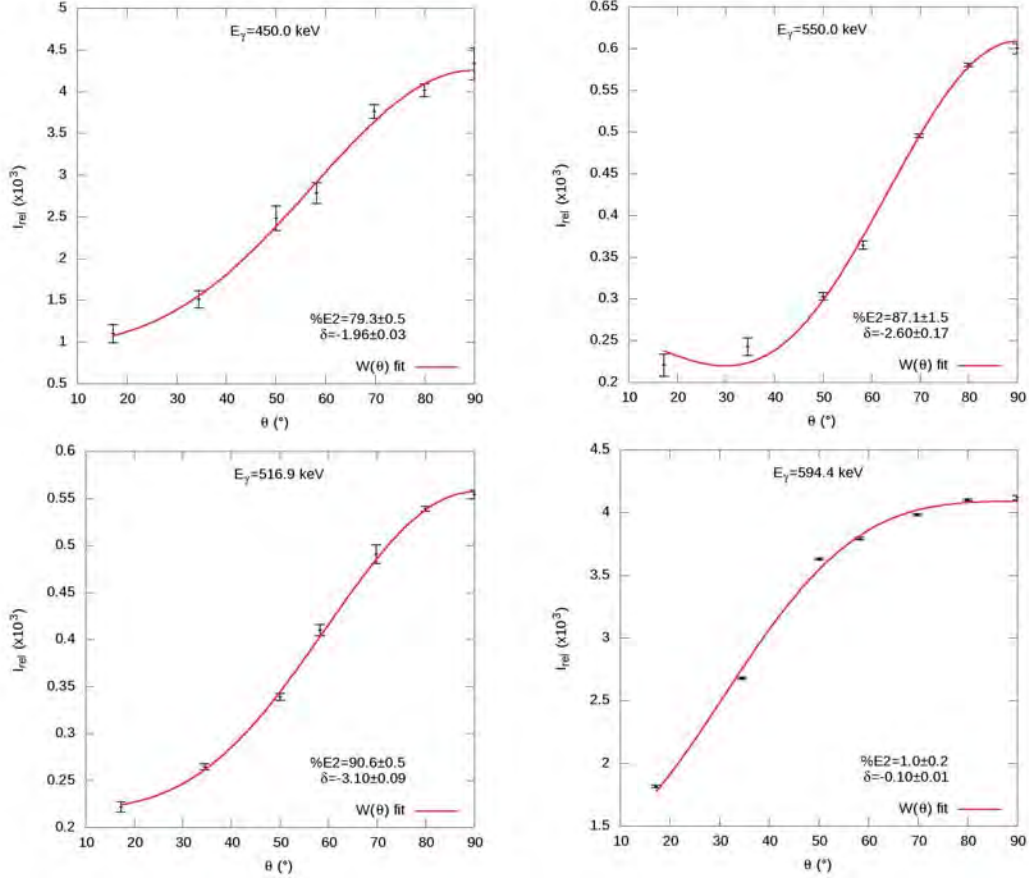


FIG. 3. Relative gamma peak intensities for the $n_w=2 \rightarrow n_w=1$ transitions: $\frac{19}{2}^- \rightarrow \frac{17}{2}^-$ (top left), $\frac{23}{2}^- \rightarrow \frac{21}{2}^-$ (top right), $\frac{27}{2}^- \rightarrow \frac{25}{2}^-$ (bottom left); and the signature partner to yrast transition $\frac{13}{2}^- \rightarrow \frac{11}{2}^-$ (bottom right).

Eq. 3 (the red curves in Fig. 3) to the data. In the case of the $E_\gamma = 450$ keV transition, two mixing ratios with comparable chi-square minima are found, at $\delta = -1.96 \pm 0.03$ and $\delta = -0.39 \pm 0.01$, but the latter is rejected based on the trends seen in other transitions and results from previous investigations of the transition [5]. The resulting mixing ratios and $\%E2$ admixtures are shown to be in agreement with what is predicted for a wobbling band. The first $n_w=2 \rightarrow n_w=1$ transition has a $79.3 \pm 0.5\%$ contribution from $E2$ radiation, the second transition has $87.1 \pm 1.5\%$ $E2$ contribution, and the third transition has an even higher admixture, with $90.6 \pm 0.5\%$ $E2$. To ensure that other interband transitions are of substantially different character when subjected to the same analysis, the angular distribu-

tion for the lowest signature partner to yrast band transition is shown in the bottom right panel of Fig. 3. As expected, this transition is found to be principally $M1$, with less than 2% of an admixture of $E2$ radiation.

In order to confirm the transverse nature of the two-phonon wobbling band, the wobbling energy as defined in Eq. 1 is plotted in Fig. 4 along with the wobbling energy of the one-phonon wobbling band. The trend for both bands

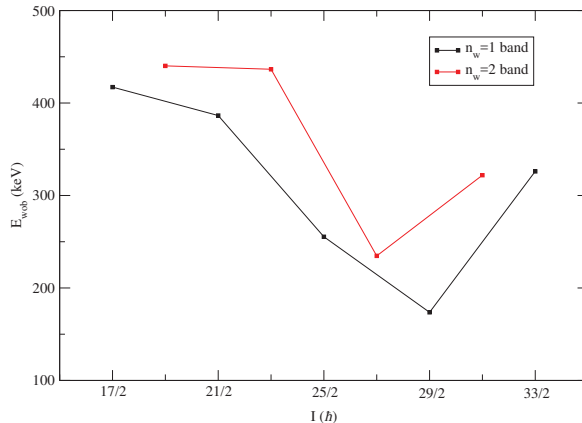


FIG. 4. Wobbling energy as a function of spin for the $n_w=1$ (blue) and $n_w=2$ (red) bands in ^{135}Pr .

clearly shows a decrease in the wobbling energy as spin increases,

exactly what is expected for transverse wobbling. As predicted, at high enough spins (around $\frac{27}{2}-\frac{29}{2}$), the wobbling energy begins to increase as the odd quasiparticle aligns with the longitudinal axis of the nuclear core.

IV. CONCLUSIONS

The present analysis of the negative parity transitions in ^{135}Pr has achieved higher statistical precision in measurements of angular distributions and DCO-like ratios than previous investigations of this nucleus. The $n_w=1$ wobbling band is analyzed with smaller confidence intervals than previously obtained, and its interband transitions to the yrast band are confirmed to be highly admixed. In addition, the signature partner band is seen with greater precision, albeit still sparsely populated. Most importantly, with evidence for $\Delta I=1$, $E2$ $n_w=2 \rightarrow n_w=1$ transitions, a second transverse wobbling band is shown conclusively to exist

in ^{135}Pr . This conclusion shows that ^{135}Pr is robust enough to support multiple phonons, and as this is the first observation of multiple-phonon wobbling outside of the $A\sim 160$ region of the nuclear chart, it definitively confirms that transverse wobbling with $n_w > 1$ is not confined to a single region of the nuclear chart.

V. ACKNOWLEDGMENTS

I thank PhD candidate Nirupama Sensharma, whose continual assistance proved to be invaluable to my research. I would also like to thank Dr. Umesh Garg for advising me and for working with Nell Collins and Lori Fuson to facilitate the Research Experiences for Undergraduates (REU) Program. This work was carried out through the University of Notre Dame Physics Department REU Program, which is funded by the U.S. National Science Foundation (NSF) [Grant No. PHY-1559848].

-
- [1] S. W. Ødegård *et al.*, *Phys. Rev. Lett.* **86**, 5866 (2001)
 - [2] J. T. Matta *et al.*, *Phys. Rev. Lett.* **114**, 082501 (2015)
 - [3] A. Bohr and B. R. Mottelson, *Nuclear Structure, Vol. II* (Benjamin, New York, 1975)
 - [4] S. Frauendorf and F. Dönau, *Phys. Rev. C* **89**, 014322 (2014)
 - [5] J. T. Matta, *Exotic nuclear excitations: The transverse wobbling mode in ^{135}Pr* , Ph.D. thesis, University of Notre Dame (2015)
 - [6] T. Yamazaki, *Nuclear Data Tables* **3**, 1 (1967)
 - [7] D. C. Radford, “Notes on the use of the program gf3,” (2000)
 - [8] G. Knoll, *Radiation Detection and Measurement* (Wiley, 2000)
 - [9] K. Starosta *et al.*, *Nucl. Instr. Meth. Phys. Res. A* **515**, 771 (2003)

Particle-Induced Gamma-ray Emission Spectroscopy Over a Broad Range of Elements

Hannah Olds

2017 NSF/REU Program

Physics Department, University of Notre Dame

Advisor: Dr. Graham Peaslee

Abstract

Ion beam analysis is a common application of nuclear physics that allows for elemental and isotopic identification of target materials via light ion beams. One of the best known ion beam analysis techniques is Particle-Induced Gamma-ray Emission (PIGE) spectroscopy, which can be used ex vacuo to identify the elements of interest in almost any solid target. The energies of the gamma-rays emitted by excited nuclei will be unique to each element and depend on its nuclear structure. For the most sensitivity, the accelerated ions should exceed the Coulomb barrier of the target, but many isotopes are known to be accessible to PIGE even below the Coulomb barrier. We explore PIGE sensitivity across the periodic table by analyzing measurements made with 3.4 MeV protons on targets containing elements with $Z = 9, 11-17, 19-25, 27-30, 35, 37, 44, 47, 53, 60, 62, 73,$ and 74 . These measurements will be used as a basis for comparison with higher-energy proton beams available at the University of Notre Dame's St. Andre accelerator when it comes online this Fall. The beam normalization technique of using atmospheric argon and its 1459 keV gamma-ray to better estimate the integrated beam on target will also be discussed.

1 Introduction

Particle-Induced X-ray Emission (PIXE) and Particle-Induced Gamma-ray Emission (PIGE) spectroscopy are similar methods of ion beam analysis. PIXE involves using light ions to excite or eject the electrons in an atom, which will then emit characteristic X-rays when returning to ground state. This works well over a large range of the periodic table at relatively low bombarding energies, and allows us to identify individual elements. However, this method is insensitive to isotopic and chemical information in the target. PIGE is a similar technique, but the ions are used to excite the nuclei of the target elements, which often requires a higher beam energy. An excited nucleus holds

much more energy than an excited electron, and the deexcitation of the target will emit gamma-rays instead of X-rays in this process. A typical emitted X-ray detected using PIXE will be 0-30 keV, while the average emitted gamma-ray detected using PIGE is 110-8000 keV.

Two positively charged nuclei, in this case a nucleus and a proton, will have an electrostatic potential energy which causes them to repel each other. The strength of this potential depends on the charge of the target nucleus squared; the higher the charge the greater the repulsion. The Coulomb barrier is the energy barrier that must be overcome by the nuclei in order to get close enough for the nuclear forces to interact. As a result, exciting the nuclei of heavier elements can be a challenge. Despite the added difficulty, PIGE still has value as a method of identification because of its ability to not only identify elements, but also distinguish between isotopes due to its interaction with an element's nucleus.

We have used PIGE to analyze 28 different elements with a 3.4 MeV proton beam produced by the tandem accelerator at Hope College. To begin, preliminary PIGE results were compared to those at 2.4, 3.1, and 3.8 MeV from previous experiments done by Räsänen [1] and Kiss [2]. Once the energy calibration was set, the energies of previously unidentified peaks could be determined. We then ran a second set of targets, including elements which had not yet been tested at 3.4 MeV. The relative sensitivity for a wide range of elements was compared to literature values [1-2] and will be used as a basis for comparison with new PIGE measurements made at higher proton energies of up to 6 MeV at the Notre Dame St. Andre tandem accelerator.

2 Methods

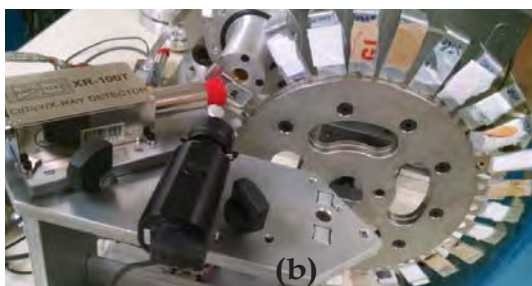
2.1 Experimental Setup

Targets were made from between 200 and 500 mg of selected powdered compounds, and pressed into pellets about 3 mm thick with a diameter of roughly 10 mm using a pellet press (Figure 1a). The pressure applied by the press to form the pellet was 1500 psi, or 1035 N/cm^2 . For the compounds which would not hold together well enough to form a pellet, cellulose was added and the mixture was then homogenized before pressing. When possible, a compound containing the target element as an oxide was used. This is preferable, because oxygen peaks are not detectable with our capabilities; the emitted gamma-rays are typically too high energy for our detector, and the few energies we can detect have counts too low to be noticeable. Without oxygen peaks showing up, we ensure the visible peaks come either from background or our target element.

Once pressed, the pellets were mounted onto slides, and the slides were inserted into the target wheel (Figure 1b). The wheel was placed approximately 3 cm away from the detector. We used a solid-state high purity germanium (HPGe) detector, placed at an angle of approximately 75 degrees from the beam to and minimize Doppler broadening.



(a)



(b)

Figure 1: a) Pellet press with all parts separated. b) Target wheel holds mounted targets in line with the beam.

Each target was irradiated with about 10 nA of protons for 120 seconds, with few exceptions. Occasionally, target elements were sensitive enough to produce high yields at large rates, and in order to preserve the detector the run time was shortened. This occurred in B and NaHCO₃, which were both stopped after seven seconds. Ta₂O₃ was lengthened to 180 seconds due to a previous run of 120 seconds producing only very small yields. A beam striking only air was also run at 30, 60, 90, 120, and 180 seconds in order to analyze background peaks.

2.2 Analysis

As gamma radiation passes through the detector, pulses of electrons are released that are proportional to the gamma-ray energy. These pulses are converted by an Analog-to-Digital Converter (ADC) into "channels" recorded in a data acquisition system. The number of channels these energies can be divided up into depends on the resolution of the detector, indicating how well it can distinguish differences in received signal. The signal is then amplified electronically such that 2048 channels represent gamma-ray energies up to 1745 keV.

After the allotted beam time for each target, the integrated counts per energy channel were collected. The analysis was done using a program written in Interactive Data Language (IDL), which allows us to determine both the channel containing the centroid of each peak and the number of counts in each peak above a linear background subtraction. See Figure 2. The goal is then to match the given channel values of the centroids to the gamma-ray energies they represent.

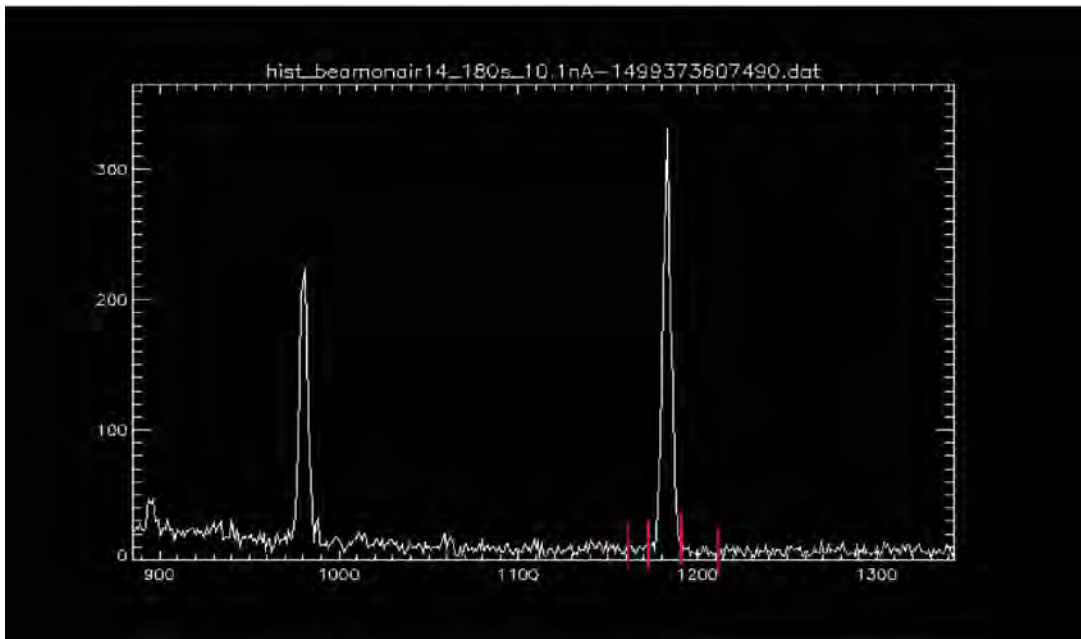


Figure 2: A section of the detector output; counts vs channel. The red bars show the selection of a peak for analysis in IDL. The centroid of this peak was calculated to be at channel 1182, and corresponds to the Al gamma-ray with an energy of 1014 keV.

Initially, the tables produced by Räsänen [1] and Kiss [2] were used for peak identification. When the literature failed to identify a recorded peak, an online database containing results from previous PIGE experiments, the Ion Beam Analysis Nuclear Data Library (IBANDL) [3], was used. Peaks from the background were also identified by running beams on air. These peaks were created by argon, aluminum, and positron annihilation. The peaks from argon can be attributed to the roughly one percent composition of argon in dry air, while peaks from aluminum can be attributed to scattering from an exit window frame or target frames containing aluminum. These known background peaks, as well as peaks from a 860 ppm NaF standard, were used for peak calibration. The following table compares their energies and the corresponding channels:

| Source | F | Al | Na | anh | Al | Al | Al | Ar | F |
|---------|-----|-----|-----|-----|-----|------|------|------|------|
| Energy | 110 | 171 | 440 | 511 | 844 | 1014 | 1369 | 1459 | 1634 |
| Channel | 110 | 182 | 499 | 585 | 980 | 1183 | 1603 | 1713 | 1915 |

Creating a scatter plot of the few known gamma-ray energies vs the channels at which they

appear makes it possible to use the slope and intercept of the resulting trend line to calculate each channel's corresponding energy. In Figure 3, the calibration curve is shown. This is a reliable method of producing accurate energy values, as the R^2 value is a near-perfect regression.

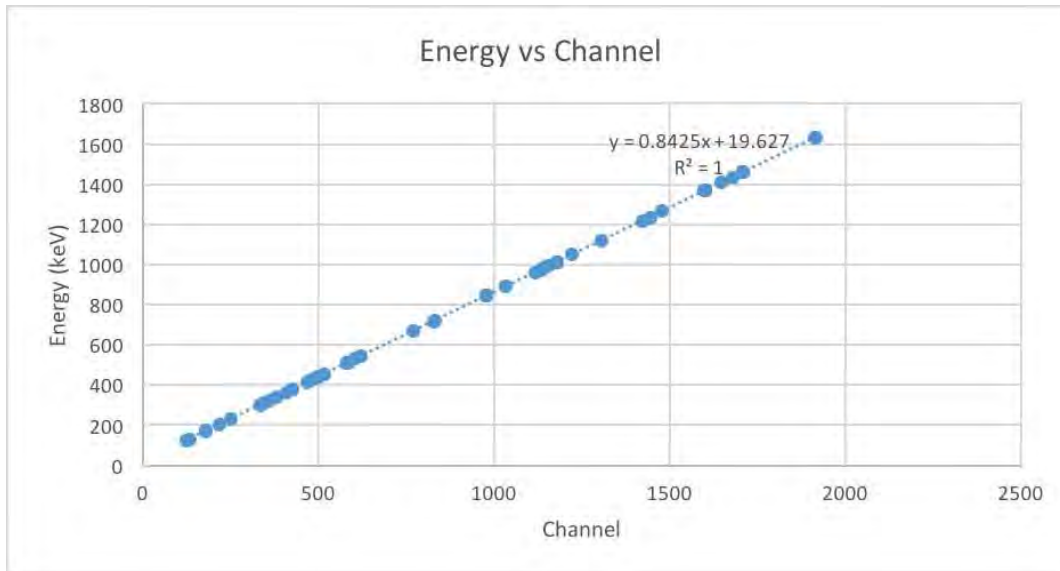


Figure 3: Gamma-ray energies in keV are plotted against the channel numbers at which the centroids of the peaks are located. The trend line shows each channel's corresponding calculated energy.

3 Results

3.1 Argon Peak for Beam Normalization

It is important to know the average beam current, because a higher current will naturally produce higher counts given the same amount of beam time. As a result, it is necessary to ensure counts are higher in some elements due to that element's sensitivity, and not a more intense beam current or longer run time. So, for each run both the initial current and the run time were recorded. These were typically around 10 nA and 120 seconds, respectively. Since the current is constantly fluctuating, there will usually be an error to the number being read at any given moment when manually recorded. To get an accurate average, we must allow the computer to do a minute of

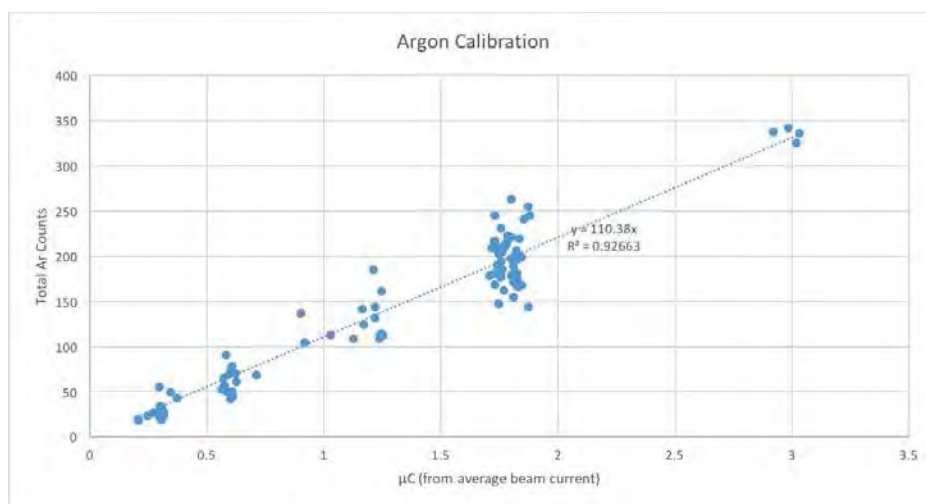


Figure 4: Relationship between counts of argon and charge.

calculation. If this was done every time a target was run, it would take up a significant amount of our time. To avoid this problem, we note that for all runs of at least 30 seconds, the argon present in the air produced a 1459 keV peak.

When beam current is multiplied by the run time, it produces a value for beam charge. Plotting the charge vs the detected argon counts produces a trend line which directly correlates argon counts to the beam's charge for that run. See Figure 4. The variance from the trend line some data points exhibit in Figure 4 can be attributed to the error which results from manually recording the current. This relationship removes the necessity of recording beam current, saving time as well as increasing accuracy.

3.2 Sensitivity of Various Elements

Because different amounts of beam time and different beam currents will also affect how many counts of each gamma-ray energy are detected, a comparison between sensitivity of elements can only be made accurately if this is properly corrected for. To avoid this problem we consider the counts seen per charge in units of micro-coulombs. This makes up for any current and run time

differences because the charge is a product of the current and beam time, which the counts will then be divided by to produce a value for the "yield" of each gamma-ray energy.

However, this is not yet completely representative, since the percent by mass of the element of interest in the target also affects the counts detected. Without correcting for this, a comparison between sensitivities of elements from both our results and those from other papers could not be made. Once the percent by mass of the element of interest in the target was calculated, the corresponding counts were adjusted to represent what would have been seen if a 100 percent pure target had been used.

Recently, another method of using argon peaks has also been developed to allow us to produce more accurate yields. We first adjust the counts to represent what would be emitted from a pure target. Then the counts of argon from each run can be normalized to 150, and the counts from all remaining peaks in each run should be adjusted by the same factor as its corresponding argon peak. The adjusted counts should then be divided by the value for beam current corresponding to the 150 argon counts. This correlation was shown previously in Figure 4, and the value will be $1.369 \mu\text{C}$. Figure 5 compares the sensitivity of all elements tested after these adjustments have been made.

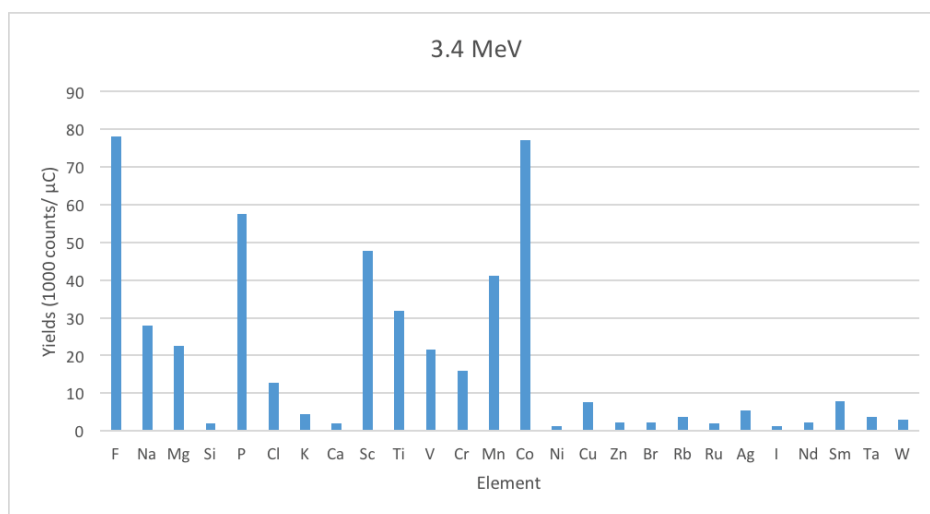


Figure 5: Sensitivity of elements examined; demonstrated by displaying yields in units of 1000 counts per micro-coulomb for each element. The counts have been adjusted to represent what would have been seen using a pure target, and the yields account for differences in beam current and run time.

In this figure, the elements are listed by increasing Z value. In general, lighter elements are more sensitive up to nickel. As expected, the elements tested with magic number Z values, Ca and Ni, are among the least sensitive. Although we did run a target containing aluminum, Al has been left out due to the increased counts detected from the background. When the beam interacts with the accelerator, there is no reliable way to determine what percent of these interactions are with aluminum, so we can't accurately correct the yields to make up for this.

4 Discussion

We have identified many of the elements most sensitive to PIGE at 3.4 MeV. These include F, Co, P, Sc, Mn, Ti, V, Cr, Na, and Mg. This suggests that PIGE may be a useful technique in screening samples for these elements in the future. In a few of the targets, some energy peaks could not be identified with the literature or online resources. New targets should be made out of these elements, and they should be run again to see if the same peaks are still present. If they are, it is less likely to be target contamination and more likely to be target element peaks which have not yet been identified.

4.1 Future Work

When the new tandem accelerator is brought online at the University of Notre Dame in the fall, we will be able to produce a 6 MeV proton beam. We will then use similar methods and the same targets to run tests at a higher energy in an attempt to better analyze heavier elements. The results should add to the information available about gamma-ray yields found in various elements. This information can then be added to databases such as IBANDL, in order for future researchers to compare energy peaks produced by a target of unknown composition against those produced by

known elements. In addition, the method of using the argon peak for beam normalization will be put in to practice.

References

- [1] Räsänen, J. and Hänninen, R. Heavy element ($Z > 30$) thick-target gamma-ray yields induced by 1.7 and 2.4 MeV protons. *Nuclear Instruments and Methods in Physics Research*, 205(1), (1983) pp.259-268.
- [2] Kiss, A., Koltay, E., Nyakó, B., et al. *Journal of Radioanalytical and Nuclear Chemistry, Articles*, 89|1 (1985) 123-141.
- [3] <https://www-nds.iaea.org/exfor/ibandl.htm>

Investigating Implicit Bias in Letters of Recommendation for a
High School Physics Camp

Allison J. Olshefke

2017 NSF/REU Program

Physics Department, University of Notre Dame

Advisor: Dr. Micha Kilburn

Abstract

In this study, 1,725 teacher recommendations for high school applicants to the Physics of Atomic Nuclei program were analyzed for possible gender biases. Text supplied by the teachers was examined for key terms that previous studies identified as indicators of gender bias in letters of recommendation for STEM professional and academic positions. This study compares the qualitative and quantitative assessments in the recommendations for consistency across gender, especially focused on grindstone and ability terms. Research has shown that, in the United States, academic fields whose practitioners emphasize aptitude over hard work have fewer women Ph.D.'s. This is especially true in physics, which both emphasizes brilliance and has one of the lowest percentages of women Ph.D.'s. This study aims to investigate whether this discrepancy exists at the high school level, as an invisible barrier for female students pursuing STEM opportunities. Results indicate that when comparing applicants who were rated equivalently in the quantitative portion of the recommendation, female students were more likely to be described with grindstone terms and male students were more likely to have their natural ability described in a recommendation. These differences become more significant when looking only at highest-rated students. These results suggest that gender bias in physics letters of recommendation is present at the high school level: a time when letters of recommendation are crucial for college and scholarship applications. Further research should be done to investigate the prominence of these biases in other high school related contexts.

Introduction

The underrepresentation of women in science, technology, engineering, and math (STEM) is a widely acknowledged issue in the United States, and the underrepresentation of women in physics is particularly acute. Although it is in the national interest to train more physicists, “women are underrepresented at all levels of the field” (Sax, Lehman, Barthelemy, & G., 2016, p.1). This includes high school, where female students are less likely to take and pass AP exams, and college, where the physics major has one of the lowest representations of women (Sax et al., 2016).

The purpose of this study is to investigate whether teacher recommendations for the Physics of Atomic Nuclei summer camp (PAN) exhibit implicit language biases based on student gender. Significant differences in letter composition that affect the perception of male and female candidates’ hireability have been discovered in applications for different STEM professional and academic positions. These differences include the frequency of gender terms (Trix & Psenka, 2003), communal and agentic descriptions of the candidates (Madera, Hebl, & Martin, 2009), and the frequency of standout adjectives used (Schmader & Whitehead, 2007).

Another discrepancy noted by multiple studies is the tendency for male applicants to be described using terms that highlight their inherent ability or natural brilliance, while female applicants’ hard work and determination are emphasized (Schmader & Whitehead, 2007). This disparity is especially detrimental to women in physics. Leslie, Cimpian, Meyer, and Freeland (2015) analyzed the relationship between female representation in various academic fields in the United States and each field’s emphasis on the importance of inherent ability as a predictor of success in that field. Physics has the lowest number of female Ph.D.’s, and the third highest emphasis on brilliance. This implies that candidates whose letters of recommendation have fewer ability words and more grindstone words are less likely to be seriously considered for a position in a physics setting because those

candidates would be viewed as less likely to succeed in physics.

Although high school is a time when letters of recommendation become increasingly important for college, scholarship, and other applications, no research has been done investigating whether these biases may affect high school students interested in physics. These biases have the potential to create an invisible barrier for female students' participation in physics opportunities before they even have a chance to enter physics at the postsecondary level.

Physics of Atomic Nuclei

PAN is a week long summer camp for high-achieving high school students interested in advanced nuclear physics. This camp is sponsored by the Joint Institute for Nuclear Astrophysics - Center for Evolution of the Elements. Two camps are held each summer, one at the University of Notre Dame and one at Michigan State University. PAN accepts 44 out of 200+ applicants each year and imposes gender parity at each location. This removes the impact of gender biases since females are only compared to females and males to males.

Method

Recommendations

Part of the PAN application requires recommendations from two different, student-selected teachers. Teachers complete an on-line form that collects quantitative information on the student as well as optional qualitative comments (see Appendix A). The 1,725 recommendations analyzed in this study are aggregated from all 2013-2017 student applications. There are 1,123 male and 602 female recommendations. The recommendations were de-identified by the Primary Investigator before analysis. The only personal information retained was student gender. The gender of the recommendation writer was not noted, as past studies have found it to be insignificant (Moss-Rascuin, Dovidio, Brescoll, Graham, & Handelsman, 2012).

Data Collection

A codebook of key words and phrases for each relevant category was compiled based on previous literature and expanded with new, related terms and phrases (Madera et al., 2009; Moss-Rascuin et al., 2012; Schmader & Whitehead, 2007; Trix & Psenka, 2003) (see Appendix B).

Context Fitting

One advantage of this study is that each letter was manually analyzed to ensure that no keywords were missed or collected in an inappropriate context by algorithms. This also prevented skipping key terms due to inconsistencies like typos or different permutations of phrases. This manual approach provides greater accuracy than the Linguistic Inquiry and Word Count algorithm used by Madera et al. (2009) and Schmader and Whitehead (2007) which can only detect sentiment probabilistically.

Results

There are no statistically significant differences between all male and female students' letters in gender terms, communal orientation, agentic orientation, or standout adjectives. When only students who were rated with mostly "exceptional" scores in the quantitative portion of the application are considered (see Appendix A), more gender disparities can be seen (see Figure 2). Grindstone terms and ability words show significant gender differences in the entire set and most highly rated subset of students.

Grindstone Terms

A Mann-Whitney U test revealed a significant difference in the presence of grindstone terms for female ($Md = 1$, $n = 540$) and male ($Md = 0$, $n = 1025$) students' letters of recommendation, $U = 246153$, $p < .001$, $r = .11$ (see Figure 1). Eleven percent more female than male students were described with grindstone terms.

These differences are still significant and present to about the same effect size when only the highest level students are considered. A Mann-Whitney U test reveals a significant

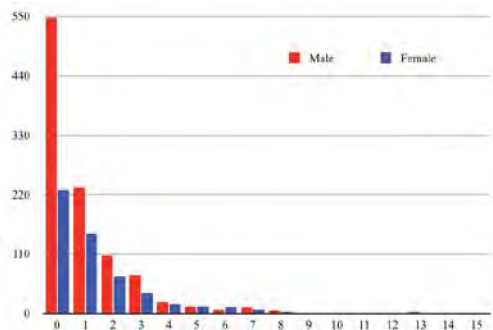


Figure 1. A frequency distribution of grindstone terms by gender for all letters.

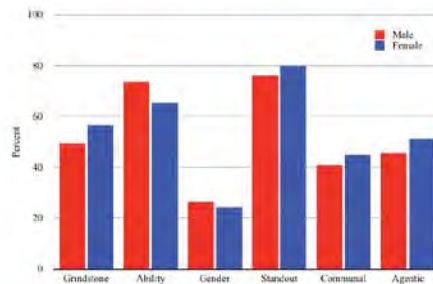


Figure 2. The percentage of "exceptional" applicants' letters that contain one or more words of a given category.

difference in the presence of grindstone terms for female ($Md = 1, n = 291$) and male ($Md = 0, n = 536$) students' letters of recommendation, $U = 72325, p = .047, r = .10$.

Ability Terms

Conversely, there is no significant difference between the presence of ability words for the entire population of male and female students' letters ($p = .073$). However, when only the highest level students' letters are analyzed using a Mann-Whitney U test, there is a statistically significant difference in the the number of ability terms used in female ($Md = 1, n = 291$) and male ($Md = 1, n = 536$) students' letters, $U = 70261, p = .015, r = .08$. This is concerning because quantitatively, teachers have ranked these students to be at functionally the same ability level and have given them the highest recommendation. Yet male students' ability is being highlighted more frequently in more letters. 73% of male students are described with one or more ability term, compared to only 65% of female students (See Figure 2). Because these students are rated so highly, they are the most likely to have the academic skills and motivation to succeed in physics. It is problematic that the most driven and talented female high school students are the ones affected most prominently by the invisible barrier created by implicit bias in the letters.

Discussion

The results of this research confirm that significant gender differences are present in high school letters of recommendations. In some ways, this bias is similar to bias found at the professional and academic levels in terms of grindstone and ability words, but different patterns are seen as well. Unlike the findings in Schmader and Whitehead (2007), the frequency of standout adjectives was not relevant. In fact, more female than male high school students had at least one standout adjective in their letter in this study. Additionally, unlike the findings in Madera et al. (2009) there was no statistically significant difference between male and female students' communal or agentic orientation according to their letters. This could be because the teaching profession relies on both agentic and communal skills equally, and teachers are therefore more likely to comment on both those qualities in the recommendations; whereas, in academia, an agentic orientation is perceived as more important than a communal one (Madera et al., 2009). Schmader and Whitehead (2007) found no significant gender difference in the frequency of grindstone and ability words in letters of recommendation for biochemistry positions, but gender differences with respect to those terms were significant at the high school level.

The differences in results between the findings of this study and previous studies are important to note. Recommendation writers should be aware of the impact that their language choices can have on applications in difference contexts. While grindstone tendencies may seem like a positive trait in a classroom setting, emphasizing them in a letter for a STEM opportunity can be detrimental to an applicant's success.

More research is needed investigating whether biases like the ones found in this study are present in other high school contexts. Because PAN accepts gender parity and a small percentage of total applicants, no conclusions can be drawn about whether this language bias affects the selection of candidates for high school physics programs. Additional research should investigate whether these implicit language biases prevent female applicants from entering other STEM-gateway opportunities.

References

- Leslie, S., Cimpian, A., Meyer, M., & Freeland, E. (2015). Expectations of brilliance underlie gender distributions across academic disciplines. *Science*, *347*(6219), 262-265. doi: 10.1126/science.1261375
- Madera, J. M., Hebl, M. R., & Martin, R. C. (2009). Gender and letters of recommendation: Agentic and communal differences. *Journal of Applied Psychology*, *96*(6), 1591-1599. doi: doi:10.1037/e518532013-658
- Moss-Rascuin, C., Dovidio, J. F., Brescoll, V. L., Graham, M. J., & Handelsman, J. (2012). Science faculty's subtle gender biases favor male students. *Proceedings of the National Academy of Sciences of the United States*, *109*(41), 16474-16479. doi: 10.1073/pnas.1211286109
- Sax, L., Lehman, K. J., Barthelemy, R. S., & G., L. (2016). Women in physics: A comparison to science, technology, engineering, and math education over four decades. *Physical Review Physics Education Research*, 1-17.
- Schmader, T., & Whitehead, V. H., J. and Wysocki. (2007). A linguistic comparison of letters of recommendation for male and female chemistry and biochemistry job applicants. *Sex Roles*, *57*(7-8), 509-514. doi: 10.1007/s11199-007-9291-4
- Trix, F., & Psenka, C. (2003). Exploring the color of glass: Letters of recommendation for female and male medical faculty. *Discourse and Society*, *14*(2), 191-220. doi: 10.1177/0957926503014002277

Appendix A

Recommendation Form

1. Please evaluate the student for the following attributes among students you have taught. *(The following questions are multiple choice with the options "Cannot assess," "Below average," "Average," "Above average," and "Exceptional")*¹

- Demonstrates strong academic integrity
- Exhibits curiosity by asking questions
- Shows initiative in seeking answers to questions
- Quickly recognizes and understands conceptual relationships
- Applies concepts to new materials
- Seeks intellectual challenges
- Works well in group settings
- Demonstrates a strong work ethic
- Works well independently
- Generates a large number of ideas or solutions to problems
- Overall quality

2. Overall recommendation *(Multiple choice with options "Highest recommendation," "Recommended without reservations," "Recommended with reservations (please make comments below)," and "Not recommended for program (please make comments below)")*

3. Use this space to make any comments that you would like the PAN committee to know about this applicant. While we do not request letters, you can copy and paste text here if you have one written.

¹In 2013-2015, the multiple choice options were "Top 1%," "Top 5%," "Top 10%," "Top 50%," and "Bottom 50%"

Appendix B

Codebook

| Category | Key Terms |
|---------------------|--|
| Grindstone | dedicat*, disciplin*, work(s) (ing) (ed) hard, hard work*, perserv*, careful, methodical, detail*, meticulous, work ethic, thorough, focus, conscientious, responsib*, effort, reliab*, organiz*, busy, diligen*, persist*, determin* |
| Ability | intell*, analytical, skill, ability/abilities, bright*, creativ*, with ease, skill, talent, innate, natural, easily, capabl*, effortless, insight, prowess, analytical, brilliant, insight, smart, capacity, intuitiv*, sharp, gift*, aptitude, innovative, proficient, precocious |
| Standout Adjectives | excellent, *est, outstanding, exceptional, extremely, super, most, extraordinar*, stellar, superb, wonderful, tremendous, ideal, phenomenal, unparalleled, remarkable, rare, impeccable, fantastic, stellar, amazing, unique |
| Gender | gentleman, lady, man, woman, Mr., Ms., Miss, girl, boy, guy |
| Communal | kind, caring, polite, cooperative, help*, popular, accepts instruction, accepts feedback, accepts criticism, collaborat*, mentor, interpersonal, social, tutor, works well in groups, personable, well-liked, likable, amiable, tactful, nice, warm, empath*, sympath*, supportive, approachable |
| Agentic | leader, achiev*, active, earn*, confident, gain*, initiative, inventive, inspir*, influen*, aggressive, assert*, contribut* |

Table B1

Key terms for each category searched for in letters of recommendation. A '' indicates that any word containing the partial word should be counted*

Analysis of Phase-Imaging
Ion-Cyclotron-Resonance Mass Measurements at
Argonne National Lab

William Porter

2017 REU Program

Physics Department, University of Notre Dame

Advisors:

Ani Aprahamian

Abstract

The importance of accurate mass measurements is evident in quite possibly the most famous equation in all of physics: $E = mc^2$. In the realm of nuclear physics, the well-known method of adding up the protons, neutrons, and electrons falls short of giving the true mass of the atom, neglecting the binding energy of the nucleus. Thus, further studies into nuclear structure are warranted, and are especially relevant for nuclear astrophysics in the study of the r-process. The primary contemporary tool for determining the mass of an ion with high precision is the Penning trap. This is a very small device that creates a quadrupole electric field that, when coupled with a homogenous magnetic field, only allows motion in the radial plane, causing ions to “orbit” the center of the trap. One of the newest methods for increasing the precision of a measured mass with the Penning trap is known as the Phase Imaging technique [1]. Using this technique, the measurement of nuclear masses is accomplished by measuring the cyclotron frequency of the isotopes circling within the trap. To determine this frequency, a position-sensitive multichannel plate (MCP) detector is used to record the relative position of the isotope in the trap as a function of time. Using these time-dependent position measurements, the center of the trap, the central angles between the positions of the isotope of interest and a measured reference spot are used to determine the cyclotron frequency and, subsequently, the nuclear mass.

1 Introduction

Due to advances in nuclear astrophysics and other related fields, the investigation of nuclei has been pushed from the valley of stability further and further towards the nuclear driplines. Thus, as more measurements of heavy, short-lived nuclei are needed, faster and more improved measurement techniques are required. Presently, three different techniques exist to measure such short-lived nuclei: Schottky, Isochronous, and Penning trap mass spectrometry. Schottky mass spectrometry provides accurate measurements of nuclei with half-lives down to 10^0s , with an approximate uncertainty of $10keV$. Isochronous mass spectrometry provides measurements of nuclei with half-lives down to $10^{-6}s$, albeit with an uncertainty of around $100keV$ [2]. Thus, for nuclei with half-lives less than a second, Penning trap mass spectrometry (PT-MS) becomes the go-to method for obtaining nuclear mass measurements [3]. Penning traps are small devices that employ the use of a quadrupole electric field and a magnetic field, as seen in *Fig. 1*, to confine an ion’s movements to exclusively radial motion. The earliest successful Penning trap mass measurement technique was the Time-of-Flight Ion-Cyclotron-Resonance (TOF-ICR) technique, which, despite recent advances in its precision, ultimately fall short of the desired mass resolution for masses with

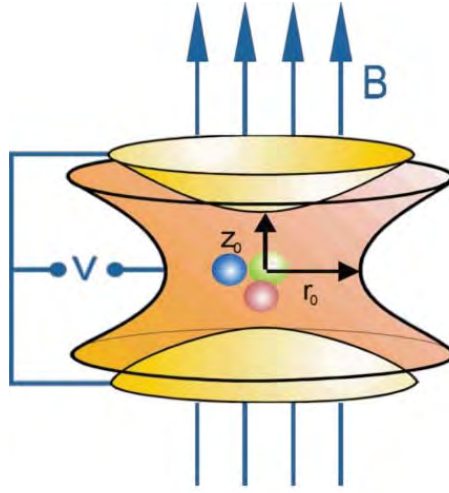


Figure 1: A model of a Penning trap, where B denotes the magnetic field and V is the potential difference applied to the electrodes of the trap, which create the quadrupole electric field. z_0 and r_0 are the spatial dimensions of the trap [4].

half-lives less than $10^{-1}s$ [5]. Thus, experimentalists have recently turned to the Phase-Imaging Ion-Cyclotron-Resonance (PI-ICR) technique, which provides significant speed and mass resolution improvements over the TOF-ICR technique [1]. The PI-ICR technique relies on the determination of the cyclotron frequency ν_c , accomplished by a position-sensitive microchannel plate (MCP) detector. The cyclotron frequency itself is a combination of two radial frequency components, the modified cyclotron frequency (ν_+), and the magnetron frequency (ν_-). The modified cyclotron frequency, the standard cyclotron motion of an ion in a magnetic field but weakly affected by the electric field, is greatly mass dependent, whereas the magnetron frequency, which is affected greatly in the radial direction relative to the electric field, is weakly mass dependent. Together, they relate to the cyclotron frequency as follows:

$$\nu_c = \nu_+ + \nu_- \quad (1)$$

Subsequently, the cyclotron frequency is related to the nuclear mass through the following:

$$\nu_c = \frac{qB}{2\pi m} \quad (2)$$

where q is the charge of the ion, B is the magnetic field, and m is the nuclear mass.

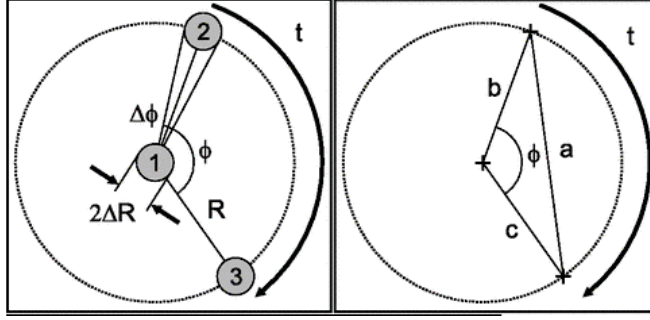


Figure 2: A diagram of the radial motion of an ion within the measurement trap.

2 PI-ICR Measurements at Argonne National Lab

At Argonne National Lab, the Canadian Penning Trap (CPT), in combination with a ^{252}Cf source from the Californium Rare Isotope Breeder Upgrade (CARIBU), is used for high-precision mass measurements of nuclides in the rare earth region. Ions are transferred into the CPT at a spatial range $2\Delta R$ (Pos. 1 in *Fig. 2*). By applying a dipolar rf field, the ions are moved outward an average radius R (Pos. 2 in *Fig. 2*). The ions are then allowed to freely evolve for a period of time t , such that the final phase of the ion is:

$$\phi + 2\pi n = 2\pi vt \quad (3)$$

where n is the number of turns the ion made within the trap (or the number of full revolutions around the trap it completed), and v is the “radial motion” frequency, or the frequency due to the radial motion of the ion within the trap. Other traps which have utilized the PI-ICR technique, such as SHIPTRAP in Darmstadt, Germany, measure the two components of the cyclotron frequency in succession, such that $v = v_-$ for one run and then $v = v_+$ for the next [1]. However, for the CPT, $v = v_c$, such that our cyclotron frequency can be measured as a function of the final phase (ϕ), the number of turns (n), and the time of free evolution (t), as seen below:

$$v_c = \frac{\phi + 2\pi n}{2\pi t} \quad (4)$$

When conducting mass measurements, we regularly measure reference ions, and then analyze the final phase of the ions in question in reference to our most recent reference ion measurement.

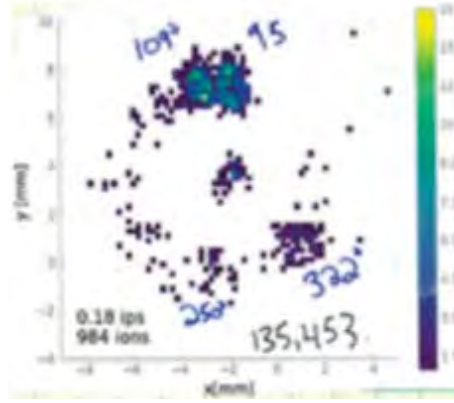


Figure 3: An experimentally recorded projection of the positions of ions within the trap, specifically for ^{159}Nd in this case. Notice the large accumulation of events around $\phi_a = 95$, signaling that our actual measurement's final phase is most likely around that value.

For the sake of avoiding confusion, we will refer to the ions we are interested in measuring and observing as the actual ions from here on. Thus, the final phase can be written as $\phi = \phi_a - \phi_{ref}$, where ϕ_a is the final phase of the actual ion and ϕ_{ref} is the final phase of the reference ion. Furthermore, we measure the time t as a function of the accumulation time (t_{acc}) of the actual ion. However, this measurement is also done with respect to the most recent reference ion measurement, and thus allows us to say that $t = t_{acc,a} - t_{acc,ref}$, where $t_{acc,a}$ and $t_{acc,ref}$ are the accumulation times of the actual and reference ions, respectively.

3 Analysis

Analysis of PI-ICR measurements begins by determining the x and y coordinates of the center spot at which ions have accumulated. *Fig. 3* shows an example of an experimentally recorded projection of ionic motion onto the MCP. Using MATLAB, we are able to fit Gaussian distribution curves to our positional spot data, giving us the positional coordinates of the final spot center. We repeat this process for various different sets of actual ions, traditionally looking at ion sets with accumulation times within 1ms of each other, as well as for the reference measurements which the actual measurements will be referenced to. We then calculate the final phase of both the actual and reference ion sets (ϕ_i) from their positional spot data, such that:

$$\phi_i = \arccos\left(\frac{b^2 + c^2 - a^2}{2bc}\right) \quad 0 \leq \phi \leq \pi \quad (5)$$

$$\phi_i = 2\pi - \arccos\left(\frac{b^2 + c^2 - a^2}{2bc}\right) \quad \pi < \phi < 2\pi \quad (6)$$

where a, b , and c are the distances illustrated in *Fig. 2*. Now equipped with the phases of the ion accumulation spots, and considering that we already have the time t of free evolution, we need to determine the number of turns n that the ion went around the trap. To do so, we start by waging a guess at the cyclotron frequency, where we say that:

$$v_c = \frac{v_{c(cal)}}{m} \frac{q}{q_{cal}} (m_{cal} - q_{cal}m_e) + qm_e \quad (7)$$

where $w_{c(cal)}, q_{cal}$, and m_{cal} are the cyclotron frequency, charge and mass of a calibrant isotope, traditionally a well-known nuclide, and are taken from AME2012 [6]. m_e and q are the mass of an electron and the charge of the measured isotope, respectively, and also taken from AME2012. This leaves only the mass of the measured isotope m , which we say is simply the sum of the masses of its consistent protons and neutrons. This clearly ignores the binding energy of the nucleus, and thus is why the resulting cyclotron frequency is only a guess. However, considering that the ignored mass defect is relatively small, we can use our cyclotron frequency guess in conjunction with the final phase (ϕ) and time (t) in *Eqn. 4* to calculate an approximate number of turns n . We then calculate v_c for a range of integer values for n around our approximate guess value. From here, we traditionally choose the cyclotron frequency value closest to our guess. To find our final nuclear mass m , we traditionally eliminate the magnetic field term in *Eqn. 2* by instead looking at cyclotron frequency ratios, and thus simply utilize a rearrangement of *Eqn. 7*, such that:

$$m = \frac{v_{c(cal)}}{v_c} \frac{q}{q_{cal}} (m_{cal} - q_{cal}m_e) + qm_e \quad (8)$$

and use our newly chosen cyclotron frequency as v_c .

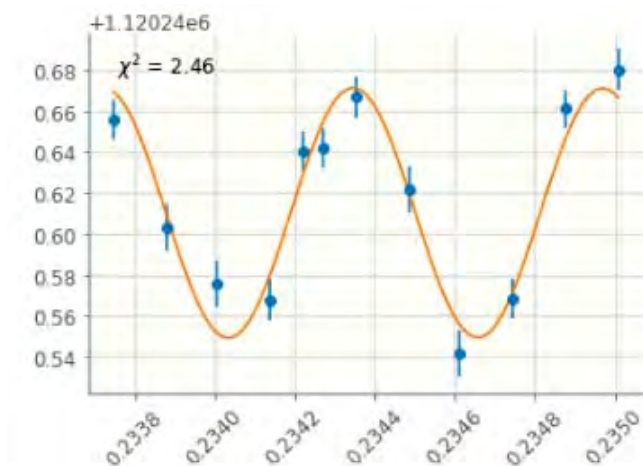


Figure 4: A graph of accumulation time vs. cyclotron frequency for C6H6 measured in May 2017.

4 Results and Sine Wave Fitting

When calculating the cyclotron frequency and nuclear mass of a measured isotope, we run analyses at various different accumulation times, and thus produce different cyclotron frequencies and nuclear mass values for each measurement made at a different accumulation times. Ideally, these values should be consistent. However, recent analyses have shown that cyclotron frequency seems to vary sinusoidally with respect to the accumulation time. Although not fully understood yet, we believe that the variance has to do with the magnetron frequency (w_-), as the period of this sinusoidal variance is close to the magnetron frequency traditionally seen in the CPT. *Fig. 4* shows a plot of a recent analysis of C6H6 measured in May 2017, with accumulation times all approximately 234ms. To correct for this variance, we fit a sine function ($a + b \sin(cx + d)$) to our accumulation time/cyclotron frequency data, where a, b, c , and d are all fitted variables. The resulting variable a , the “center” of the sine fit, is then taken to be our final cyclotron frequency.

5 Conclusion

As more precise mass measurements are needed in nuclear physics, more precise ways of measuring short-lived nuclide have arisen, specifically the PI-ICR technique in PT-MS. Using the CPT at Argonne National Lab in combination with the PI-ICR technique, we are able to get accurate measurements of nuclides with half-lives much less than a second. However, further work is most

certainly warranted, as issues with cyclotron frequency variance continue to arise. Further refinement of analysis techniques will be necessary, as we must take into consideration the dependence of our measured cyclotron frequencies such that we can continue to produce reliable, accurate mass measurements farther and farther from the valley of stability.

6 Acknowledgements

I would like to thank my advisor, Prof. Ani Aprahamian, for her help on this project. I would also like to thank Rodney Orford and Trenton Kuta for their extensive help on the analysis process. Finally, I would like to thank Prof. Umesh Garg for putting on the 2017 Notre Dame Physics REU Program. This work has been supported by the University of Notre Dame's College of Science and the National Science Foundation under contract PHY-1205412.

References

- [1] S. Eliseev, K. Blaum, M. Block, C. Droese, M. Goncharov, E. Minaya Ramirez, D. A. Nesterenko, Yu. N. Novikov, and L. Schweikhard, *Phys. Rev. Lett.* **110**, 082501 (2013)
- [2] B. Franzke, H. Geissel, and G. Münzenberg, *Mass Spectrom. Rev.* **27**, 428 (2008).
- [3] K. Blaum, *Phys. Rep.* **425**, 1(2006)
- [4] A. A. Kwiatkowski, G. Bollen, M. Redshaw, R. Ringle, and S. Schwarz. *Int. J. Mass Spectrom.* **379**, 9 (2015).
- [5] S. George, K. Blaum, F. Herfurth, A. Herlert, M. Kretzschmar, S. Nagy, S. Schwarz, L. Schweikhard, and C. Yazidjian, *Int. J. Mass Spectrom.* **264**, 110 (2007).
- [6] G. Audi, M. Wang, A. Wapstra, F. Kondev, M. MacCormick, X. Xu, and B. Pfeiffer, *Chinese Physics C* **36**, 1287 (2012).

SN 1992A Progenitor Investigation Through Late Time Light Curve Analysis

Cian Roche

August 12, 2017

Supervisor: Prof. Peter Garnavich
2017 NSF/REU Program
Physics Department, University of Notre Dame
May 23rd - August 11th 2017

Abstract

By analysing images in the V and B bands from HST and CTIO, a light curve was obtained for SN 1992A extending to almost 1000 days past V band maximum, with an upper limit at ~ 1700 days. By fitting a model of ^{56}Ni , ^{56}Co and ^{57}Co decay to the light curve, a relative isotopic abundance of $^{57}\text{Co}/^{56}\text{Co} = 0.025_{-0.08}^{+0.09}$ was obtained. This result was compared to that of Shappee et al. (2017) in which a similar analysis was conducted for SN 2011fe, a far better observed type Ia supernova. The abundance ratio found strongly prefers the lower central progenitor density of double degenerate models, as was found in the case of 2011fe.

1 Introduction

Type Ia supernovae (SNe Ia) are primarily classified by the features of their spectrum near maximum luminosity such as a lack of Hydrogen and Helium signatures, and a strong absorption line near 6100\AA . Other secondary classification criteria such as light curve shape, color evolution, and host galaxy morphology are also used for confident SNe Ia identification. These particular SNe exhibit remarkably consistent light curves and spectra, with the light curves reaching maximum in 15-20 days and a tight correlation between this peak brightness and various measures of the light curve development speed (Phillips, 1993). This uniformity means that SNe Ia have been invaluable as cosmological distance indicators, being used to provide the first evidence for the acceleration of the cosmic expansion (Riess et al., 1998), (Perlmutter et al., 1999) for which the 2011 Nobel prize in physics was awarded.

Despite being relied upon as "standard candles" in many scenarios, the progenitor systems of SNe Ia are still unknown. Progenitor models traditionally focus on getting a C/O white dwarf (WD) to ignite by approaching or exceeding the Chandrasekhar mass, M_{Ch} . Currently, there are two main classes of progenitor models: The single degenerate (SD), in which a

degenerate primary accretes matter from a nondegenerate secondary, causing the primary to approach M_{Ch} , and double degenerate (DD), in which a tight binary system of degenerate WDs merge through loss of energy and angular momentum to gravitational waves. Both models differ in their relative isotopic yields due to a lower central progenitor density in the DD scenario. This allows for an inference of the most likely progenitor system based on a relative isotopic yield, as is presented in this report.

2 Method

2.1 Raw Data

In order to construct the B and V band light curves for SN 1992A, images were taken from the HST WFPC2 and CTIO telescopes and analysed in order to obtain magnitudes for SN 1992A up to 1000 days past V band maximum in both bands. Work by Nick Suntzeff on the CTIO images has already produced a robust light curve up to 600 days past V_{max} , and so a late time magnitude and an upper limit were added to this light curve using HST WFPC2 images. Unfortunately SN 1992A is not very well observed past this 600 day point, although several images in the B and V bands were taken by ESO in 1993 and 1994 of NGC 1380, many of these images did not contain the supernova, and those that did were not usable. This increases the error in the final results, as a relatively small amount of data is available.

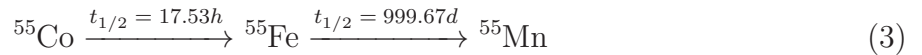
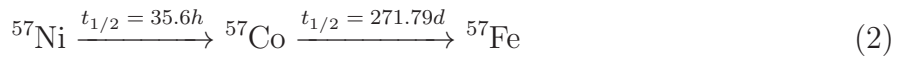
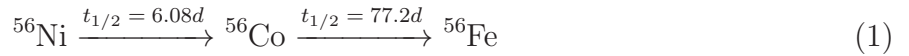
2.2 HST Photometry

In performing photometry on the HST images, corrections had to be made in order to obtain an accurate apparent magnitude. The first of these was the aperture correction, which was calculated by taking the average of the $\Delta m_{3,6}$ (Difference in magnitude between a 3 pixel

and 6 pixel aperture) for the 5 brightest stars in the region of NGC 1380 in each image. The error associated with this correction was taken as the 1σ RMS deviation from the mean of the $\Delta m_{3,6}$ values. The magnitudes also had to be converted from the STMAG system to Johnson UBVRI which assumed the supernova has the same colour as an A0 V type star.

2.3 Radioactive Decay Model

A model was created which calculates the apparent magnitude observed in the decay of a certain initial mass of ^{56}Ni , following the decay chains in equations 1-3. The masses of ^{57}Ni and ^{55}Co are taken as relative abundances to this initial ^{56}Ni mass. The goal of this project was to determine these ratios and use this to infer a progenitor density.



In the model, only the contributions due to eq. 1 (represented by subscript 56) and the ^{57}Co to ^{57}Fe decay (represented by subscript 57) were included. This is because the contribution due to eq. 3 is relatively small and would not influence the light curve until ~ 2000 days past maximum, when the ^{55}Fe decay becomes the primary source of flux, and also because the half life of ^{57}Ni is so short that it has no impact on the late time light curve. The early portion of the light curve is not important to fit well, as there are many unaccounted for factors here which become unimportant at late times ($\gtrsim 600$ days).

The energy available due to the decay of each isotope (accounting for the coupling of ^{56}Ni and ^{56}Co) as a function of time is derived by Jeffery (1999), and the constants used in eq. 4 were calculated by Hayden et al. (2010). The energy was split into two portions, one for the

decay chain described in eq. 1, and the other for the ^{57}Co to ^{57}Fe decay. M_{Ni} is the initial synthesised ^{56}Ni mass, t is the elapsed time in days, the denominator of each exponential is the lifetime of each isotope in days, α is the relative abundance of ^{57}Co to ^{56}Ni , the factor of 0.83 represents the ratio between energy in electrons and the total energy for a ^{57}Co decay, the remainder of which is x-rays. Using the decay energies presented in Seitenzahl et al. (2009), the ratio of the energy of the Auger electrons and internal conversion electrons to the total energy (ie. including x-rays) was taken to obtain the 83% factor. The ratio of electrons and positrons in ^{57}Co to that in ^{56}Co was taken to obtain the factor of 6.5, allowing for the ^{57}Co energy to be calculated based on the ^{56}Co constant.

$$E_{56} = M_{Ni} \left(6.45 \times 10^{43} \exp\left(-\frac{t}{8.8}\right) + 1.45 \times 10^{43} \exp\left(-\frac{t}{111.3}\right) \right) \quad (4)$$

$$E_{57} = (\alpha M_{Ni})(0.83) \left(\frac{1.45 \times 10^{43}}{6.5} \right) \exp\left(-\frac{t}{392.04}\right) \quad (5)$$

The absolute magnitudes of each of these decay energies was calculated as in eq. 6 and 7, where t_0 is the time for the ejecta to become optically thin to the radiation, 0.034 is the fraction of the energy which manifests as positrons, and λ is a conversion factor which is related to the flux of a 0^{th} absolute magnitude star. At large times, the optical depth parameter approaches 1, resulting in only the 0.034 term remaining in the logarithm, and so as an approximation this term has been neglected in the ^{57}Co absolute magnitude calculation, as it only becomes significant at roughly 900 days past maximum.

$$M_{56} = -2.5 \log_{10} \left(E_{56} \left[1 - \exp\left(-\left(\frac{t_0}{t}\right)^2\right) + 0.034 \right] \right) + \lambda \quad (6)$$

$$M_{57} = -2.5 \log_{10} (E_{57}(0.034)) + \lambda \quad (7)$$

$$\lambda = 2.5 \log_{10} (4\pi(9.52 \times 10^{38})(2.04 \times 10^{-5})) \quad (8)$$

Absolute magnitude contributions can be summed and converted to an apparent magnitude, m_{sum} , in general via equations (9) and (10) below, where d is the distance to the supernova.

$$M_{sum} = -2.5 \log_{10} \left[\sum_{i=0}^n 10^{-\left(\frac{M_i}{2.5}\right)} \right] \quad (9)$$

$$m_{sum} = 5 \log_{10}(d) - 5 + M_{sum} \quad (10)$$

These equations allow for a theoretical light curve to be obtained and compared to the observed light curve. Once the model was fit to the data, relative isotopic densities of the progenitor could be inferred from the value of α .

3 Results

3.1 HST Photometry

Tables 1 and 2 represent the data used in calculating magnitudes from the HST images, and the errors associated with these values. The photometric error was taken as the ratio of the 1σ RMS deviation from mean background value to the supernova value, both in counts per second. The RMS deviation was calculated by taking over 100 samples from the background of each image, fitting this to a Gaussian and comparing the 1σ deviation of this Gaussian to the calculated RMS deviation from mean of the data. Both values consistently agreed to two significant figures and the noise value was taken as the RMS deviation from mean directly calculated from the data. This noise to signal ratio gives an approximate uncertainty in magnitudes for the supernova value in each image and is denoted N/S. The

Table 1. HST magnitude calculation for SN 1992A.

| Filter | Days Past Maximum | 3px Aperture Magnitude | Aperture Correction | STMAG to Johnson | Apparent Magnitude |
|--------|-------------------|------------------------|---------------------|------------------|--------------------|
| F555W | 932 | 25.8983 | -0.1427 | +0.02 | 25.7754 |
| F439W | 932 | 26.2040 | -0.1823 | +0.67 | 26.6917 |
| F555W | 1697 | 26.204 | - | - | 27.3594 |

Note. — For data for 1697 days past maximum, 3px aperture magnitude represents mean background value and apparent magnitude represents this value in counts s^{-1} + background RMSD as in Table 2, converted to an apparent magnitude as there is no clear detection in this image.

Table 2. HST error calculation for SN 1992A

| Filter | Days Past Maximum | Aperture Correction Error (mag) | Background RMSD (counts s^{-1}) | N/S Ratio | Total Error |
|--------|-------------------|---------------------------------|---|-----------|-------------|
| F555W | 932 | 0.0603 | 0.0693 | 0.2098 | 0.218 |
| F439W | 932 | 0.0634 | 0.0195 | 0.3635 | 0.369 |
| F555W | 1697 | - | 0.0654 | - | - |

aperture correction error, Δ_{AC} was taken to be the 1σ RMS deviation from mean of the $\Delta m_{3,6}$ values, calculated in a similar manner. In each case, the total error was calculated as $\sqrt{(\Delta_{AC})^2 + (N/S)^2}$.

3.2 Model fit of SN 1992A

By fitting the model light curve in the V band to the observed data, the best fit occurred at $\alpha = 0.025_{-0.08}^{+0.09}$, ie. a 2.5% relative abundance of ^{57}Co to ^{56}Co , focusing mainly on the

difference between the magnitude of the HST late time data and the light curve (0.007 magnitudes at 2.5%). The maximum associated error to this figure is due to the error of the HST magnitude, ± 0.22 . This is calculated as the the combination of errors from the imaging and aperture correction. Within this range, the difference between the observed value and the model does not exceed 0.22.

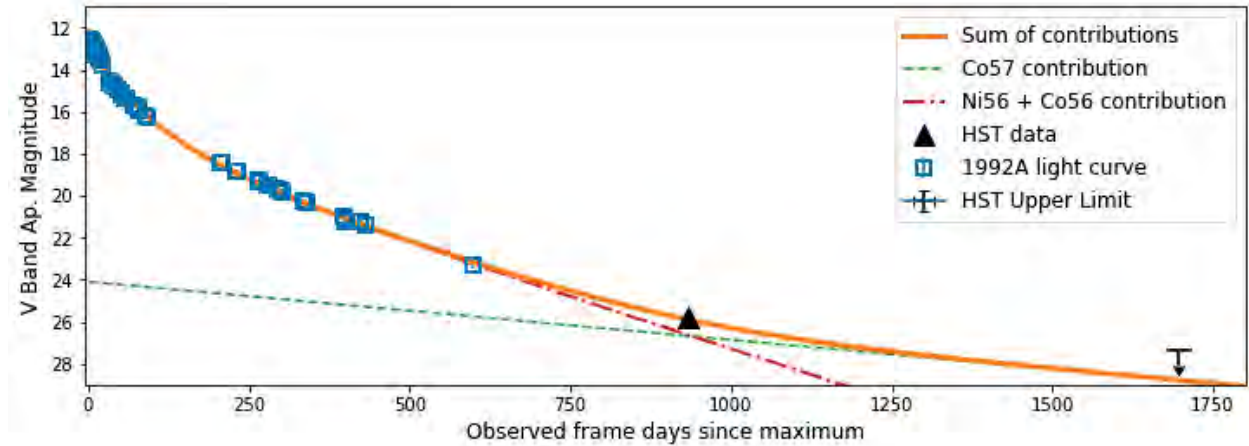
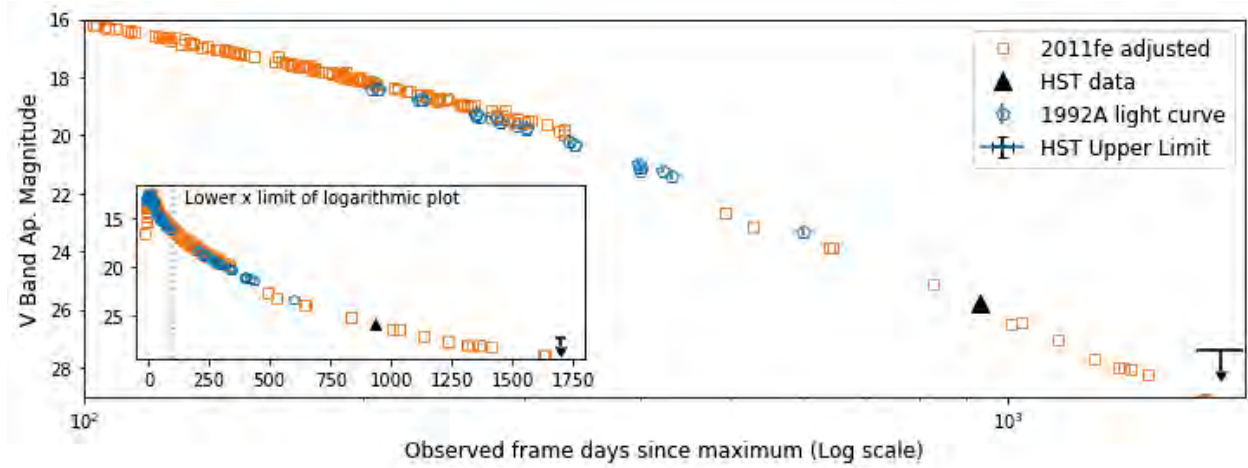


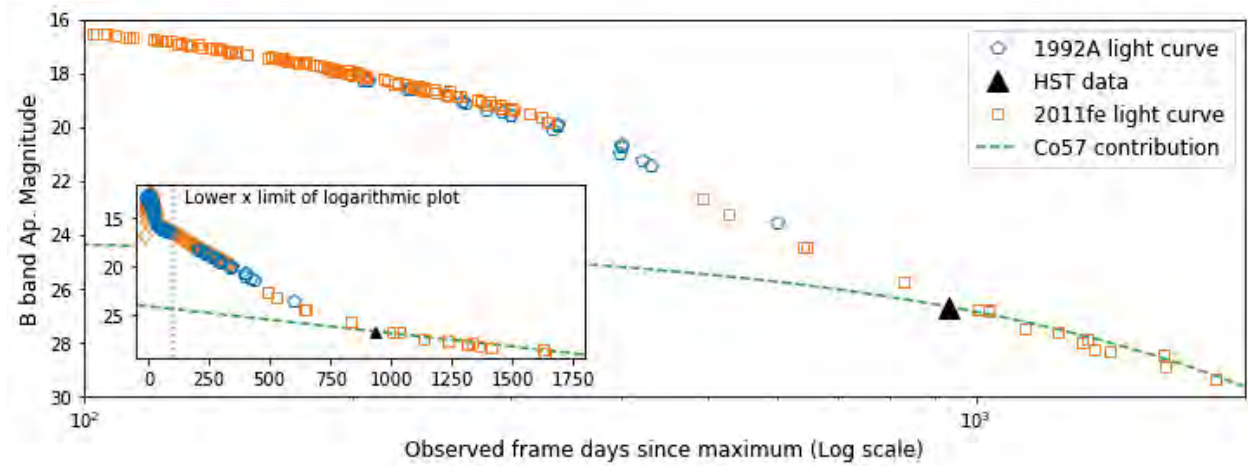
Fig. 1 Light curve model at best fit value of $\alpha = 0.025$. Note that such large timescales and thus, magnitude ranges are being used here and in other figures that error bars are too small to be seen behind individual points.

3.3 Comparison to 2011fe

The analysis of this model fit is based on the analysis of SN 2011fe by Shappee et al. (2017), and thus it is important that the light curves of both supernovae evolve in the same fashion. Figure 2 compares the light curve of SN 1992A to that of SN 2011fe, presented with a logarithmic time axis in the larger plots to emphasise the correlation in the 200 - 600 day portion of the data. The 2011fe data were adjusted to the rest frame of 1992A by scaling their time data by the ratio of their redshifts: $(1.006261/1.000804)$.



(a) V band light curves



(b) B band light curves

Fig. 2 Comparison of light curves of SN 1992A and SN 2011fe, wherein the light curve of 2011fe is adjusted to the rest frame of 1992A, and the light curves are matched at maximum by adding 2.55 magnitudes to all points on the 2011fe curves.

4 Analysis and Conclusions

In the analysis of SN 2011fe, Shappee et al. (2017) find that a ^{57}Co to ^{56}Ni ratio given by $\log_{10}({}^{57}\text{Co}/{}^{56}\text{Ni}) = -1.59_{-0.07}^{+0.06}$, (ie. $0.0257_{-0.033}^{+0.045}$) strongly supports the double degenerate progenitor model as opposed to the SD model, due to the central progenitor density required for such a nucleosynthetic yield. The ratio obtained for SN 1992A using this model of

$\alpha = 0.025_{-0.08}^{+0.09}$ matches this remarkably well, but with larger errors due to less observation data being available for 92A. Even accounting for the full range of relative abundances within the error, this isotopic yield still strongly supports the DD progenitor model. The error in this figure is a combination of errors in aperture correction and in the imaging.

In comparison of the evolution of the light curves of 1992A and 2011fe in both the B and V bands, it is clear that both SNe exhibit the same characteristics, and the latest data available for 1992A (the HST images) fits well with the adjusted 2011fe light curve. The only difference between the curves is a sudden "drop" observed in the 11fe light curve after the 300-400 day gap. This could be due to the fact that the data before and the data after this gap comes from two different sources, and some flux may have been lost in slightly different passbands. However, this feature of the light curve occurs in the early time portion, and thus is not of major significance to the analysis. In the model, t_0 was set to 50 days, however this figure is also insignificant as this optical depth parameter has a large effect at early times, but the late time light curve is largely unaffected.

We follow the analysis of SN 2011fe in Shappee et al. (2017), in which the light curve can only be explained using only ^{56}Ni and ^{57}Co with an upper limit on the ^{55}Fe abundance ratio of $^{55}\text{Fe}/^{57}\text{Co} < 0.22$ at 99% confidence, concluding that the Röpke et al. (2012) DD model ($^{55}\text{Fe}/^{57}\text{Co} = 0.27$) is strongly favored over their SD model ($^{55}\text{Fe}/^{57}\text{Co} = 0.68$).

References

- Shappee, B. J., Stanek, K. Z., Kochanek, C. S., & Garnavich, P. M. 2017, , 841, 48
- Phillips, M. M. 1993, , 413, L105
- Riess, A. G., Filippenko, A. V., Challis, P., et al. 1998, , 116, 1009
- Perlmutter, S., Turner, M. S., & White, M. 1999, Physical Review Letters, 83, 670
- Jeffery, D. J. 1999, arXiv:astro-ph/9907015
- Hayden, B. T., Garnavich, P. M., Kessler, R., et al. 2010, , 712, 350

Calculating Absolute Transition Probabilities for Nuclei in the Rare-Earth Region

Anne Stratman

2017 NSF/REU Program
Physics Department, University of Notre Dame

Advisor: Prof. Ani Aprahamian

Abstract

Absolute transition probabilities are the cornerstone of understanding nuclear structure physics in comparison to nuclear models. I have helped develop code in Python and Mathematica to calculate absolute transition probabilities from measured lifetimes. Both of these methods take pertinent quantities such as the lifetime of a given state, the energy and intensity of the emitted gamma ray, and the multipolarities of the transitions to calculate the appropriate $B(E1)$, $B(E2)$, $B(M1)$ or in general, any $B(\sigma\lambda)$ values. The program allows for the inclusion of mixing ratios of different multipolarities and the electron conversion of gamma-rays to correct for the intensities, and yields results in absolute units or results normalized to Weisskopf units. My contributions to this work include rewriting portions of the code to account for the E2/M1 mixing in mixed E2/M1 transitions; accounting for asymmetric uncertainty in multipole mixing fractions; and adding an optional conversion from absolute units to Weisskopf units. The code has been tested against available data in a wide range of nuclei from the rare earth region (28 in total), including $^{146-154}\text{Sm}$, $^{154-160}\text{Gd}$, $^{158-164}\text{Dy}$, $^{162-170}\text{Er}$, $^{168-176}\text{Yb}$, and $^{174-182}\text{Hf}$. Both versions will be available from the Notre Dame Nuclear Science Laboratory webpage for use by the community.

Introduction

For a group of radioactive nuclei, the rate at which the sample decays is proportional to a decay constant, also known as the transition probability. This constant can be

expressed in terms of the mean lifetime or the half-life of a sample:

$$\mathcal{W} = \frac{1}{\tau} = \frac{T_{1/2}}{-\ln(0.5)} \quad (1)$$

where τ is the mean lifetime, and $T_{1/2}$ is the half-life.

One possible mode of decay for an excited nucleus is γ -decay, in which a nucleus decays from an excited state to a lower energy state through the emission of a photon. γ -decays are labelled using $\sigma\lambda$ notation, where σ describes the electromagnetic character of the photon, and λ describes the multipole character of the radiation field produced by the γ -ray (i.e. the angular distribution of the radiation, the parity of the radiation field, and the radiated power).¹ In this notation, σ is either “E” or “M” to denote whether the γ -ray originated from electric or magnetic interactions with an external magnetic field, respectively; and λ is a positive integer (i.e. 1 for dipole, 2 for quadrupole, 3 for octupole, etc.).

An excited nucleus may have multiple γ -decay channels (it can decay from an initial state to multiple final states). For a nucleus with multiple γ -decay channels, the transition probability is given by the sum of all transition probabilities weighted by the branching ratio (BR_i) and the internal conversion coefficient (α_i) of each transition:

$$\mathcal{W} = \sum_i \mathcal{W}(i) = \sum_i \frac{BR_i}{\tau(1 + \alpha_i)} \quad (2)$$

where the branching ratio gives the relative intensity of a particular decay compared

¹K.S. Krane. (1988). *Introductory Nuclear Physics*, John Wiley & Sons, Inc., pp. 328-331.

to all other channels exiting a level, and the internal conversion coefficient accounts for the possibility of an atomic electron being ejected in place of a γ -ray being emitted from the nucleus.

Transition probabilities are proportional to the square of the nuclear matrix element that describes how a nucleus interacts with an external magnetic field in transitioning from an initial state $|\psi_i\rangle$ to a final state $|\psi_f\rangle$. As such, the transition probability for a certain γ -decay can be used to calculate the nuclear matrix element for that transition, and hence to understand how two states $|\psi_i\rangle$ and $|\psi_f\rangle$ are connected. The following equation is used to calculate absolute² transition probabilities:

$$B(\sigma\lambda; J_i \rightarrow J_f) = \frac{\hbar}{8\pi} \mathcal{F}(\sigma\lambda) \frac{BR}{\tau(1+\alpha)} \frac{\lambda[(2\lambda+1)!!]^2}{(\lambda+1)} \left(\frac{\hbar c}{E_\gamma}\right)^{2\lambda+1} \quad (3)$$

In Equation (3), the branching ratio BR , the lifetime τ , the internal conversion coefficient α , the energy of the γ -ray E_γ , and the multipolarity of the radiation are all experimentally determined quantities. $\mathcal{F}(\sigma\lambda)$ is the multipole mixing fraction, which measures the mixing between differing multipolarity γ radiation. For pure transitions, this factor collapses to unity. For mixed E2/M1 transitions it follows

²Absolute transition probabilities are calculated when the lifetime of a nuclear state is known, in contrast to reduced transition probabilities, which are calculated when the lifetime of a state is unknown. Reduced transition probabilities predict the likelihood that an initial state will decay to a certain final state, relative to other decays from the same initial state to different final states. Absolute transition probabilities extend this to calculate the probability of a decay from a certain initial state to a certain final state, relative to all other decays within that nucleus.

equations (4) and (5):

$$\mathcal{F}(E2) = \frac{\delta^2}{1 + \delta^2} \quad (4)$$

$$\mathcal{F}(M1) = \frac{1}{1 + \delta^2} \quad (5)$$

Equations (4) and (5) are used to calculate the probability of an E2 or M1 transition occurring, respectively. The multipole mixing fraction δ is defined as a ratio of the E2/M1 transition strengths.

Transition probabilities are dimensioned quantities, with units given by:

$$B(E\lambda) : e^2 \text{fm}^{2\lambda} \quad (6)$$

$$B(M\lambda) : \mu_N^2 \text{fm}^{2\lambda-2} \quad (7)$$

These units are known as absolute units. Another set of units, Weisskopf units (W.u.), is also commonly used to compare transition rates. They are derived from Weisskopf estimates - estimates of the transition rates between $|\psi_i\rangle$ and $|\psi_f\rangle$ that assume that the transition is due to a single proton that changes from one shell-model state to another. The following equations are used to calculate Weisskopf estimates:

$$B_W(E\lambda) = \frac{1}{4\pi} \left(\frac{3}{\lambda + 3} \right)^2 (0.12)^{2\lambda} A^{2\lambda/3} e^2 \text{fm}^{2\lambda} \quad (8)$$

$$B_W(M\lambda) = \frac{10}{\pi} \left(\frac{3}{\lambda + 3} \right)^2 (0.12)^{2\lambda-2} A^{(2\lambda-2)/3} \mu_N^2 \text{fm}^{2\lambda-2} \quad (9)$$

Dividing an experimental transition probability by the Weisskopf estimate, and mul-

tiplying by a proportionality constant³, yields transition probabilities in terms of W.u.

Process

We have developed two programs, one written in Mathematica and the other in Python, to calculate transition probabilities for nuclei that γ -decay. To use either program, all that is required is the appropriate coding software, and software capable of generating a csv file (e.g. Excel or LibreOffice). Both programs read input from a csv file to calculate $B(\sigma\lambda)$ values. Table 1 shows the necessary input parameters:

| <i>line 1</i> | E_γ | δE_γ | I_γ | δI_γ | $I_{\gamma,tot}$ | δ_{mix} | $\delta_{\delta_{mix}}^+$ | $\delta_{\delta_{mix}}^-$ | τ | δ_τ^+ | δ_τ^- | α_K | δ_{α_K} | A | $\sigma\lambda$ | E_{lev} |
|---------------|--------------|-------------------|--------------|-------------------|------------------|----------------|---------------------------|---------------------------|--------------|-----------------|-----------------|--------------|---------------------|--------------|-----------------|--------------|
| 2 | 0.888157 | 0.005 | 174.8 | 3.9 | 369.3 | 0 | 0 | 0 | 2830 | 110 | 110 | 0.0032 | 0 | 162 | E2 | 888.158 |
| \vdots | \downarrow | \downarrow | \downarrow | \downarrow | \downarrow | \downarrow | \downarrow | \downarrow | \downarrow | \downarrow | \downarrow | \downarrow | \downarrow | \downarrow | \downarrow | \downarrow |

Table 1: Required format for an input file

In the above table, E_γ is the energy of an emitted γ -ray (in MeV); I_γ is the intensity of a γ -ray (in arbitrary units); $I_{\gamma,tot}$ is the sum of the intensities of *all* γ -rays exiting the level; δ_{mix} is the multipole mixing fraction for a γ -ray (set to 0 if no mixing occurs); τ is the mean lifetime of the level (in fs); α_K is the internal conversion coefficient; A is the atomic number of the nucleus; $\sigma\lambda$ is the multipolarity of the transition; and E_{lev} is the level energy of the initial state (in keV). δE_γ , δI_γ , $\delta_{\delta_{mix}}^+$, $\delta_{\delta_{mix}}^-$, δ_τ^+ , δ_τ^- , and δ_{α_K} are the uncertainties in their respective quantities.⁴

³This constant is $k\alpha\hbar c/(100\text{fm}^2)^2$, where $k = \lambda[(2\lambda + 1)!!]^2/(\lambda + 1)$ and $\alpha = e^2/4\pi\epsilon_0\hbar c$

⁴ $\delta_{\delta_{mix}}^+$ and $\delta_{\delta_{mix}}^-$, and δ_τ^+ and δ_τ^- , are upper and lower uncertainties, respectively.

Both the Mathematica notebook and Python script initially take user input to specify the location of the data file, the names of the output files, and the units to be used (absolute units or W.u.). The Python script also takes user input to determine how many decimal places to report in the calculated $B(\sigma\lambda)$ values. After reading in the input from the csv file, the two programs use this input to execute transition probability calculations. The two programs are structured similarly, and contain sections for calculating transition probabilities in absolute units, for converting from absolute units to W.u., and for error propagation. The Mathematica notebook outputs pdf files (one each for transitions of each individual multipolarity and one containing all transitions) while the Python script outputs a text file, formatted in LaTeX syntax. Table 2 and Figure 2 in the Appendix contain sample output tables for the two programs.

This code was tested using available data from a range of rare-earth nuclei: $^{146-154}\text{Sm}$, $^{154-160}\text{Gd}$, $^{158-164}\text{Dy}$, $^{162-170}\text{Er}$, $^{168-176}\text{Yb}$, and $^{174-182}\text{Hf}$.⁵ Output from the $^{156-160}\text{Gd}$ calculations was tested against previously published $B(\sigma\lambda)$ values. Transition probabilities for the rest of the isotopes were calculated to ensure that the code yielded reasonable values for a variety of input data. The calculated transition probabilities were then used to produce schematics for selected rare-earth nuclides, as shown in Figure 1. These schematics will be used to draw conclusions about the characteristics of 0_n^+ vibrational bands and the collectivity of γ -decays in even-even rare-earth nuclei.

⁵Data for ^{156}Gd from paper by J. Klora et al. Data for ^{158}Gd and ^{160}Gd from papers by S.R. Leshner et al. Data for ^{162}Dy from paper by A. Aprahamian et al. All other data was retrieved from the NNDC website.

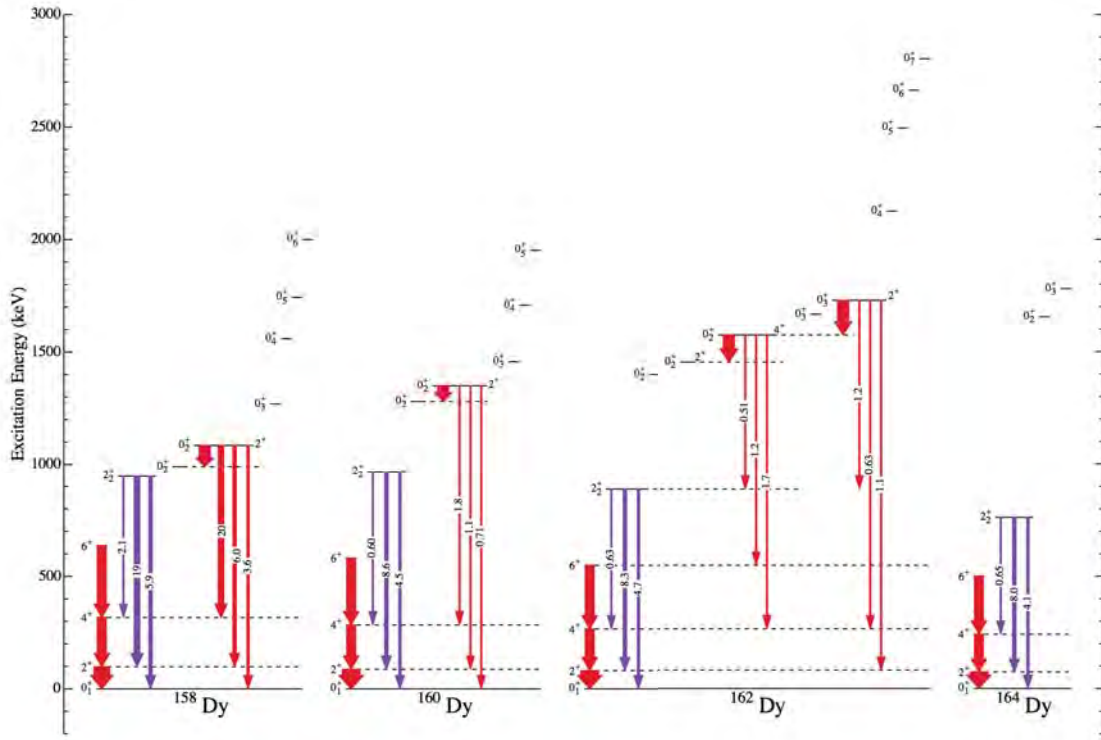


Figure 1: Schematics for $^{158-164}\text{Dy}$

Conclusion

The Mathematica notebook and Python script developed through this project are powerful tools for calculating absolute transition probabilities. The code requires minimal user input, can yield output in two sets of units, and accounts for multipole mixing. In addition, both versions are accessible and easy to use. Future work on this project will include writing an article, to be published in *Nuclear Instruments & Methods*, about this code; and publishing the programs on the University of Notre Dame's webpage for public domain use.

Acknowledgements

First and foremost, I would like to thank my advisor, Prof. Ani Aprahamian, for her guidance in completing this project. I would also like to thank Dr. Clark Casarella, who began the coding project and coded the vast majority of the finished script; and the other members of Prof. Aprahamian's research group.

This work was funded by the University of Notre Dame College of Science Summer Undergraduate Research Funding (COS-SURF), and by the National Science Foundation under grant PHY-1419765.

Appendix

| E_{lev} (keV) | E_γ (keV) | L_γ | τ (fs) | $\pi\ell$ | δ | $B(\pi\ell)$ (cgs) |
|-----------------|------------------|------------|---------------------|-----------|----------------------|--|
| 1049.48 | 960.51 (20) | 138.0 (0) | $1810_{0.0}^{+0.0}$ | E2 | 0.0 $_{-0.0}^{+0.0}$ | $0.055016_{-0.055165}^{+0.049288}$ e ² b ² |
| 1049.48 | 960.51 (20) | 138.0 (0) | $4750_{0.0}^{+0.0}$ | E2 | 0.0 $_{-0.0}^{+0.0}$ | $0.020964_{-0.021021}^{+0.018781}$ e ² b ² |
| 1129.44 | 1112.94 (20) | 80.0 (0) | $1260_{0.0}^{+0.0}$ | E2 | 0.0 $_{-0.0}^{+0.0}$ | $0.006144_{-0.006156}^{+0.005592}$ e ² b ² |
| 1129.44 | 1112.94 (20) | 80.0 (0) | $2590_{0.0}^{+0.0}$ | E2 | 0.0 $_{-0.0}^{+0.0}$ | $0.002989_{-0.002995}^{+0.00272}$ e ² b ² |
| 1129.44 | 1040.47 (20) | 294.0 (0) | $1260_{0.0}^{+0.0}$ | E2 | 0.0 $_{-0.0}^{+0.0}$ | $0.031334_{-0.031407}^{+0.028323}$ e ² b ² |
| 1129.44 | 1040.47 (20) | 294.0 (0) | $2590_{0.0}^{+0.0}$ | E2 | 0.0 $_{-0.0}^{+0.0}$ | $0.015244_{-0.015279}^{+0.013779}$ e ² b ² |
| 1129.44 | 841.24 (20) | 119.0 (0) | $1260_{0.0}^{+0.0}$ | E2 | 0.0 $_{-0.0}^{+0.0}$ | $0.036994_{-0.037125}^{+0.032597}$ e ² b ² |
| 1129.44 | 841.24 (20) | 119.0 (0) | $2590_{0.0}^{+0.0}$ | E2 | 0.0 $_{-0.0}^{+0.0}$ | $0.017997_{-0.018061}^{+0.015858}$ e ² b ² |

Table 2: Sample Python output for ¹⁵⁶Gd transitions, calculated in absolute units. The LaTeX-friendly tables generated by the Python script can easily be copied and pasted into other documents.

| Elev (keV) | E γ (keV) | τ (fs) | πl | B(E1) pure (mW.u.) | σ B(E1) pure (mW.u.) | σ B(E1) pure (mW.u.) |
|------------|------------------|-------------|---------|--------------------|-----------------------------|-----------------------------|
| 888.158 | 888.157 | 2830. | E2 | - | - | - |
| 888.158 | 807.501 | 2830. | E2 | - | - | - |
| 888.158 | 622.494 | 2830. | E2 | - | - | - |
| 1148.23 | 260.067 | 300 000. | E1 | 0.0504847 | 0.000789745 | -0.000789745 |
| 1148.23 | 185.292 | 300 000. | E1 | 0.029498 | 0.00121694 | -0.00121694 |
| 1275.77 | 1275.81 | 29. | E1 | 2.30548 | 0.402131 | -0.402131 |
| 1275.77 | 1195.09 | 29. | E1 | 3.82255 | 0.722553 | -0.722553 |
| 1357.92 | 1277.27 | 214. | E1 | 0.42655 | 0.00796066 | -0.00796066 |
| 1357.92 | 1092.26 | 214. | E1 | 0.494245 | 0.0318184 | -0.0318184 |
| 1485.67 | 1219.98 | 2910. | E1 | 0.0401726 | 0.00120821 | -0.00120821 |
| 1485.67 | 937.144 | 2910. | E1 | 0.0399622 | 0.00266415 | -0.00266415 |
| 1485.67 | 424.676 | 2910. | E1 | 0.0171984 | 0.00107492 | -0.00107492 |
| 1485.67 | 302.909 | 2910. | E1 | 0.0375205 | 0.000987555 | -0.000987555 |
| 1485.67 | 275.582 | 2910. | E1 | 0.0998938 | 0.00493333 | -0.00493333 |

Figure 2: Sample Mathematica output for ^{162}Dy transitions, calculated in mW.u.

References

- [1] S.S. Wong. (1990). *Introductory Nuclear Physics*. Prentice-Hall, Inc.
- [2] K.S. Krane. (1988). *Introductory Nuclear Physics*. John Wiley & Sons, Inc.
- [3] J. Klorá, H.G. Börner, T. von Egidy, R. Georgii, J. Jolie, S. Judge, V.A. Khitrov, B. Krusche, V.A. Libman, H. Lindner, L.L. Litvinsky, U. Mayerhofer, A.V. Murzin, S.J. Robinson, A.M. Subkhovoj, and H. Tiedt, Nucl. Phys. A **561**, 1-73 (1993).
- [4] S.R. Leshar, J.N. Orce, Z. Ammar, C.D. Hannant, M. Merrick, N. Warr, T.B. Brown, N. Boukharouba, C. Fransen, M. Scheck, M.T. McEllistrem, and S.W. Yates, Phys. Rev. C **76**, 034318 (2007).
- [5] S.R. Leshar, C. Casarella, A. Aprahamian, B.P. Crider, R. Ikeyama, I.R. Marsh, M.T. McEllistrem, E.E. Peters, F.M. Prados-Estévez, M.K. Smith, Z.R. Tully, J.R. Vanhoy, and S.W. Yates, Phys. Rev. C **91**, 054317 (2015).
- [6] A. Aprahamian, S.R. Leshar, C. Casarella, H.G. Börner, and M. Jentschel, Phys. Rev. C **95**, 024329 (2017).
- [7] NNDC database, www.nndc.bnl.gov

A Chemical Perspective of Stars in Dwarf Galaxies & Converting Coordinates

Di Tian

2017 NSF/REU Program

Physics Department, University of Notre Dame

ADVISORS: Prof. Beers, Postdoc. Yoon, Graduate Student: Sarah

Abstract:

Basically what I did in this summer consists of two parts: chemical analysis and kinematic calculations. The first one is to take a look at the carbon abundances($A(C)$) as well as $[C/Fe]$ of the stars in classical dwarfs and ultra-faint dwarfs(UFDs). The reason why I did this will be stated later. I also explored the morphology of the abundance distribution of other elements like Na, Ba, Si, etc. And I made a comparison between chemical features of stars in classical dwarfs and ultra-faint dwarfs. The second part of my entire research is to the velocities of the MILKYWAY stars relative to the galactic center.

1.The Yoon-Beers Diagram

My project starts from a figure in the paper written by Yoon & Beers (2016).

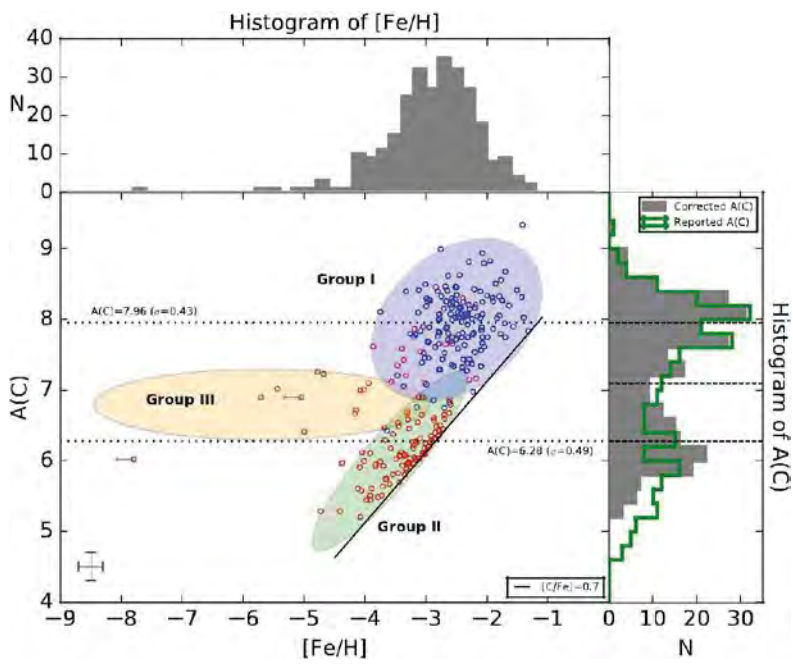


Figure 1

The figure 1 above is called Yoon-Beers Diagram. It shows the $A(C)$ (absolute carbon abundances) distribution versus metallicity ($[Fe/H]$) for the sample of sub-classified CEMP (CEMP -s/rs and CEMP -no) stars. The blue and red open circles represent the CEMP -s/rs and CEMP -no stars.

There are stark differences in the morphology of $A(C)$ vs. $[Fe/H]$ distributions between the CEMP -s/rs and CEMP -no stars. The distribution of $A(C)$ for the former gathers in relatively high-C region, and it exhibits a very weak dependence on $[Fe/H]$. This subset of stars in the diagram is called “Group I”. However, the CEMP -no stars exhibit two very different behaviors in the diagram. We refer to these as “Group II” and “Group III” stars. The Group III stars are located on the lowest metallicity regime, centered on $A(C) \sim 6.8$. The $A(C)$ values for the Group III stars exhibit no clear dependence on $[Fe/H]$. In contrast, CEMP -no stars are located in higher metallicity region, and they exhibit a clear dependence of $A(C)$ on $[Fe/H]$. All these differences in the two group of CEMP -no stars led an argument that there are more than one class of progenitors for the CEMP -no stars. According to some theories, there are two models may be able to explain the origins of CEMP -no stars: mixing and fallback models as well as rotating massive star models. Further investigation still needs to be done.

The samples compiled in the Yoon-Beers Diagram are basically stars in the MILKYWAY. To find more clues to support the idea that CEMP -no stars have two

kinds of progenitors, we need to look at more stars, which became an important job for me to do. I downloaded the data of dwarf galaxy stars from the SAGA Database, arranged them, and did some computer programming using Python to plot the $A(C)$ versus $[Fe/H]$ distribution figure just in the style like the Yoon-Beers Diagram. Based on that, I also plotted the element abundance distribution for Na, Si and Ba to make a comparison between the classical dwarfs and ultra-faint dwarfs.

To be more specific, the scientific goals for me are:

1. Explore the behaviors shown in Yoon-Beers Diagram exist in the stars from satellite galaxies (both Classical Dwarfs and UFDs)
2. Expect the Group II and III stars present in UFD galaxies
3. Compare the distribution of carbon abundances versus metallicity of stars in Classical Dwarfs and UFDs.
4. Examine whether contrasts in the observed abundances for other elements might exist

2. Stars in Dwarf Galaxies

As I've mentioned, we refer to the dwarf satellites as two groups, classical dwarfs and ultra-faint dwarfs. Basically, they are all small galaxies and composed of about 100 million up to several billion stars. A large fraction of their mass comprises dark matter. Besides, there are also some differences. Basically, ultra-faint

dwarfs have average metallicities of $[Fe/H] \sim -2.5$ with underlying $[Fe/H]$ spreads of up to ~ 2.5 dex, lower than classical dwarfs. They also are much fainter, smaller than classical dwarfs. Their star populations are dominated by truly ancient stars. These systems lack stars with $[Fe/H] > -1.0$, and they're believed to be the living relics of the first star-forming mini-haloes. What's more, they can help us with the study of early star-forming environments and associated conditions.

Figure 2 and figure 3 are the $A(C)$, $[C/Fe]$ distribution as functions of $[Fe/H]$ for the sample of stars from classical dwarfs and ultra-faint dwarfs. Stars from different galaxies have different corresponding colors or markers. The markers for the stars that are not CEMP stars are rightward triangles. The three gray solid lines provides the references at $[C/Fe] = 0.5, 0.7, 1.0$. The right box in each diagram contains the galaxies included together with their masses.

From figure 2, the ultra-faint dwarfs lack stars with $[Fe/H] > -1.5$. It's not hard to explain. As ultra-faint dwarfs galaxies have quite low mass, they have not enough gas to form new stars, and most stars have nearly stopped evolving, which means the creation of iron and other heavy elements has stopped. Apart from that, there's an inspiring message we can get from figure 2. The morphology of CEMP stars in figure 2 clear shows the behaviors like Group 2 and Group 3 stars. Another important thing is that most CEMP stars in ultra-faint dwarf galaxies are CEMP -no stars. It can be proved by later illustration with Ba abundance diagram. In addition, the Yoon-Beers

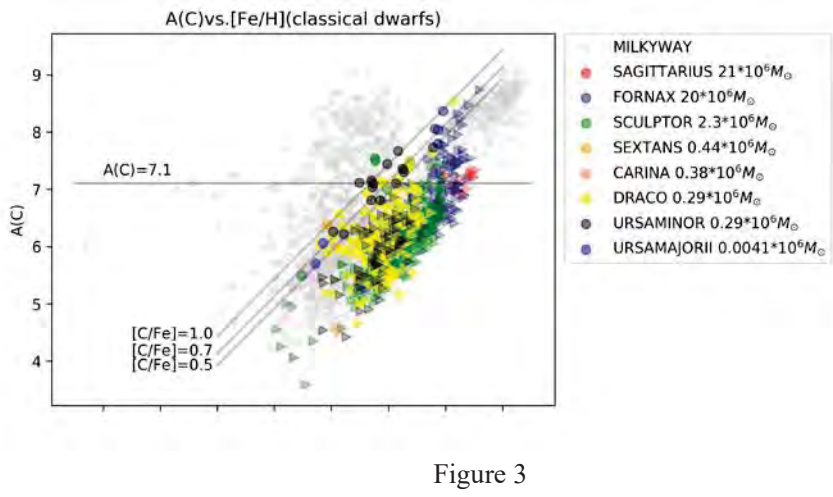
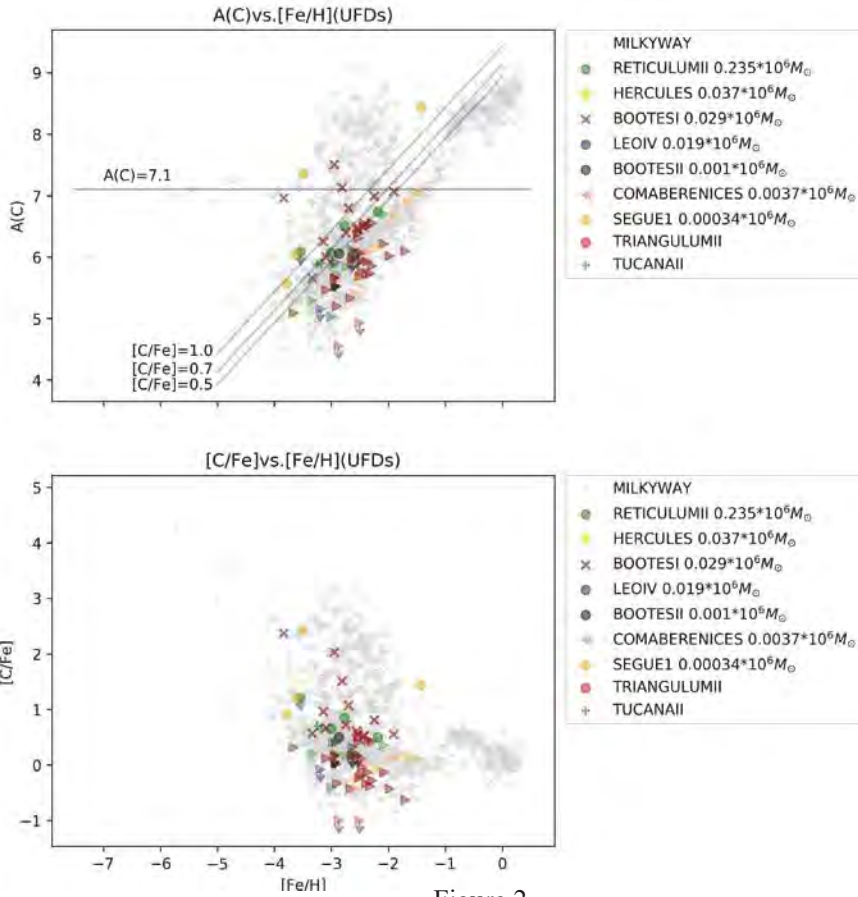


Diagram reflects a well division of stars by the fiducial line at $A(C)=7.1$. It effectively separates the binary nature of all of the CEMP -s/rs stars and most of the CEMP -no stars. So we can simply identify a CEMP -no star by looking at its absolute carbon abundances, which can also prove that most CEMP stars in figure 2 are CEMP -no stars. However, there maybe exists a problem with the possible Group III stars in figure 2 which needs further investigation. If making a more precise comparison with the Yoon-Beers Diagram, although the morphology looks alike, the values of metallicity of the “Group 3 stars” in figure 2 are all lower than -4. If we match up the region of these 4 “Group 3 stars” with that of Yoon-Beers Diagram, we’ll realize that most part of this region actually belongs to Group I. Only one of the BOOTESI star in the left middle of the picture with can be definitely identified as a Group III star.

For figure 3, it’s easy to recognize stars from Group 2 and Group 3. By checking the neutron-capture element abundances of the Group 2 stars in figure 3, only few of them are CEMP -no stars. It’s not hard to understand. CEMP -no stars are believed to be accreted form the first galaxies due to their large lack of metallicity, while ultra-faint dwarf galaxies are thought to be the relics of the first galaxies. They should have more CEMP -no stars.

That’s the basic analysis of the morphology about carbon. Then I moved on to other elements.

Figure 4, figure 5 are about silicon, one of the α -elements. The plots are made just in

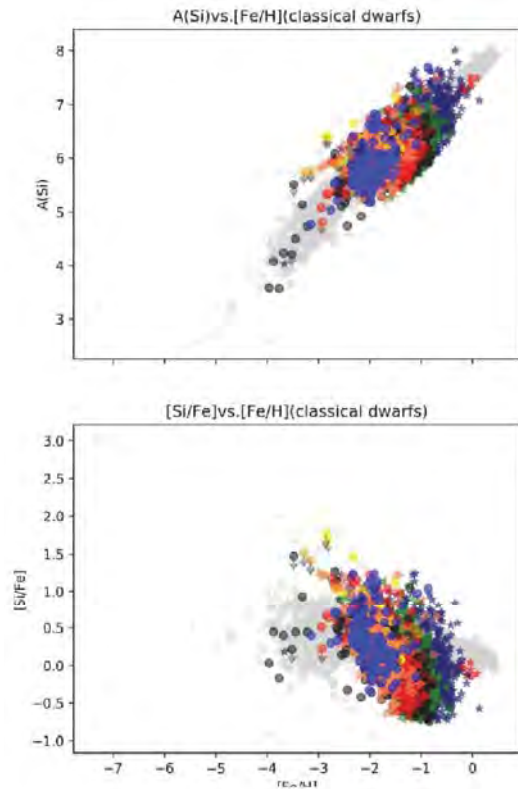


Figure 4

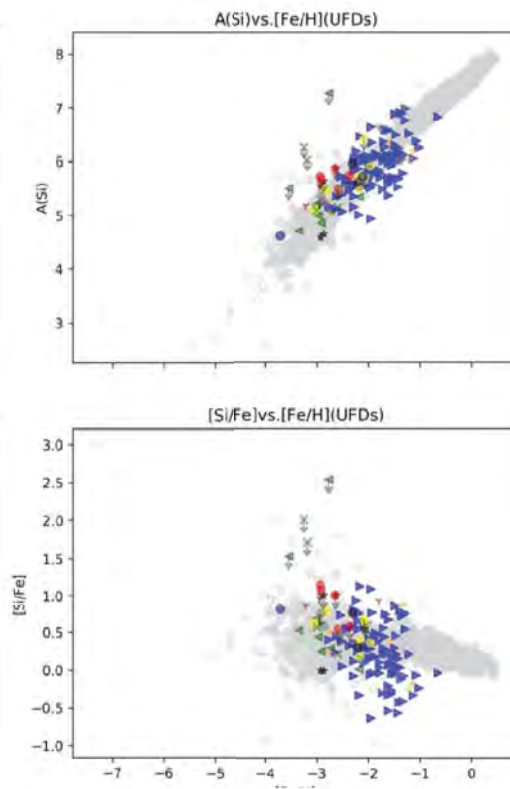


Figure 5

the same style as the previous ones. I was expecting a downturn in [Si/Fe] at higher metallicity in the case of classical dwarfs because of the affection from Type Ia supernovae. Type Ia supernovae is special. It produces iron and little silicon, which can cause the rise of [Si/Fe]. From the diagram, there is a downturn in figure 4.

However, I didn't expect that feature also happened figure 5 because we believe that no additional long-lived stars would have formed after the Type Ia explosions.

Noticing that the downturn happens in figure 5 almost from the same galaxy, CANESVENATICI, maybe it's just a special case. We need further studies. Figure 6, figure 7 are about one of the neutron-capture elements, Ba.

It's apparent that for most stars in ultra-faint dwarf galaxies, the value of A(Ba)

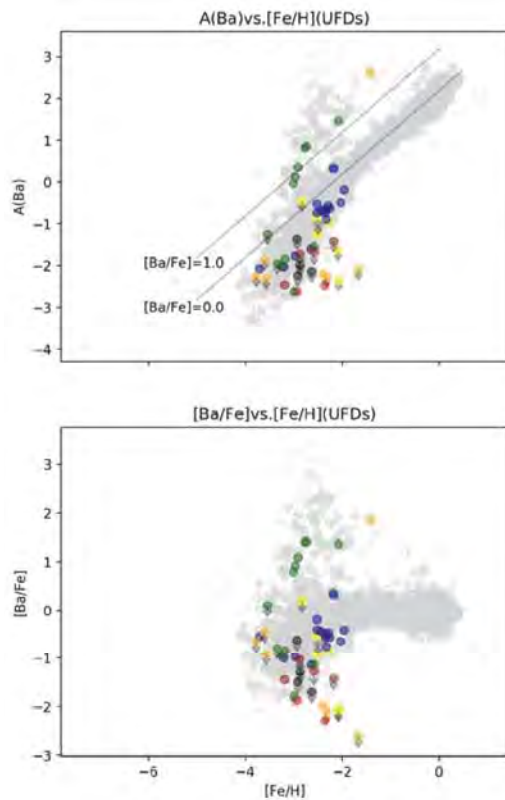


Figure 6

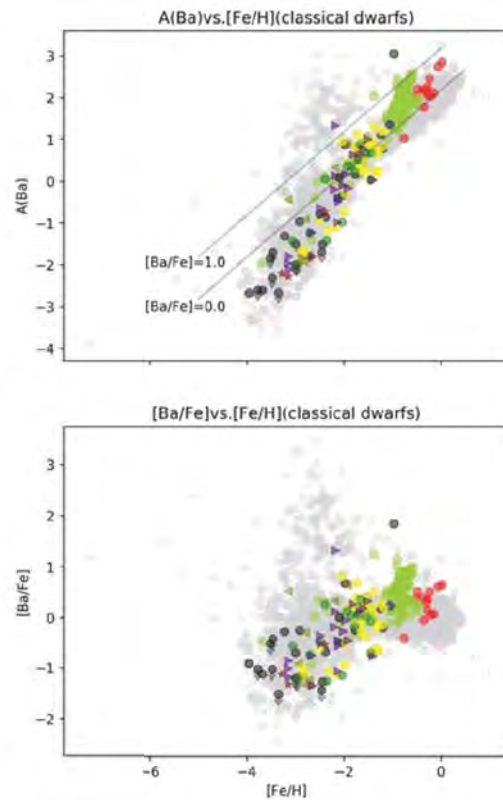


Figure 7

and $[Ba/Fe]$ are low. The neutron-capture process is likely to occur in a restricted progenitor mass range (8 to 10 solar mass). As we believe the first stars are quite massive, neutron-capture process would have barely enriched the Ba abundance in ultra-faint dwarfs. However, in low $[Fe/H]$ region, this is also the case in figure 7.

I haven't found an appropriate explanation so far.

3. Kinematic Calculates

Considering the limitation of space, I won't talk too much about this part. Basically, what I did is to convert coordinates from equatorial system to galactic system, and use Python to calculate the velocities relative to the galactic center.

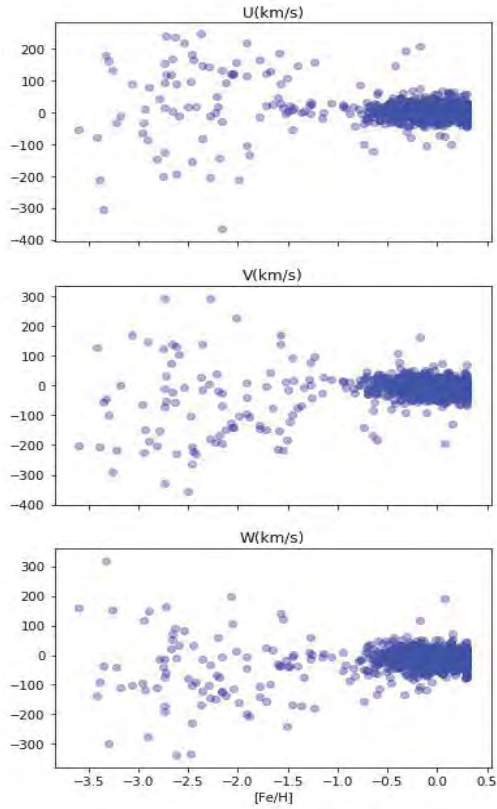


Figure 8

The left figure is one of the plots I made about the velocity distribution in three directions of stars in the MILKYWAY. There's a trend that the dispersion of the velocity becomes small as the metallicity grows. It is because the stars with lower $[Fe/H]$ are from the outer halo. They have larger orbits and they move faster.

4.References

Annu.Rev.Astron.Astrophysics.2015.53:631-88

Jinmi Yoon, The Astrophysics Journal,833:20, 2016 December 10

AMS Radiocarbon Dating Wooden Artwork from the Snite
Museum of Art

Laura Troyer

2017 NSF/REU Program

Physics Department, Notre Dame

ADVISOR:

Dr. Philippe Collon

COLLABORATORS:

Connor Bagwell

Tyler Anderson

Adam Clark

Austin Nelson

Michael Skulski

Abstract

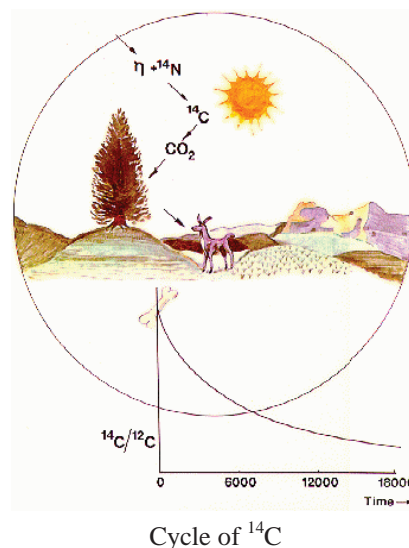
The Snite Museum of Art desires to accurately display authentic artwork and, in doing so, guarantee this authenticity to its patrons. This involves testing their pieces for forgery, which can include testing the artwork material date and cross-referencing that with background information about the piece. To determine the age of the artwork, the accelerator mass spectrometry (AMS) group at the University of Notre Dame will use AMS radiocarbon dating. Primarily, this is to verify whether or not the wood of the artwork is from the bomb-peak era. The first testing of the samples was inconclusive and will be performed again to obtain better sampling statistics in the hopes of narrowing the reported date ranges.

Introduction

The Snite Museum of Art recently acquired a donation of African artwork, some of which lack sufficient evidence to rule them out as potential forgeries. More information surrounding the origins of the pieces in question, specifically the age of five wooden carvings, is needed to determine if the artwork is a forgery. These pieces include a Dogon ritual ladder (museum sample #1), a Duala model canoe (museum sample #2), two Kota reliquaries (museum samples #3 and #4), and a Zulu Knobkerrie (museum sample #5). The AMS group at the University of Notre Dame was tasked with measuring the age ranges of the artwork via radiocarbon dating using accelerator mass spectrometry (AMS). Following is an introduction to radiocarbon dating and AMS.

Radiocarbon dating is a technique used to determine the age of organic materials by comparing the ratio of unstable ^{14}C and stable ^{12}C isotopes¹. A simplified version of the ^{14}C cycle is pictured on the following page.² ^{14}C produced in the stratosphere chemically reacts with oxygen to form CO_2 and disperses throughout the atmosphere³. CO_2 (with most of the

molecules containing ^{12}C) enters into plant material during photosynthesis. Animals ingest CO_2 from plants or other animals and inhale and exhale CO_2 while breathing. While alive, the level of ^{14}C in the plant or animal reflects the ^{14}C level of the atmosphere. When the organism dies, it no longer acquires ^{14}C . This is when the decay count begins. The amount of time that has passed since death can be determined by measuring how much of the ^{14}C is left and comparing that to the



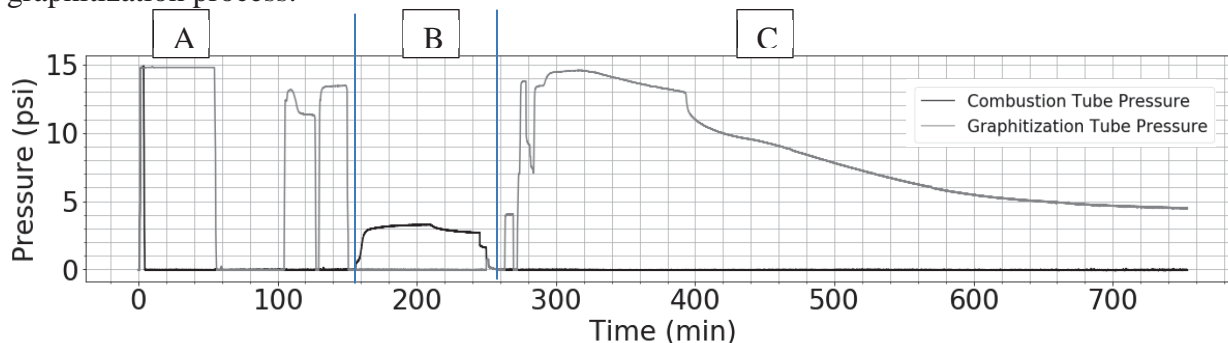
^{12}C amount. The $^{14}\text{C}/^{12}\text{C}$ levels over thousands of years have been well tested using tree rings.³ After 10 half-lives, the unstable isotope concentration between half-lives makes it difficult to differentiate between half-life cycles. Since the half-life of ^{14}C is $5,700 \pm 30$ years⁴, organic materials up to 50,000 years old are measurable. There are several techniques available to measure the carbon isotope ratio.

AMS is one way to measure the isotopic ratios⁵. AMS is a technique that utilizes aspects of nuclear physics and mass spectrometry to form the highly sensitivity measurement capabilities required to find rare isotopes such as ^{14}C . For every one ^{14}C atom, there is approximately 10^{12} stable ^{12}C atoms³. AMS is ideal for long-lived radioactive isotopes because it uses small amounts of sample in a short amount of time and sorts out contamination from isobars (neighboring nuclides of the same mass but different proton number).

Experimental Methods

The carbon in a sample must be extracted and put into a form that can be put through the detector in order to measure the $^{14}\text{C}/^{12}\text{C}$ ratio. Carbon is extracted from the African artwork via burning wood shavings from the inner part of the artwork gotten by drilling a narrow, shallow

hole into the piece. This burning releases the carbon in the form of CO₂. Contaminants from combustion are removed from the CO₂ through several purification steps. Then the CO₂ is reduced to graphite in a two-step reduction process involving H₂. The result is graphite embedded in an iron matrix which will then be packed into a sample holder, or cathode. The cathode is placed into the beginning of the accelerator line in the ion source. The sample, which is mostly carbon and iron, but also has traces of other elements, is accelerated. Contaminants other than ¹⁴C are directed away from the sensitive parallel grid avalanche counter (PGAC) position detector by a series of electric and magnetic elements acting as filters. The ¹⁴C and ¹²C events are counted on separate parts of the machine. More details about this process, starting with graphitization, follow. Please refer to the pressure vs. time graph of a standard graphitization process.



A: Iron Pretreatment. As mentioned above, the graphite will be embedded into an iron matrix during graphitization. In order to prevent contamination of the sample from the iron, the iron must first be pretreated to remove other elements through a series of four baking steps. The iron, 2.0-2.5 mg, in the graphitization tube (gray) is open to atmosphere (pressure of 14.7 psi) and baked at 900°C for 30 minutes to oxidize the iron powder. The oven did not start at time zero on the above graph which includes attaching tubes of new sample material to the line.

After the first baking, the iron is closed off from atmosphere, and the graphitization tube is pumped down to a pressure <10 microns. This is seen at approximately 60 minutes into the

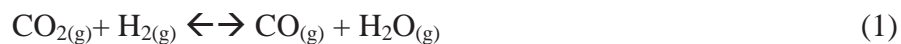
run. Pumping out the gas takes several minutes. The iron is then baked at 815°C for 30 minutes while being pumped on. Next, 12.3 psi of H₂ is introduced to the graphitization tube, and the hydrogen and iron is baked for the third time at 815°C for 15 minutes with liquid nitrogen (LN₂) on the cold finger to freeze out water produced when reacting the hydrogen with the oxygen in the iron. After baking, the system is pumped out; and 12 psi of fresh H₂ is added to the graphitization tube with the LN₂ still on the cold finger. The iron is baked for the last time in the iron pretreatment at 815°C for 15 minutes to remove any lingering oxygen. The system is once again pumped out and the LN₂ is removed. Before pretreatment the iron is a dull gray. After pretreatment the iron is slightly shiny.

B: Combustions/Transfer. During combustion the CO₂ is released from the sample and then transferred from the combustion tube to the graphitization tube. To begin with, 3.2-3.7 mg of wood and 450.0-480.0 mg of copper oxide are put into a crystalline tube and attached to the graphitization line at the same time the iron in the graphitization tube is attached to the line which is during the first ten minutes of the run displayed above. After the tube is attached to the graphitization system, it is pumped on and vacuumed to <10 microns using a scroll pump. The combustion tube is pumped on during the entire iron pretreatment. After the iron pretreatment is complete, combustion of the wood shavings and copper oxide (the source of oxygen) is at 950°C until the pressure of gas in the combustion tube levels out. This takes 40-60 minutes. The heater temperature is then lowered to 600°C to allow any remaining oxygen to re-react with the copper to reduce the amount of oxygen transferred to the graphitization tube. The heater is kept at 600°C until the gas pressure again levels off which takes 20 minutes.

The CO₂ is now transferred from the combustion tube to the graphitization tube. During the transfer, the gas is directed through a water trap surrounded by a dry ice and ethanol slush to

freeze out water and other contaminants produced during combustion. Once the gas is in the graphitization tube, the CO₂ is deposited using LN₂. The remaining gases are pumped away before reducing CO₂ to graphite.

C: Graphitization. This is the process of chemically reducing CO₂ to graphite. The pressure of CO₂ is measured at room temperature. Then H₂ is introduced into the system so that the oxygen will react with the hydrogen, breaking the bonds between the carbon and the oxygen. This is explained via the chemical processes⁶:



It was decided to use 2.3 parts H₂ to 1 part CO₂ based on research conducted by M. Nemeč, et. al.⁶ The desired amount of H₂ to be introduced into the system is calculated using the room temperature pressure of carbon dioxide times 2.3 times 0.75 to account for the pressure difference between room temperature and the temperature of the tube with LN₂ around it to keep the CO₂ from escaping while adding the H₂. The first stage of reduction, where the first chemical equation dominates, is at 950°C for 90 minutes with the dry ice/ethanol slush on the cold finger to trap water. The second stage of reduction, where the second chemical equation dominates, is at 600°C with LN₂ on the cold finger until the pressure levels off. This takes approximately five hours. The result is a very black sample of graphite embedded into the iron matrix. The graphitized sample is removed from the graphitization line, exposing the sample to atmosphere. The outside of the quartz tubing is labeled and parafilm is put over the top of the tube. The first sample sat for 22 days before being loaded into the AMS line.

Packing. A sample is put into a cathode to hold the carbon source during a run. Packing is done by loading the sample into the back of the cathode and then using a rod and hammer to

compact the graphite and iron. There is a platform sticking into the front of the cathode to create a uniform surface during packing. Uniform packing throughout the cathode improves the sample current during AMS measurement.

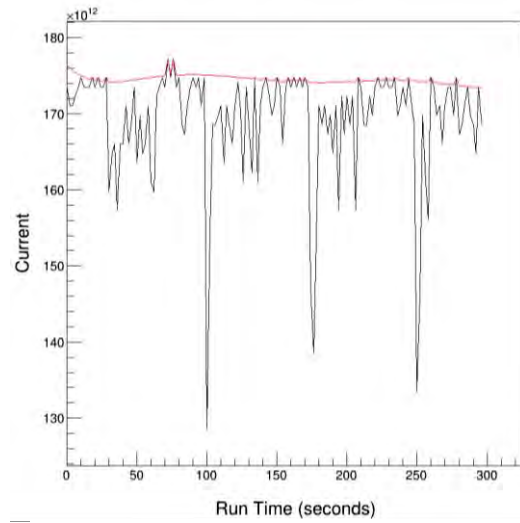
AMS. Once the cathodes are loaded into the 40-cathode wheel, the wheel is loaded into a vacuumed ionization chamber at the beginning of the accelerator line. Cesium is sent toward the surface of the cathode to sputter the carbon from the sample and ionize the carbon to a negative 1 charge state. The ionized carbon is then directed through an electrostatic analyzer to filter by energy and a magnet to filter by mass. Then the beam enters the FN-tandem accelerator. In the FN accelerator, the negative carbon is accelerated toward a positive charge in the middle of the accelerator. In the middle of the accelerator, the beam goes through foils to strip electrons from the carbon so the carbon is in a positive charge state. The positive carbon is accelerated again as it is repelled away from the positive terminal. The desired charge state of positive 3 is selected using another magnet. Then the beam passes through a Wein filter to select the desired velocity. The beam is then directed into the detector. This detector is a parallel grid avalanche counter (PGAC) which measures the x-position of an ion passing through the detector. The location of an event measured by the PGAC is used to determine whether the event is from ^{14}C . The location of counts per two seconds intervals are recorded and then analyzed after the run.

Results

Two cathodes per sample were graphitized and measured using AMS. The primary data is ^{14}C counts per time on the PGAC and ^{12}C particle current per time which is used to calculate the amount of ^{12}C in the sample. The measured current was very noisy and was cleaned. An example of the current from one of the measurements of the museum #5 sample is pictured on the right. The black line is the measured current. The red line is the current used in calculations,

which is the best representation of the current behavior during the runs as verified by offline runs.

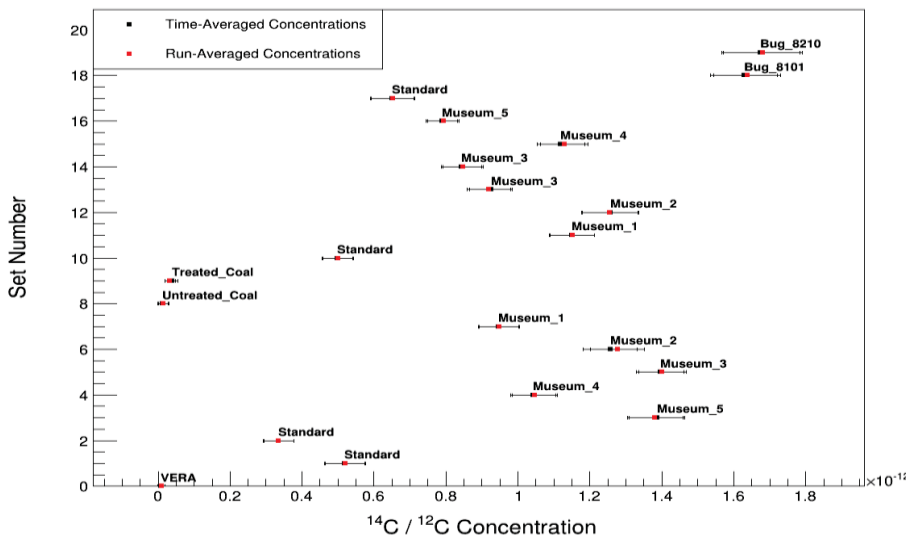
The machine and samples are calibrated using standards of oxalic acid that were graphitized. This also accounts for the transmission factor of the beam through the machine at different times of the run because the standards were measured periodically and the unknowns were corrected using



Measured current (black) compared to cleaned current (red)

the two standards measured before and after the unknown. Following is a table and a diagram of $^{14}\text{C}/^{12}\text{C}$ ratios found using the cleaned current. The ratio was determined by two processes which have similar results. The first process, labeled “time-averaged,” was calculated by dividing the ^{14}C in two seconds by the ^{12}C counts from the current in those two seconds and then averaging across the time of the run. The second process, labeled “run-averaged,” was calculated by dividing the total ^{14}C counts by the total current during the run.

These concentrations were then corrected for ion fractionation due to the different mass ratios of ^{14}C and ^{12}C . The corrected concentrations were then plugged into OxCal, a tool created



by Oxford to calculate the age of a sample. The dates include several age ranges and the percent of likelihood for the sample to be from that time period. Below is a table of data from the OxCal calculations.

$^{14}\text{C}/^{12}\text{C}$ calculated ratios comparing the two methods of averaging counts in a run series on once cathode.

| Sample | Graphitization Date | Run-Averaged | | Time Averaged | |
|-----------|---------------------|--------------|------------------|---------------|----------------|
| | | % Likelihood | Age Range | %Likelihood | Age Range |
| Museum #1 | 6-Jul-17 | 95.4 | 848BC - 1085AD | 95.4 | 866BC - 1067AD |
| | 28-Jun-17 | 79.5 | Prior-1893 | 79.5 | prior - 1893 |
| | | 15.9 | 1906 – 1954 | 15.9 | 1906 - 1954 |
| Museum #2 | 2-Jul-17 | 32 | 1664 – 1787 | 34.5 | 1664 - 1787 |
| | | 48 | 1791 – 1958 | 50.8 | 1790 - 1958 |
| | | 15.4 | 1987 – Present | 10.1 | 1990 - present |
| | 29-Jun-17 | 35.1 | 1664 – 1788 | 34.9 | 1664 - 1788 |
| | | 51.1 | 1789 – 1958 | 50.8 | 1789 - 1958 |
| | | 9.2 | 1990 – Present | 9.7 | 1990 - present |
| Museum #3 | 8-Jul-17 | 16.9 | 1957-1962 | 16 | 1957 - 1962 |
| | | 78.5 | 1979 – 2006 | 79.2 | 1979 - 2007 |
| | | | | 0.2 | 2008 - 2008 |
| | 8-Jul-17 | 95.4 | 1882 BC - 265 AD | 95.4 | 1914BC - 232AD |
| | 30-Jun-17 | 95.4 | 1199BC - 914AD | 95.4 | 1151BC - 964 |
| Museum #4 | 10-Jul-17 | 95.4 | prior – 1655 | 95.4 | prior - 1655AD |
| | 1-Jul-17 | 43.2 | prior – 1669 | 54.5 | prior - 1666AD |
| | | 38.8 | 1781 – 1798 | 40.9 | 1783 - 1796 |
| | | 13.5 | 1945 – 1951 | | |
| Museum #5 | 13-Jul-17 | 4.2 | 1681 – 1738 | 3.6 | 1681 - 1738 |
| | | 0.2 | 1745 – 1748 | 0.4 | 1755 - 1762 |
| | | 0.7 | 1750 – 1763 | | |
| | | 10.2 | 1802 – 1938 | 8.8 | 1803 - 1937 |
| | | 12.5 | 1802 – 1938 | 13.3 | 1952 - 1962 |
| | | 67.6 | 1976 – present | 69.4 | 1976 - present |
| | | 26-Jun-17 | 95.4 | 1262 – 1261 | 95.4 |

Conclusion

There are very large age ranges for many of the samples, especially once different cathodes of the same sample are cross-referenced. For example, the first cathode for museum #1 has a date range of 848BC – 1085AD while the second cathode has date ranges of any time before 1893 and 1906—1954. Museum #2 has the best correspondence between cathodes with the date ranges differing by a couple of years. The age ranges are so vast because of an

undesirably large error for the counts. These cathodes will be remeasured by the AMS group to identify any potential sources for these differences.

Acknowledgements

Many thanks to my fellow collaborators Connor Bagwell, Adam Clark, and Austin Nelson who contributed many hours to graphitizing. Thanks also to the graduate students Adam Clark, Austin Nelson, Michael Skulski, and Tyler Anderson for training Connor and myself on graphitizing, setting up the graphitization line, and for taking AMS measurements. Thank you to Michael for helping analyze the data. Thank you to my advisor, Dr. Philippe Collon, for his guidance on this project. Thank you as well to the National Science Foundation and JINA-CEE for the funding to participate in research this summer.

References

- [1] McNichol, A. P., Jull, A. J., & Burr, G. S. (2001). Converting AMS Data to Radiocarbon Values: Considerations and Conventions. *Radiocarbon*,43(2A), 313-320.
doi:10.1017/s0033822200038169
- [2] University of Oxford, <https://c14.arch.ox.ac.uk/calibration.html>
- [3] Kutschera, W. (2013). Applications of accelerator mass spectrometry. *International Journal of Mass Spectrometry*,349-350, 203-218. doi:10.1016/j.ijms.2013.05.023
- [4] (n.d.). Retrieved July 20, 2017, from <http://www.nndc.bnl.gov/chart/reCenter.jsp?z=6&n=8>
- [5] Kutschera, W., & Paul, M. (1990). Accelerator mass spectrometry in nuclear physics and astrophysics. *Annual Review of Nuclear and Particle Science*, 411-438.
<http://www.annualreviews.org>
- [6] Němec, M., Wacker, L., & Gäggeler, H. (2010). Optimization of the Graphitization Process at Age-1. *Radiocarbon*,52(03), 1380-1393. doi:10.1017/s0033822200046464

Controlling Electronic States With Strain Engineering

JOHN WALKER

ADVISOR: PROFESSOR KENJIRO GOMES

GOMES LAB, UNIVERSITY OF NOTRE DAME, REU SUMMER 2017

Abstract

Electronic bands and bandgaps play a pivotal role in the electronic properties of a material. The ability to finely adjust the size and position of these phenomena could go a long way toward creating customizable LEDs, solar cells, and other circuitry. Our research dealt primarily with simulating the effects of mechanical strain on the formation of bandgaps in a variety of 1D and 2D arrangements of atoms. The goal was to find a realistic way to strain a material such that we could tune the bandgap to a desired size. Attempts we made to apply simple overall strain to a 2D lattice of atoms yielded behavior that approached a 1D system. Bandgaps in both 1D and 2D systems can be directly tuned with more complex strain, but implementation of these effects in any real-world device seems difficult.

Introduction

Manipulation of electronic bandgaps has typically been achieved through a complicated process of growing and doping semiconductor crystals in a very complex fashion. As evidence of just how difficult this can be, the Nobel Prize in physics in 2014 was given to three Japanese scientists, Akasaki, Amano and Nakamura, for creating the first blue LED [1]. This meant that LED sources of white light, which are longer lasting and much more efficient than both incandescent and fluorescent lights, could finally be made—a significant feat which has helped to reduce consumption of natural resources and brought effective lighting to off-grid areas with limited electricity access.

Rather than mixing together very specific semiconductor crystals to produce a particular wavelength of light, our research aims to provide a basis for tunable LEDs which could potentially give off any range of colors. In a case similar to ours, a team of scientists at several universities collaborated to publish a paper in *Advanced Materials* describing the straining of

both natural and artificial concentrically-layered fibers. They found that they could directly manipulate the photonic bandgap of the fibers through strain thanks to Bragg's law, $n\lambda = 2d \sin \theta$ [2]. Strain directly impacts d , and therefore the primary color of light being reflected from the substance at a given angle of observation, θ . We attempt to utilize similar strain tactics in simulated structures to manipulate the electronic bandgap as opposed to the photonic bandgap.

Theory

Basic atomic theory teaches us that electrons fall into discrete orbitals around atomic nuclei. As many atoms are brought together, the energies of electrons occupying each orbital don't necessarily align. Instead, they spread out to form nearly continuous bands of allowed energies centered around the original orbital energy. This is shown in Figure 1.

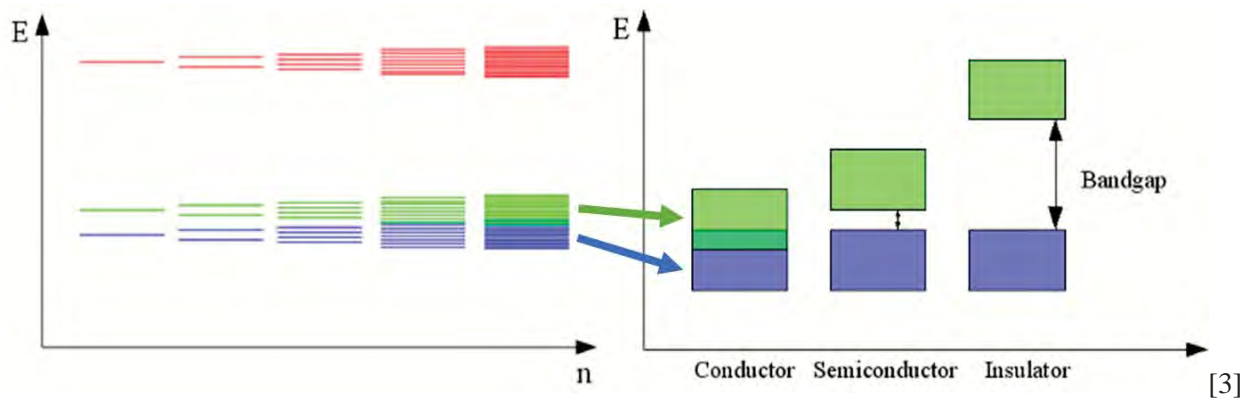


Figure 1: As n , the number of atoms, increases, orbitals blend together into nearly continuous bands. Depending on the relative position of these bands along the energy (E) axis, and their position relative to the fermi energy, we can wind up with a conductor, a semiconductor, or an insulator. These are marked by an overlap, small gap, or large gap between bands respectively.

Tight binding theory provides a means for understanding the formation of these bands [4]. As atoms are brought closer together, we model each nuclei's "pull" on electrons as a potential well of a certain energy E , and the strength of the bonds between each atom with a bonding term, t . These two general terms are all we need to assemble a Hamiltonian that describes any given 1D or 2D system of interest to us. The potential energy terms representing each atom run along the

main diagonal such that each term has both a unique row (i) and column (j). The bonding term, t , representing the bond between the atom in row i and the atom in column j is then placed in position (i,j) and position (j,i) . In our case, we only consider bonding between nearest neighbors.

The eigenvalues of this Hamiltonian represent the allowed energies. Since these energies are not necessarily evenly spaced, a histogram of the energies can be made to represent the density of allowed energies, also known as the density of states (DOS). It is through this plot of the DOS that we can identify bands and bandgaps. In our case, we produced continuous histograms by summing a series of Lorentzian curves of a relatively narrow width centered at each allowed energy. Figure 2 shows an example of a simple arrangement of atoms and its corresponding Hamiltonian. For larger systems, this process remains the same and winds up producing very large Hamiltonians. We used MATLAB for diagonalization.

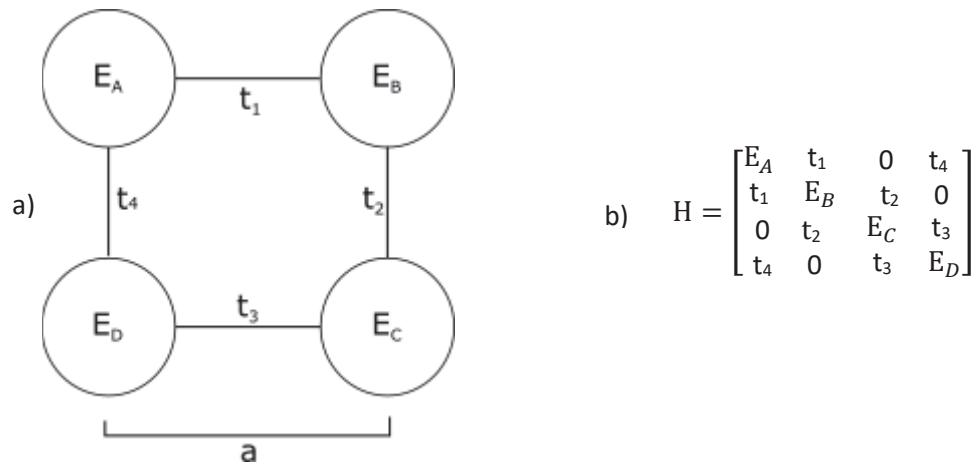


Figure 2: a) A basic 2D structure. The E terms represent the “depth” of the potential wells which in turn represent atoms. The t terms represent the bonding strength. ‘ a ’ represents the distance between atoms, which is held constant. b) The Hamiltonian describing the system in ‘a’. The bonding term for the potential in row i and the potential in column j is found at position (i,j) and (j,i) . Typical values for E ’s are 0 and 1, and typical values for bonds are -1 and -2. Units are arbitrary.

Two further options for studying the systems in question were considered but didn’t have time to develop. One was the use of a scanning tunneling microscope (STM) in conjunction with carbon monoxide (CO) molecules on a copper surface (Cu (111)) to create artificial versions of

the structures we are simulating with the previous method. The STM could then directly measure the DOS at any given position in the material. The second is the use of multiple scattering theory to replicate the functionality of the STM within MATLAB. In the former case, due to time constraints, the STM hasn't yet been used directly for this study. In the latter case, the model wasn't studied enough to provide useful commentary on the results of the tight binding method.

In all structures we studied, we started with a unit cell and then repeated that cell as many times as reasonable for the computational power we had at our disposal. In the 1D case, our unit cells consist of three potentials and two bonds. To form the full structure, each cell is placed immediately next to the former with the outside potentials overlapping. See the top of Figures 3 and 4 for an illustration of this translational symmetry. In the 2D case, this same idea is used, except the unit cell is any square connecting four potentials with one in the middle rotated at 45 degrees relative to the horizontal as seen in the top right of Figure 6 and Figure 5a.

Results and Discussion

In 1D, the structure and DOS of a homogenous string of atoms and bonds is shown in Figure 3. Peaks exist right at the highest and lowest allowed energies with a minimum in the middle. Stretching a string of atoms results in a retention of the same shape but with a smaller range of allowed energies (the range of E is roughly proportional to $4t$) and relatively less extreme variance between the peaks and the minimum in the middle. Compressing produces the opposite effect. A bandgap doesn't open in either case.

In order to open a gap, we must alternate either the bond strengths or the potential strengths as shown in Figure 4a and 4b respectively. The former opens a gap directly in the middle with a size of two times the difference in the bond strengths. The latter opens a gap with edges at the

energy corresponding to the energies of the potentials (i.e. bandgap edges at $E = 0$ and $E = 1$ if one potential is zero and the other is one, but note that the units are arbitrary). In both cases, the edges of the gap form peaks as if the states that were formerly in the gap were shoveled up and piled up on either side.

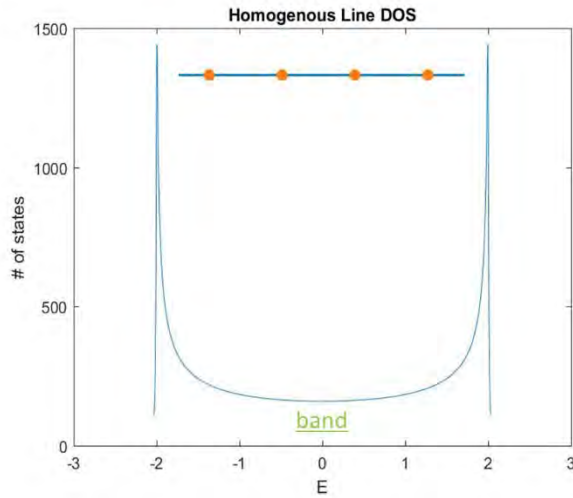


Figure 3: Illustration and DOS for a line of identical atoms and bonds. The circles represent atoms, and the lines represent bonds. This illustration is only an excerpt of a much longer line. The DOS forms a single band; note the "U" shape. The potentials were all 0, and the bonding terms were all -1. E is in units of t .

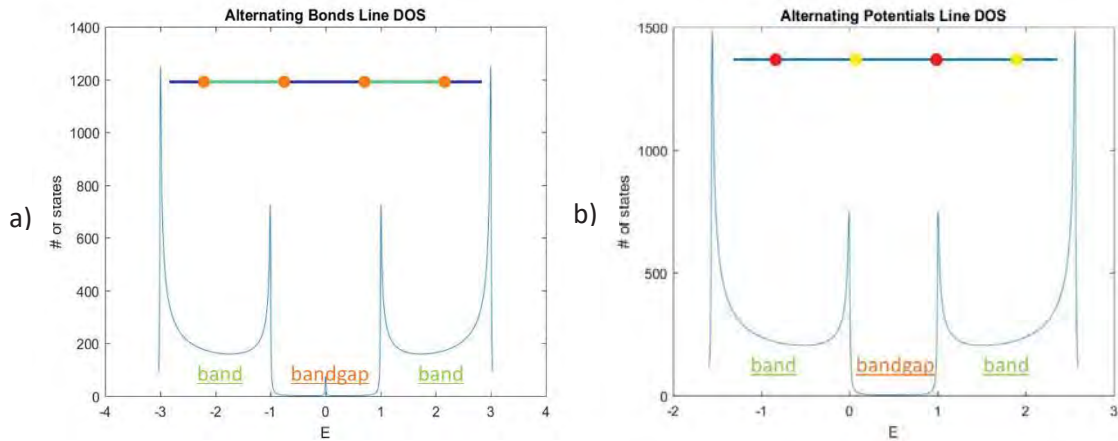


Figure 4: a) Illustration of the lattice and DOS for the case of alternating bonds. The potentials were all 0 and the bonds alternated between -1 and -2. b) Illustration of the lattice and DOS for the case of alternating potentials. The potentials alternated between 0 and 1 while the bonds were all -1. In both images, the circles represent the potentials, and the lines represent the bonds. Colors reflect the alternating patterns used. E is in units of t . Bands and bandgaps are labeled.

In 2D, the DOS of a homogenous square lattice is a peak shown in Figure 5a. In this case, stretching the lattice along one axis causes the peak to split as shown in Figure 5b. In the middle,

a valley forms, and the entire shape of the DOS begins to approach the shape of the 1D case as seen in Figure 3. This makes sense since the bonds being stretched will tend to weaken, and, in the extreme case, go to zero, causing the entire lattice to resemble a series of 1D strings of atoms. Similar to the 1D case, the range of E is roughly proportional to $8t$, meaning that stretching again causes a smaller range of E 's while compressing does the opposite.

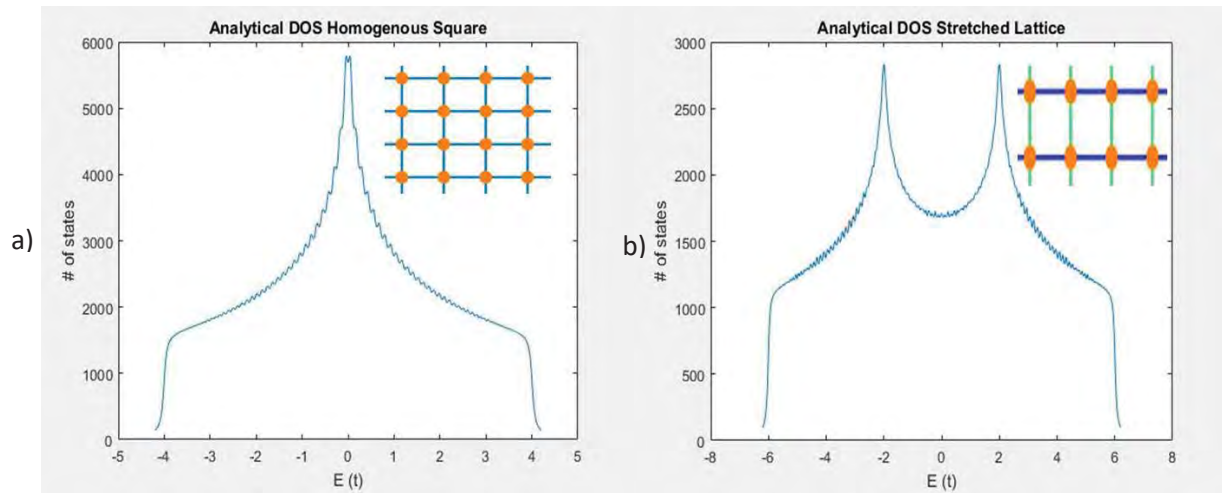


Figure 5: a) Illustration of the lattice and DOS for the case of a homogenous square lattice. The potentials were all 0 and the bonds were all -1. The DOS forms a peak about $E=0$. b) Illustration of the lattice and DOS for the case of a stretched square lattice. The potentials were all 0 while the horizontal bonds were -2 and the vertical bonds were -1. The “U” shape characteristic of a 1D system begins to form about $E=0$. In both images, the circles represent the potentials, and the lines represent the bonds. Colors in ‘b)’ represent variation in magnitude. The little bumps are due to small gaps between the tips of the Lorentzian distributions used to form the histogram.

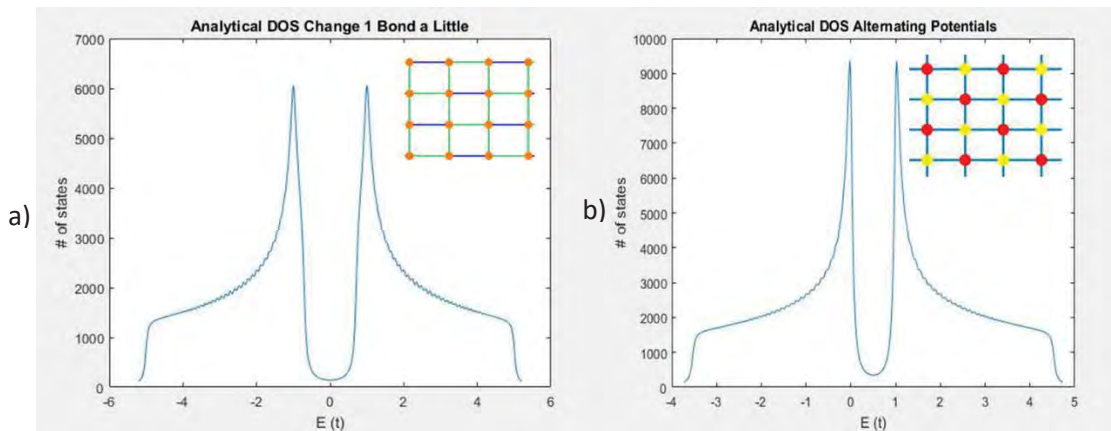


Figure 6: a) Illustration of the lattice and DOS for the case of a square lattice with alternating bonds. The potentials were all 0 and the bonds alternated between -1 and -2 along the horizontal and remained -1 along the vertical. b) Illustration of the lattice and DOS for the case of alternating potentials. The potentials alternated between 0 and 1 and the bonds are all -1. In both images, the circles represent the potentials, and the lines represent the bonds. Colors represent variation in magnitude. A bandgap is opened in both DOS plots.

Once again, to open a gap, we must alternate either the bond strengths or the potential strengths. In 2D, it is slightly more complicated since there are more ways to achieve alternating translational symmetry. The only way to make it work is to alternate along both axes as shown in Figure 6. Again, the peak splits, but the valley in the middle goes to zero. The position and size of the gap is identical to the 1D case, as is the effect wherein peaks are observed immediately on the edges of the gap.

As previously mentioned, there are many more combinations of strains in the 2D case. However, all other combinations that I observed led only to small variations in the same general peak structure. It remains possible that there are more ways to open a gap, but they either didn't merit mentioning or went unobserved in the course of this study.

Finally, in both the 1D and 2D cases, we observe that the effects of altering the potentials and the bonds at the same time results in independent behaviors that superimpose without interacting in any significant way. Figure 7 illustrates this in the 2D case.

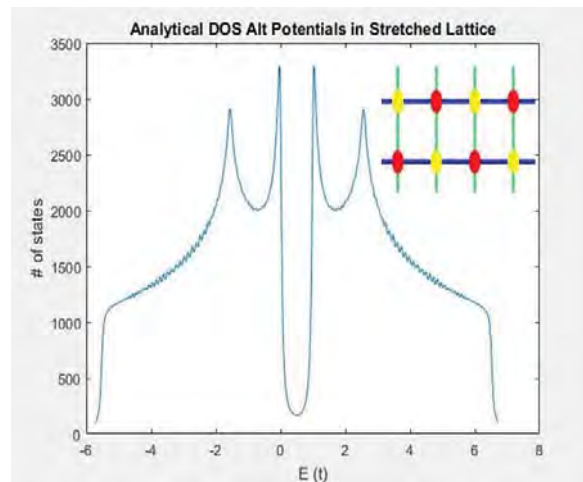


Figure 7: Illustration of the lattice and DOS for the case of a stretched square lattice with alternating potentials. The potentials alternated between 0 and 1. The vertical bonds were -1 while the horizontal bonds were -2. The circles represent the potentials, and the lines represent the bonds. Colors represent variation in magnitude.

Conclusion

Control of bandgaps provides a promising way of tuning diode behavior for implementation in many different applications. Unfortunately, in both the 1D case and the 2D case, we see that we are unable to form or manipulate bandgaps through overall strain of a material. However, if we are able to come up with a method of manipulating bond strengths on a per-atom basis that doesn't involve merely changing the bond type (i.e. single bond vs double bond), we can form and manipulate a bandgap proportional to twice the difference in energy between the two bonds. This seems difficult, but remains a possible route for future study. One specific idea is to investigate whether manipulation of larger collections of atoms (as opposed to single atoms) could lead to the same effect while being more practical.

References

- [1] BRIGHT, T. (2014). Efficient blue light-emitting diodes leading to bright and energy-saving white light sources. *Sci. Backgr. Noble Prize Phys*, 1-9.

- [2] Kolle, M., Lethbridge, A., Kreysing, M., Baumberg, J. J., Aizenberg, J. and Vukusic, P. (2013), Bio-Inspired Band-Gap Tunable Elastic Optical Multilayer Fibers. *Adv. Mater.*, 25: 2239–2245. doi:10.1002/adma.201203529

- [3] https://homofaciens.de/technics-semiconductor-diode_en.htm

- [4] Simon, S. H. (2016). *The Oxford solid state basics*. Oxford: Oxford University Press.

Simulation of an Atmospheric Pressure Plasma Jet via COMSOL

Wei Zha

2017 NSF/REU Program
Physics Department, University of Notre Dame

Advisers: Sylwia Ptasinska, Vladimir Samara

1.Introduction

1.1 Atmospheric Pressure Plasma Jet

Plasma is ionized gas composed of charged particles, radicals, neutrals, photons and electromagnetic fields.[1] Naturally, plasma is often at high temperature and pressure. In our case, we use a method to generate plasma of low temperature at normal pressure.[2] Detailed experimental setup is in reference [1]. This plasma can be used for medical treatment and other biological manipulations, which we call atmospheric pressure plasma jet.

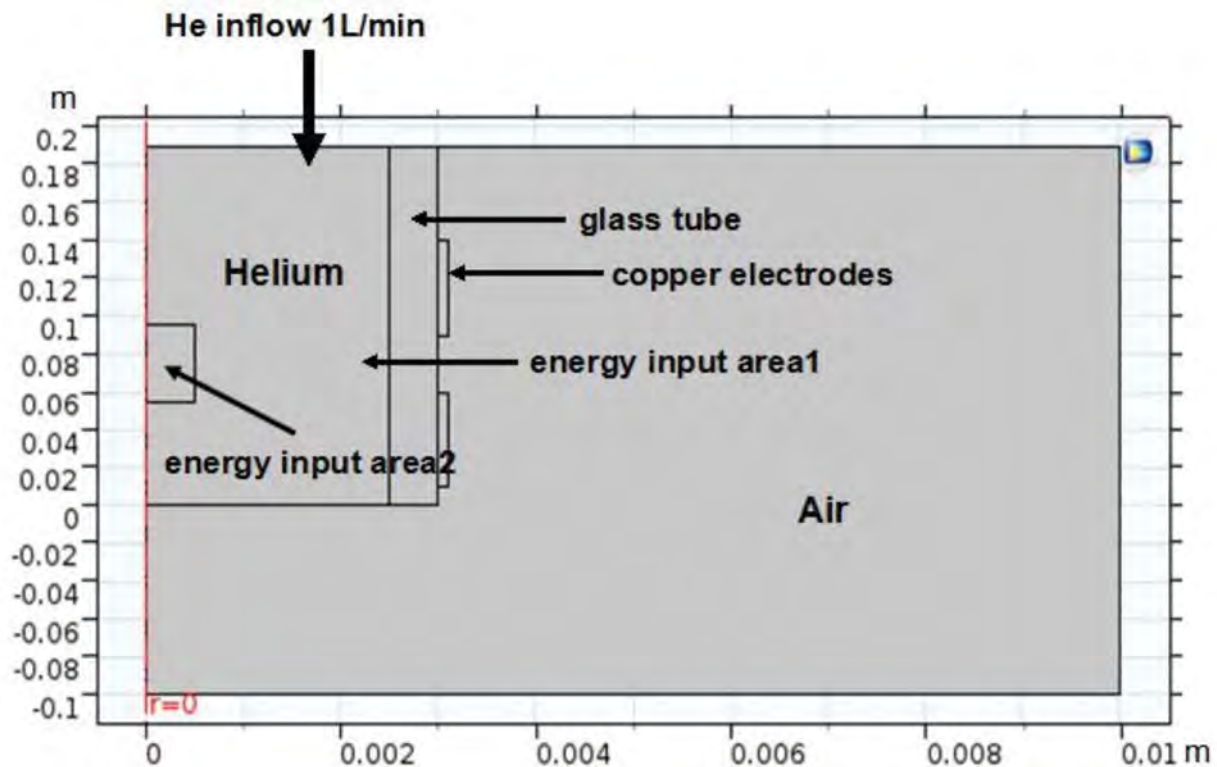
1.2 COMSOL and finite element method

COMSOL Multiphysics is a software to do analysis, solution and simulation by using finite element method. Finite element method is a numerical method used to derive estimated values of solutions to partial differential equations.

1.3 Aim of my work

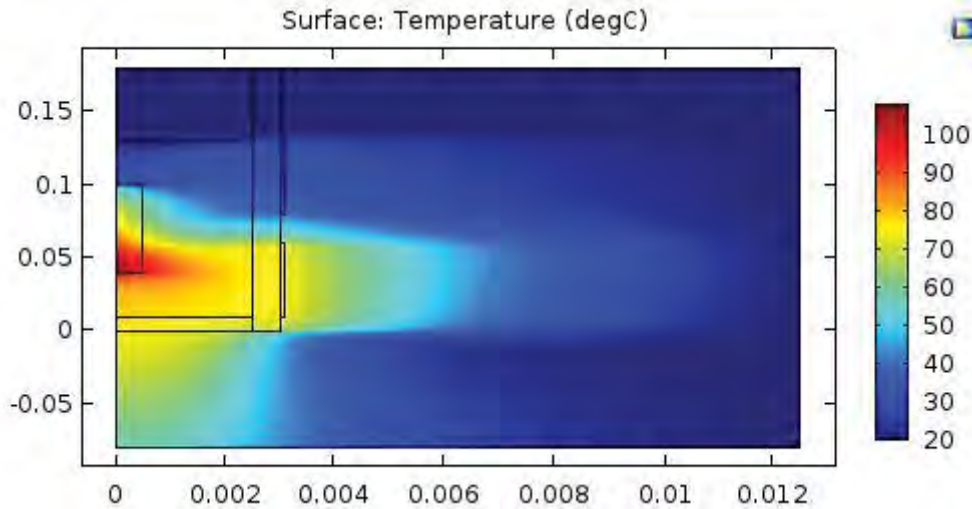
We do simulations by setting up physical models. After solving the model, we derive values of physical quantities and compare them with experimental data. In changing input parameters, we can investigate how well simulation fits with experiment, and thus find out the best set of relevant parameters. Using this well fitted model, we can derive more variables which are difficult to measure directly, and cooperate with experimentalists.

2. Model setup



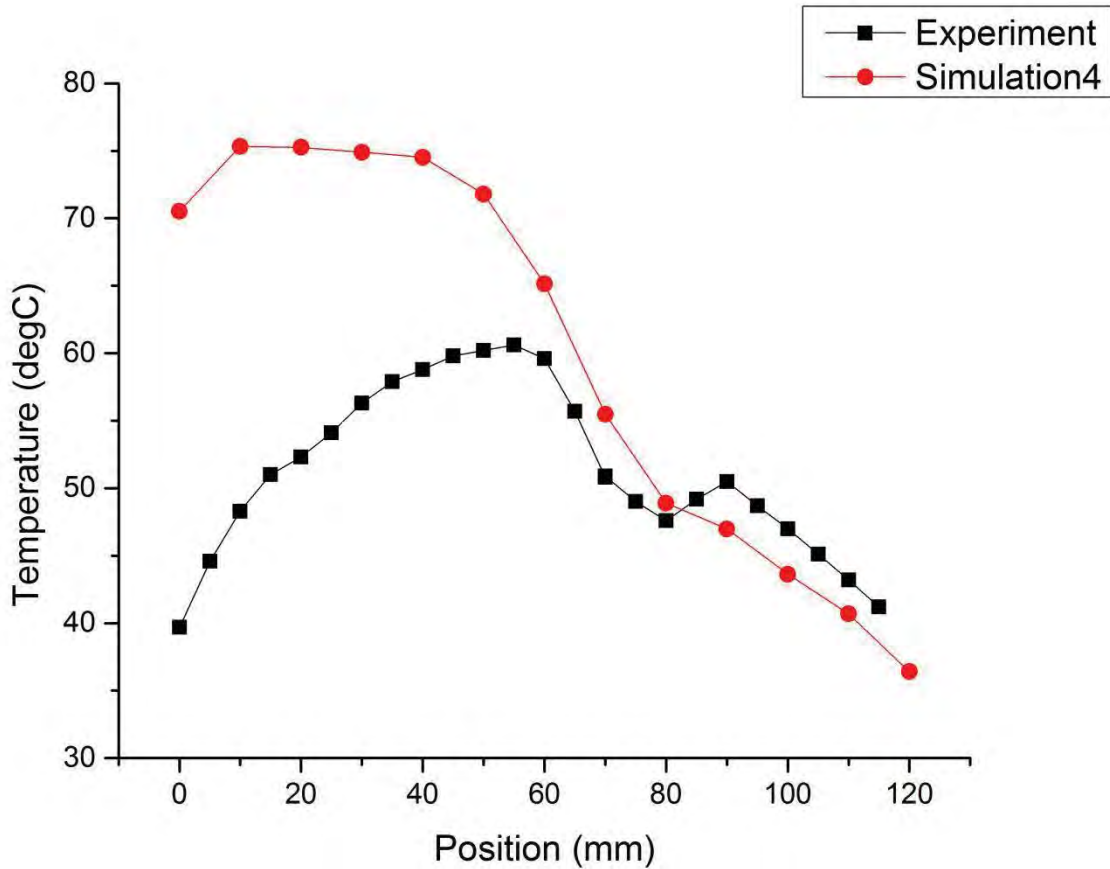
In the picture we show our setup for simulation, which is exactly the same as that of experimental setup. We use an axial symmetric geometry, and all boundaries are set as room temperature. It is difficult to simulate plasma, so we make simplifications. We have two areas of power input because we firstly use thermal energy input as alternative of plasma, in which case, plasma is denser in area 2 and is distributed throughout the whole area 1. As you can see in the picture, the radius of the tube is 2.5mm, and the length of the tube is over 14mm. However, these lengths are not fixed because we can adjust these setups both in our experiment and our simulation model.

3. Simulations



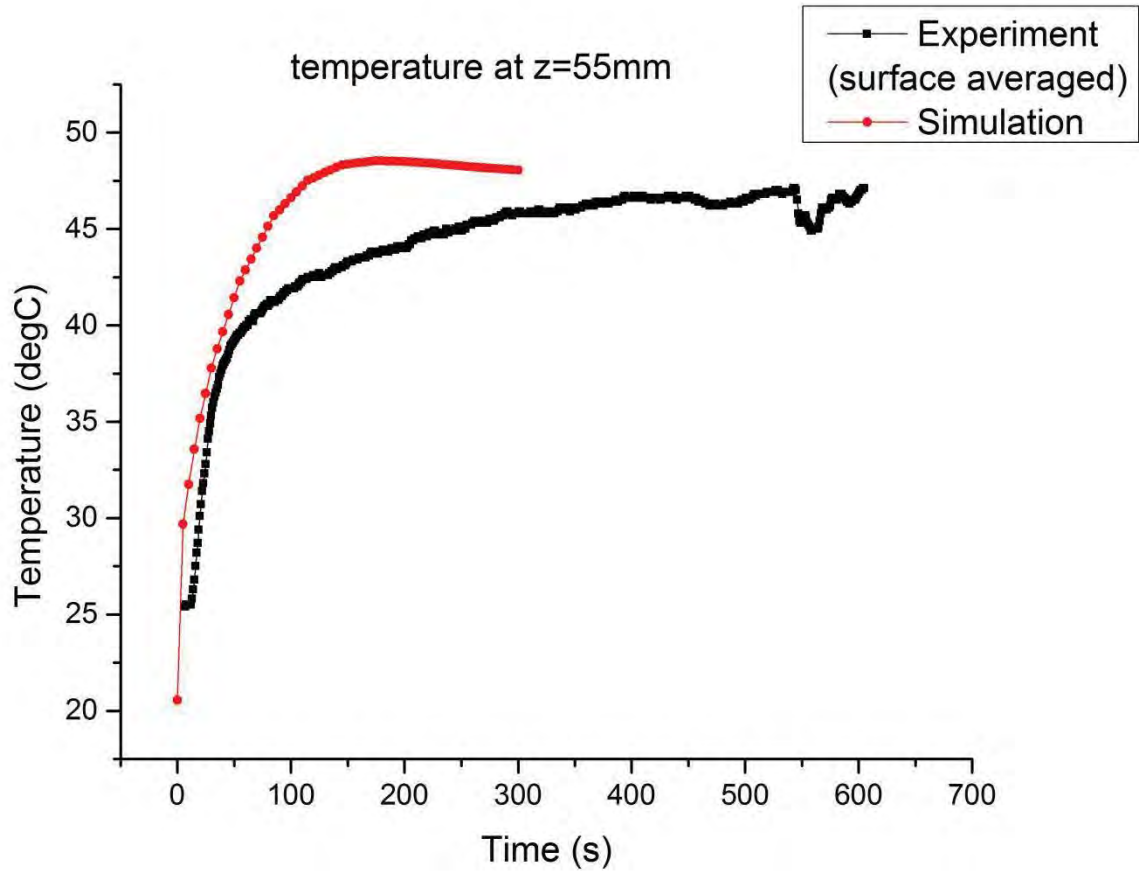
As you can see, the figure above is one plot of temperature in solved model. We derive our data by solving partial differential equations using COMSOL.

In simulation, we derive average temperature of a cut plane in the tube. We also have experimental data of temperature in tube so we compare the two to adjust the model. COMSOL can derive estimated values wherever you want, but we choose several cut planes because it is time-costing and complex to compile a calculation of too much data, as several typical data can show the trend of temperature and are enough for comparison.



The figure above is our final version of temperature fitting. The region from 60 to 120 in position are kind of what in our expectation, for it is fitting well with experimental data. The region from 0 to 60 in position, however, is not fitting well. In experiment, we have a rapid drop near the exit of the tube while in simulation there is not. The reason why we get such inconsistent results is still under discussion, but we have some hypotheses. One reason can be failure in simulation of helium flow near the exit. We discovered that in experiment, helium flow near the tube is always fluctuating and doesn't have a stable position. There can be turbulent flow to help cool down the helium. In our simulation, however, we treat the whole helium flow as laminar flow. Another reason can be neglecting convection in our model.

We also did time-dependent simulations to compare with our experimental work. Below is the figure of comparison between simulation and experiment.



We derived average temperature at $z=55\text{mm}$ from our solution of the model, which was solved as time-dependent result. We can see that in the picture, two sets of data have similar trend. The time needed to get to equilibrium and ultimate temperature are close. Considering it is difficult to simulate plasma, it is acceptable result already.

4. Summary

We found a relatively well-fitted model, which deserves more discussion and improvements. We already did some cooperation with experiments. As a student, I am now experienced in using

COMSOL to do simulations. Also, I learned about what is it like to do research by doing simulations.

In future, we can improve my work in the following directions: firstly, we didn't finish our temperature fitting because of limited time. We can continue on doing this work in order to improve our model. More work over sweeping parameters and finer adjustments can be done to optimize our model. Secondly, we can add other physics into our model. Turbulence and chemical reactions can be good choices because they are not taken into account in our model. However, in fact they do play an important role, according to both our experimental works and other group's works. After solving these factors, we can add electrical and magnetic field into the system, then add plasma module in COMSOL to really simulate plasma.

In short, our simulation work is prospective and meaningful, and at the same time, in need of effort.

5.Acknowledgments

I would like to thank Ptasinska Group, especially my advisers, Prof. Ptasinska and Dr. Samara. Also, many thanks are in order to those who help me improve my report. It is a great experience to be a member of the group.

I would also like to thank Prof. Garg, Ms. Lori Fuson and Ms. Nell Collins for wonderful REU activities.

Last but not least, thank Notre Dame.

6.References:

[1] Effects of Atmospheric Pressure Plasmas on Isolated and Cellular DNA--A Review,
K.Arjunan, V.Sharma, S.Ptasinska

[2]The Atmospheric-Pressure Plasma Jet: A Review and Comparison to Other Plasma Sources,
A.Schutze, J.Jeong, S.Babayan

Ferromagnetic Resonance in III-Mn-V Nanostructures

Xucheng Zhang

2017 NSF/REU Program

Physics Department , University of Notre Dame

Advisors:

Jacek Furdyna

Xinyu Liu

Abstract

Magnetic properties of $\text{Ga}_{1-x}\text{Mn}_x\text{As}$ and $\text{Ga}_{1-x}\text{Mn}_x\text{As}_{1-y}\text{P}_y$ are measured using Bruker EPR machine. They have, in many ways, exact opposite features, arising from different strain-induced uniaxial anisotropy. In addition to the effect of strain, we also reveal the shape effect on the magnetic anisotropy, which is evident in the spectra of spin waves. One of the spin wave mode is pinned within the thickness of the film, the other is confined in artificial nanopatterns created on the surface of the sample.

I Introduction

Semiconductors and magnetic materials both play essential roles in the modern electronics industry. Most electronic and optical semiconductor devices utilize the charge of electrons and holes to process information; and magnetic materials use the spin of magnetic ions for information storage. Thus—although the applications of semiconductors and magnetics have evolved independently—it appears logical to combine their properties for possible spin-electronic applications with increased functionalities.

Despite the tremendous success in II-VI based magnetic semiconductors, recent studies show that III-V based semiconductors with Mn doping remain ferromagnetic to much higher Curie temperature than those observed in their II-VI based counterparts. These III-V-based ferromagnetic semiconductors are fabricated in thin layer form by low temperature molecular beam epitaxy (LT-MBE).

It is generally accepted that when Mn is incorporated at the cation site of III-V semiconductors it enter the lattice as a Mn^{2+} ion, which has a half-filled d shell with an angular momentum $L=0$

and a spin of $S=5/2$. However, Mn^{2+} ion at the group III cation site do not just serve as $S=5/2$ magnetic moments inserted into the III-V host, but also as acceptors, so that the resulting $III_{1-x}Mn_xV$ alloys automatically contain a high concentration of holes. Figure 1 shows the crystal structure of GaMnAs, magnetic moments carried by Mn^{2+} ions are coupled together by holes, give rise to ferromagnetism in the material.

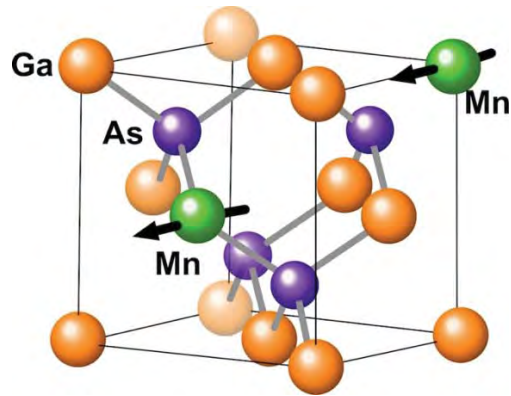


Figure 1: Carrier-mediated ferromagnetism

We use ferromagnetic resonance to study various magnetic properties of III-V-based DMS. Our research shows the strain effect in this type of material, which give rise to a uniaxial anisotropy field. We also show how the spin wave induced in the thin ferromagnetic film is manipulated by different confinement conditions.

II Experiment Setup

2.1 Sample preparation

Our sample is grown by a special technic called molecular beam epitaxy (MBE). MBE allows the deposition and growth of monocrystalline structures. Figure 2 shows a schematic diagram of a MBE machine. The system is placed in a high cleanliness and ultra-high vacuum chamber,

preventing any sorts of contamination and impurities. Beams of molecules are fired from the effusion cell, then they will deposit onto a heated substrate (GaAs in our case) one atomic layer at a time (epitaxially). By varying the deposition rate and also the ratio between different elements, we can precisely control the thickness and impurity ratio of the film.

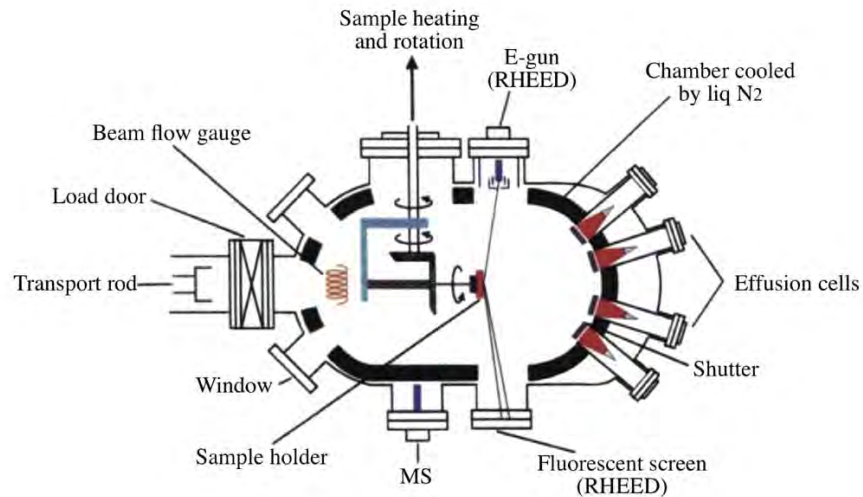


Figure 2: Schematic diagram of the MBE machine

2.2 Coordinate system

All of our samples are in the form of a thin film, and we use Bruker EPR machine to measure FMR spectra in these films. Figure 3 shows the coordinate system in our experiment, the edges of the film are in the $[110]$ and $[1\bar{1}0]$ direction. Magnetic field is kept in the horizontal direction, and we change the angle between the magnetization M and the magnetic field H by changing the orientation of our sample with respect to the magnetic field. Basically, there are two configurations--magnetic field is either in-plane or out-of-plane.

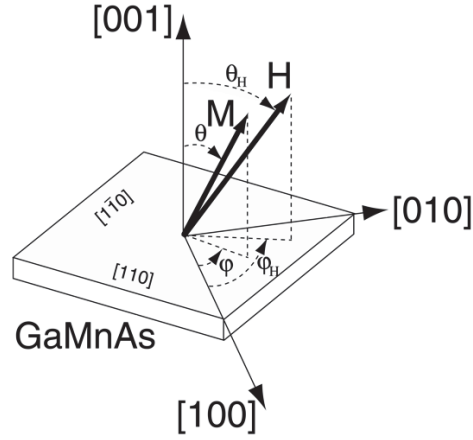


Figure 3: Coordinate system, polar and azimuthal angle of magnetization and magnetic field are (θ, φ) and (θ_H, φ_H) , respectively

III FMR Theory

The time evolution of the magnetization around the equilibrium position can be estimated using the Landau-Lifshitz-Gilbert formulation, which takes into account the damping of the magnetization:

$$\frac{d\vec{M}}{dt} = -\gamma[\vec{M} \times (\vec{H} + \vec{H}_{eff})] + \frac{G}{\gamma M^2} \left[\vec{M} \times \frac{\partial \vec{M}}{\partial t} \right]$$

H is the externally applied dc magnetic field; H_{eff} is the effective magnetic field, which includes the driving rf- microwave field, the demagnetizing field, the magnetocrystalline anisotropy field, and the exchange interaction; $\gamma = g\mu_B\hbar^{-1}$ is the gyromagnetic ratio; G is the Gilbert damping parameter. Note that when damping is considered, the magnetization will try to align itself with the magnetic field. However, if an external magnetic field of the same frequency as the Larmor precession is applied to the system, the energy of the microwave will be absorbed, leaving a sharp absorption peak in the microwave spectrum, i.e. resonance.

IV Experimental result

3.1 Strain effect

Figure 4a shows the FMR spectra observed in a 12nm $\text{Ga}_{1-x}\text{Mn}_x\text{As}$ ($x>0.08$) film. Resonance occurs at a much stronger field in the [001] direction than in all in-plane directions. The reason behind this is that $\text{Ga}_{1-x}\text{Mn}_x\text{As}$ film experience compressive strain, the direction of magnetization (i.e. easy axis) is kept in-plane. Notice that the resonance occurs at different field strength for [110] and $[1\bar{1}0]$, indicating that there're physical difference between these two angles, we attribute that to a small but finite in-plane anisotropy field.

Figure 4b shows the angular dependence of the FMR spectra in the 12nm $\text{Ga}_{1-x}\text{Mn}_x\text{As}$ ($x>0.08$) film. The resonance field has a two-fold symmetry in the normal plane and a four-fold symmetry in the sample plane.

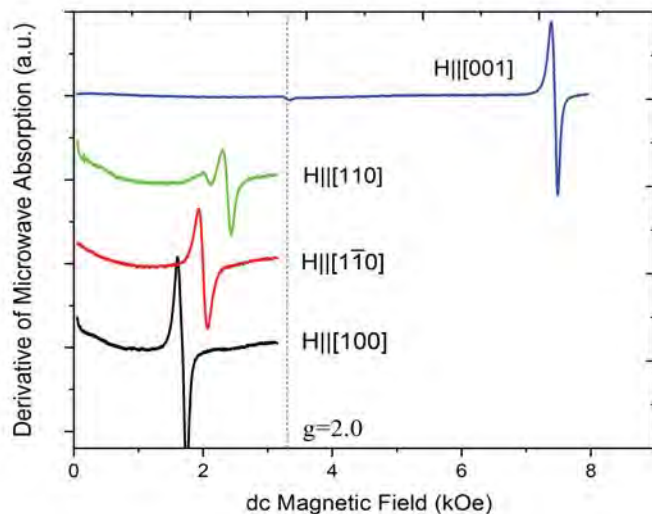


Figure 4a: FMR spectra observed in a 12nm $\text{Ga}_{1-x}\text{Mn}_x\text{As}$ ($x>0.08$) film, plot for four characteristic crystal axes [001],[110],[$1\bar{1}0$] and [100]

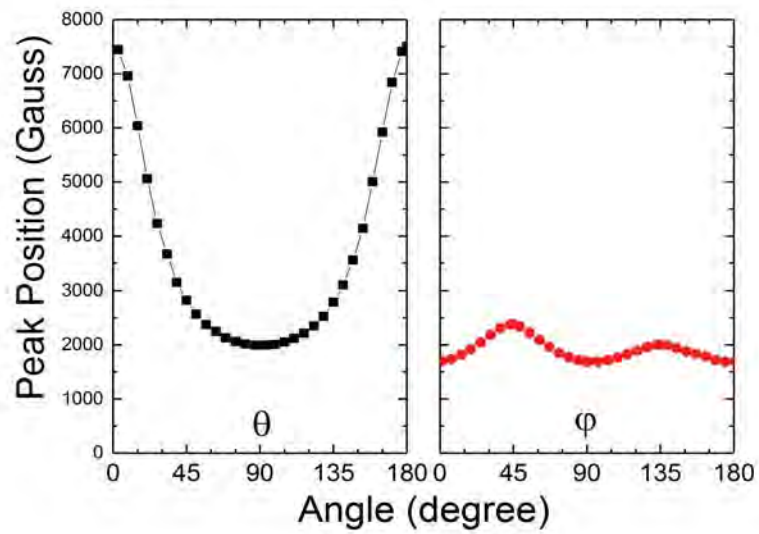


Figure 4b: Angular dependence of FMR spectra observed in a 12nm $\text{Ga}_{1-x}\text{Mn}_x\text{As}$ ($x>0.08$) film

In contrast to GaMnAs, GaMnAsP film experience tensile strain. Figure 5a and 5b shows the observed FMR spectra in a GaMnAsP film. Notice that resonance occurs at a low field strength for out-of-plane direction.

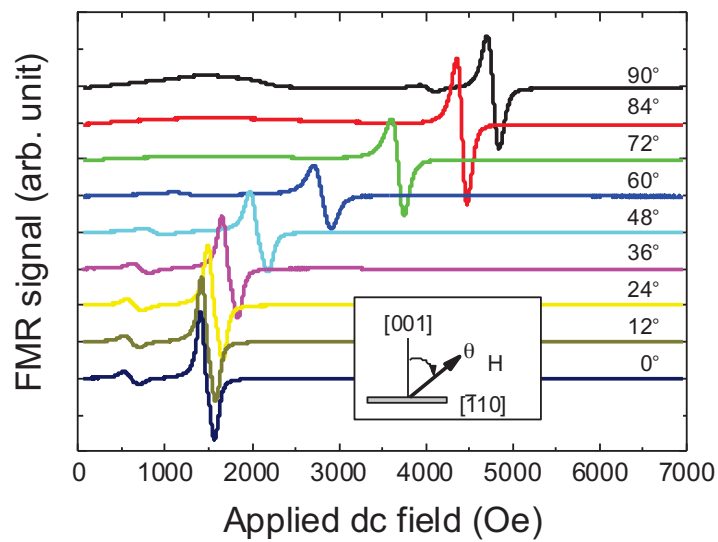


Figure 5a: FMR spectra observed in GaMnAsP film with varying polar angle.

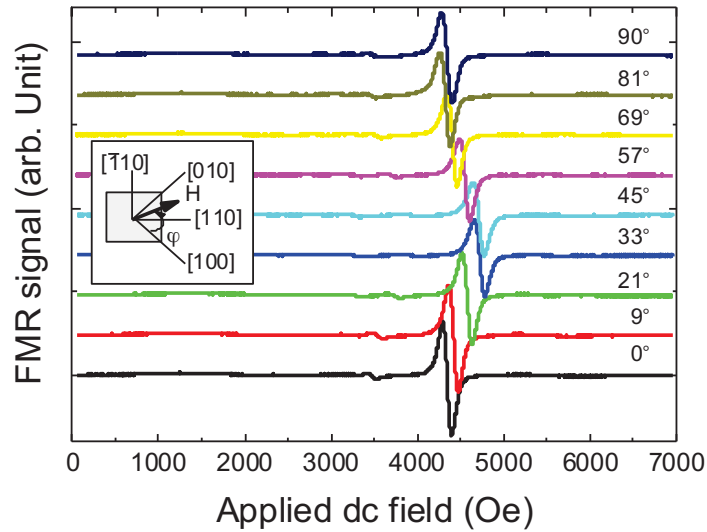


Figure 5b: FMR spectra observed in GaMnAsP film with varying azimuthal angle.

The reason for this transition is that at this time the film is under tensile strain, the easy axis has shifted from in-plane to out-of-plane. We observed similar symmetries in GaMnAsP, except that this time, the normal plane shows a four-fold symmetry and the sample plane shows a two-fold symmetry.

3.2 Spin Wave Resonance

Uniform rf magnetic fields can excite long-wavelength spin waves in thin ferromagnetic films if the electron spins on the surfaces of the film is pinned by surface anisotropy interactions. According to Kittel, a uniform field can only excite spin waves with a odd number of half-wavelength within the thickness of the film. Our experiment reveals clear spin wave signal in the GaMnAsP film.

Figure 5 shows the FMR spectra observed in a 84nm GaMnAsP film. When the magnetization is aligned with the magnetic field, we observe two clear spin wave signals besides the main FMR

signal. When the field is gradually adjust from out-of-plane to in-plane, the observed spin wave mode also changes due to the variation of the surface pinning condition.

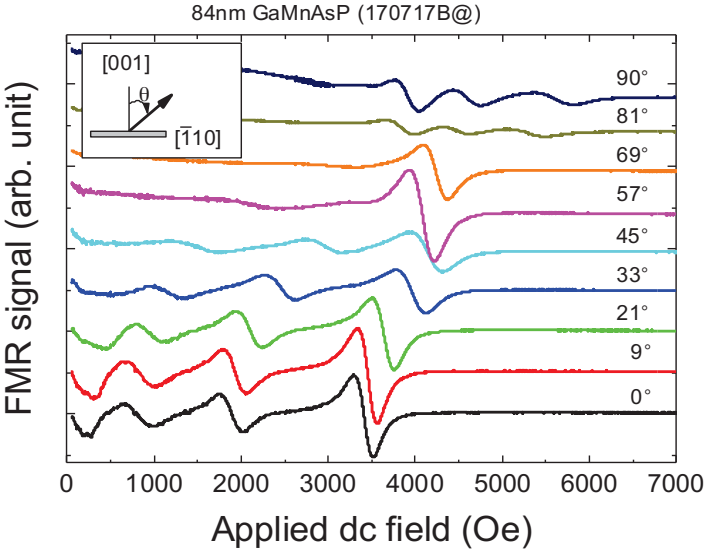


Figure 6: FMR spectra observed in 84nm GaMnAsP flim with varying polar angle

Figure 6 shows the FMR spectra observed in a GaMnAsP film with 400nm-size nanopattern. This time, we see a clear spin wave signal when the magnetic field is in-plane.

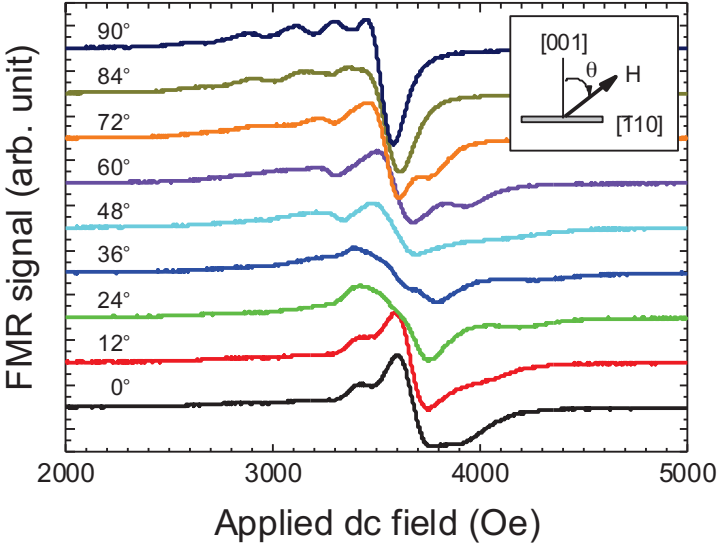


Figure 7: FMR spectra observed in GaMnAsP film with 400nm nanopattern

V Summary

With the combined features of magnetic materials and semiconductors, diluted magnetic semiconductor is the potential candidate for next generation of information processing material. Using ferromagnetic resonance, we are able to reveal a lot of distinct features of DMS, such as magnetic anisotropy and spin wave. In summary, When the film experience compressive strain, the easy axis is in-plane; when the film experience tensile strain, the magnetic field is out-of-plane. We also observe clear spin wave signals in GaMnAsP film. When the spins are confined due to the finite thickness of the sample, we observe clear spin wave signal when the magnetic field is out-of-plane; when the spins are confined due to the finite size of the pattern created on the surface, we observe typical spin wave signal when magnetic field is in-plane.

Acknowledgement

I would like to thank my advisor, Prof. Jacek Furdyna and Prof. Liu for guiding me through out the entire research process. I would also like to thank Prof. Garg for giving me this valuable opportunity.

Reference

- [1] Xinyu Liu and Jacek K Furdyna, Ferromagnetic resonance in $\text{Ga}_{1-x}\text{Mn}_x\text{As}$ dilute magnetic semiconductors, J. Phys.: Condens. Matter 18 (2006) R245-R279.
- [2] J.K. Furdyna, Diluted magnetic semiconductors, J. Appl. Phys. 64 (4), 15 August 1988.
- [3] Henryk Puzskarski, Theory of spin states in spin wave resonance, Progress in Surface Science, 1979, vol.9, pp. 191-247.
- [4] Charles Kittel, Introduction to solid state physics, 8th edition.